Title

Application of MR Spectroscopic Techniques for the Development and Translation of Metabolite Markers Characterizing Infiltrating Glioma

Permalink

https://escholarship.org/uc/item/28p7k6kk

Author

Elkhaled, Adam

Publication Date

2016

Peer reviewed|Thesis/dissertation

Application of MR Spectroscopic Techniques for the Development and
Translation of Metabolite Markers Characterizing Infiltrating Glioma

by

Adam Elkhaled

DISSERTATION

Submitted in partial satisfaction of the requirements for the degree of

DOCTOR OF PHILOSOPHY

in

Bioengineering

in the

GRADUATE DIVISION

of the

UNIVERSITY OF CALIFORNIA, SAN FRANCISCO

AND

UNIVERSITY OF CALIFORNIA, BERKELEY

Dedicated to my beloved parents,

Wayne and Susan

Acknowledgements

As I reflect on my experience as a PhD student, I am compelled to acknowledge the many who have contributed to my training and personal success in life. There is a general awareness among those in academia of what constitutes collaboration, but few are privy to the environment surrounding brain tumor research at UCSF, which supports the highest levels of engagement across campus. For several years now, I have had the pleasure of working alongside many of the talented individuals leading research efforts and learning from their expertise as dedicated members of this cause. They taught me a great deal about the collective impact that can be achieved in even the most challenging situations when passion is kept alive. I hold in equal regard those who have influenced the more technical aspects of my training at Berkeley/UCSF and who renewed my appreciation for the inherent beauty of science. Because of you, I was treated to the absolute thrill of discovery. By recognizing some of these and other important figures, I hope that I can adequately express my sincere debt of gratitude for the help given.

Being of key importance to my success, my thesis advisor and mentor, **Sarah Nelson**, deserves first mention. Without her unwavering support to propel me through the program, I could not have accomplished the work that follows. As a brilliant yet selfless leader, she has modeled what it means to advance science while also investing in the next generation. I can speak to so many occasions where she has gone out of her way to promote my professional development, whether it was through an ouside opportunity or particular engagement recommended for networking. More than that, she championed every success which benefitted me personally. Her sage advice and guidance over the years have meant very much to me and I am humbled to have shared this

experience with such a pioneer.

For providing clinical perspective and grounding projects in patient-oriented goals, I am grateful to **Susan Chang**, who embodies the translational spirit together with Sarah. Beyond her tremendous standing in the neurooncology community, Susan possesses an uncommon dedication to patients that has helped inspire me in my own efforts.

As my academic advisor and boon NMR guru, **John Kurhanewicz** has imparted a wealth of knowledge for which I am very thankful. His guidance in coursework kept me well-rounded and encouraged the pursuit of my specific interests with regard to imaging. He also helped guide certain aspects of my research and provided me with a framework to conduct hyperpolarized C13 bioreactor studies with Ilwoo Park.

For technical advice related to MRS development and quantification, I owe much to **Yan Li**, whose tireless work also benefited my projects. Another core member of the lab, **Wei Bian**, was very helpful when I first started performing research.

Close collaborators **Sabrina Ronen**, **Joanna Phillips**, **Hikari Yoshihara**, **Janine Lupo** and **Annette Molinaro** all deserve recognition, given their specific and notable contributions.

Ilwoo Park has been a good friend and mentor throughout my stent in graduate school and I have greatly enjoyed working with him on both *in vivo* and *ex vivo* hyperpolarized C13 projects.

After a motorcycle accident on the eve of graduating, I am grateful to **Lisa Lattanza** for surgically re-aligning the bones in my wrist and palm, and allowing me to say that I single-handedly completed my dissertation.

Without question, the greatest influence on my success in life has been my family and I am so thankful they remain at my side. My mom, **Susan Autry**, has loved, supported, sacrificed for and believed in me from the very beginning and provides ongoing inspiration. Likewise, my dad, **Wayne Conwell**, has been a foundational pillar and an excellent example of what it means to live with purpose. My step-mom, **Diana Conwell**, has always been very kind and seeking to help however possible. My grandparents, **Don** and **Ruth Autry**, share in my every accomplishment for all their support and are the very best.

<center>***</center>

Application of MR Spectroscopic Techniques for the Development and

Translation of Metabolite Markers Characterizing Infiltrating Glioma

by

Adam Elkhaled

ABSTRACT

Despite ever more advanced characterization, the family of malignant central nervous system diseases known as infiltrating glioma remain pernicious and resistant to treatment. Because of their molecular and pathologic heterogeneity, they are among the most complex cancers in adults, with tremendous variability in patient outcomes being observed across oncologic subtypes. Over the course of therapy, magnetic resonance imaging (MRI) is critical to evaluating the level of response as the diagnostic standard for clinical management. Conventional MRI, having superior soft tissue contrast, provides a non-invasive means of detecting abnormalities that are embedded within neural anatomy. However, gauging the full extent of tumor is difficult owing to non-specific changes, which may either reflect benign processes in the aftermath of treatment or tumor infiltration.

Given the ambiguity associated with anatomical imaging, magnetic resonance spectroscopy (MRS) has emerged as a technique that can add diagnostic value to clinical practice by probing signature chemical species characterizing disease. The primary focus of this work was the development of translatable biomarkers for infiltrating glioma using analogous *ex vivo* methodology that has greater sensitivity and spectral resolution. By analyzing image-guided tissue

samples acquired from a large cohort of patients with pathologically distinct subtypes, it was possible to characterize metabolite expression across diverse swathes of tumor representing natural heterogeneity. Quantified data revealed distinct metabolomic profiles for each of the clinically relevant subtypes that enabled their differential classification. Importantly, classification models were able to predict malignant progression on the basis of these profiles, highlighting the potential to determine pathologic trajectory. Separate analysis of contrast-based radiographic subtypes of the most aggressive form of glioma demonstrated unique metabolite expression in the portion of tumor that fails to exhibit contrast and is therefore masked on standard imaging.

Since some of the metabolite markers discovered exhibited features that diminished the lifetime of their signal, technical development of an *in vivo* MRS sequence was also undertaken. The creation of radiofrequency (RF) pulses with reduced peak power requirements was critical to the design of the sequence and enabled improved signal fidelity over longer acquisition times when incorporated into existing frameworks. Results from this project and those obtained *ex vivo* support greater clinical integration of spectroscopy.

Table of Contents

List of Figures

List of Tables

Chapter 1: Introduction

Through advanced pathologic and molecular characterization, infiltrating glioma have come to represent a heterogeneous class of malignant disease affecting the adult central nervous system. The most aggressive and common form of this disease is glioblastoma (GBM), which carries a median overall survival of less than 2 years despite treatment, making it especially hazardous to patients. Because GBM demonstrates a significant and dynamically evolving mutational burden, there are few conventional options for therapy that have proven effective long-term against acquired resistance, and these options can themselves exacerbate mutagenic activity in unpredictable ways. While the consequent molecular heterogeneity of GBM reflects the complex nature of this disease, it also exposes potential pathways that may be exploited by means of tailored treatment in the era of personalized medicine. Already immune-mediated and other advanced agents targeting aberrant enzymes have been emerging as potential candidates for targeting specific tumor variants. Regardless of their efficacy, research into novel treatment strategies will undoubtedly continue on multiple fronts, given the heterogeneous makeup of the disease.

Since its development, diagnostic imaging has factored prominently in the clinical management of patients with glioma, in terms of planning surgery and evaluating longitudinal response to therapy. As a safe and non-invasive technique, magnetic resonance imaging (MRI) naturally lends itself to such applications while also satisfying certain technical concerns, such as soft tissue contrast, that are relevant for the brain. Routine MRI examinations are standard under the current clinical care for patients and focus primarily on identifying anatomical abnormalities associated with tumor

infiltration. Although significant radiographic hallmarks of disease can be obtained through anatomical imaging, both malignant and treatment-related changes in the tissue can give rise to ambiguous findings that defy interpretation and even forestall clinical decision-making. In an effort to mitigate this shortcoming, several MR-based physiologic techniques were developed as supplemental diagnostics to evaluate most notably the perfusion, diffusion, and chemical content of GBM. These diagnostics remain powerful means of characterizing diverse processes that are involved in malignancy.

With regard to ascertaining the chemical content of GBM, magnetic resonance spectroscopy (MRS) offers a wealth of information that is valuable in patient imaging. By identifying signature resonances from nuclear species and their interaction, the technique can provide a quantifiable readout of metabolite expression that can help distinguish tumor against a background of healthy or treated tissue. More recent MRS methodologies allow for the dynamic assessment of metabolism *in vivo* using isotopically-labeled molecular probes that undergo enzymatic conversion. The *ex vivo* analogue and historic precursor to MRS known as nuclear magnetic resonance (NMR) has been used extensively in the field of metabolomics to profile disease due to its superior sensitivity and spectral resolution. While NMR can only be applied to small tissue specimens, these technical advantages make it a powerful tool in biomarker investigations designed to elucidate biology and ultimately improve the utility of MRS.

The goal of this thesis is to communicate the knowledge that has been gained in connection with profiling glioma metabolism via NMR and how it may be translated into clinically relevant MRS techniques. While infiltrating glioma are considered collectively in this work, emphasis has been

placed on GBM, which can arise from other such pathologies by way of malignant progression. Primary contributions include: i) differential classification of glioma pathological subtypes and their associated inter-conversions on the basis of *ex vivo* metabolite expression; ii) characterization of *ex vivo* metabolite expression in radiographic subtypes of GBM; and iii) technical development of an *in vivo* MRS sequence utilizing broadband RF pulses with quadratic phase. The following provides a summary of the topics presented and their general organization.

Chapter 2 serves as an introductory overview of infiltrating glioma in which GBM is prominently featured. After describing stem and progenitor cells that give rise to neuroglia and may be involved in gliomagenesis, the discussion turns to current molecular and histopathologic classifications of glioma. This chapter concludes with the clinical management of patients through treatment and serial MR surveillance.

Chapter 3 reviews fundamental principles of NMR and details technical development on an *in vivo* MRS pulse sequence. Historical backround for NMR is provided at the outset to contextualize the presentation of theory and also to help explain how aspects of quantum mechanics deviate from classical intuition. Latter sections cover high-resolution *ex vivo* spectroscopy techniques for dealing with tissue specimens and MRS pulse sequence development.

Chapter 4 presents original research on the *ex vivo* spectroscopic analysis of image-guided tissue samples acquired from patients with pathologically distinct subtypes of infiltrating glioma. This work was concerned with characterizing such subtypes and their inter-conversions according to broad metabolomic profiles, including onco-metabolite D-2-hydroxyglutarate. Machine learning

models were employed to assess the potential for differential classification.

Chapter 5 presents another *ex vivo* spectroscopy study that sought to characterize contrast-based radiographic subtypes of GBM. By comparing metabolite expression in contrast-enhancing versus non-enhancing GBM samples, the goal was to determine whether there were any markers of non-enhancing disease that is difficult to detect via standard anatomic MR imaging. Analysis was also performed on associated pathologic and *in vivo* physiologic MR data.

Chapter 2: GBM & Infiltrative Glioma

This chapter surveys the pathological, clinical, and diagnostic considerations that surround the modern study of brain tumors that are collectively known as infiltrating gliomas, with particular emphasis placed on the most malignant subtype: glioblastoma multiforme (GBM). Although the mechanistic basis for gliomagenesis remains elusive, considerable effort has been made in the opening section to explore the lineage of glial cells and their differentiation from neural progenitors. The focus then shifts toward the standard classification of gliomas by histopathological and novel molecular criteria that hold clinical significance with regard to relative malignancy and prognosis. Latter portions of the chapter are dedicated to the clinical management of patients with GBM, which includes treatment as well as non-invasive radiographic surveillance for disease progression.

2.1 Neuroglia & Neural Progenitors

At the earliest stages of human development, neural stem cells (NSCs) can be observed to have prominent roles in the functional specialization of the nervous system, based on their capacity for self-renewal and multipotency (1). They derive from the ectodermal germ layer and are intimately involved with how rudimentary neural structures mature into the complex anatomy of the brain and spinal chord (2). In these nascent structures, NSCs take the form of neuroepithelial cells (NEPs) that comprise what is known as the neuroepithelium: a highly organized cellular lattice, which facilitates the course of development (3). As neurogenesis progresses, NEPs undergo a series of cell divisions that either lead to their proliferation or differentiation, depending on both intrinsic properties and external cues from the neuroepithelial environment (4). The following

describes the lineage of differentiated cell types whose generational succession results in increased functional specialization, paralleling the loss of stem-like properties or "stemness".

Given their capacity for self-renewal, NEPs may proliferate by means of symmetric division to produce equivalent daughter cells that retain the parental stemness. Some of the NEP divisions, however, are asymmetric and give rise to different cell types with novel functions pertaining to development. In this way, a single asymmetric division might generate both a neuron and radial glial cell; an alternative scenario is found in the subventricular zone (SVZ), where basal progenitors are cellular intermediates for neurons, being directly produced by NEPs (3). As the presence of neurons and basal progenitors is not thought to be relevant in the formation of glioma, the focus in the following discussion will be on the fate of radial glia. These cells have long processes that radiate outward from the ventricular zone toward the cerebral cortex during neurogenesis, providing guidance to migrating neurons via their intricate scaffolding (5). Upon induction, they acquire astroglial hallmarks, including most notably glial fibrillary acidic protein (GFAP), along with metabolite transporters and enzymes related to glutamatergic activity (5). Despite having restricted pathways for differentiation, radial glial cells still collectively exhibit aspects of the canonical properties associated with embryonic NSCs.

Through various investigative studies, it has been determined that heterogeneity amongst radial glial populations is responsible for their diverse progeny (6). Whereas early in neurogenesis these cells are understood to produce vast numbers of neurons within the central nervous system, their importance here follows from the later production of astrocytes and oligodendrocytes, among other cell types (3, 5). Astrocytes and oligodendrocytes constitute only a few of the known neuroglia

that play integral roles in the central nervous system (CNS), but they are unique in that their histology bears a strong resemblance to infiltrative neoplasms that form the subject of this chapter.

Astrocytes, or astroglia, perform diverse and manifold functions within the CNS that are critical to development and the maintenance of homeostasis. Like radial glia, they can be described as having heterogeneous populations, though this heterogeneity is primarily constrained to anatomical location and morphology. Grey matter, for example, characteristically exhibits protoplasmic astrocytes with short branched processes, while white matter contains fibrous astrocytes that project long unbranched processes (7). During development, these astrocytes are involved in guiding the migration of neuronal axons and immature neurons, or neuroblasts, along pre-determined paths (8). This assistance lent to neurons also extends to the formation of emerging synapses, in which molecular signaling by astrocytes has been explicitly implicated (9). Furthermore, being in close proximity to synaptic junctions through their cellular processes, astrocytes demonstrate several regulatory functions for maintaining homeostasis, including the control of surrounding fluid, pH, and neurotransmitters (7). Another important role in the adult CNS is the regulation of blood flow via endogenous production and excretion of vasodialators and vasoconstrictors (10). In a related role, they also interface with endothelial cells whose tight junctions form the blood brain barrier (BBB) governing molecular diffusion across vasculature.

In response to injury, astrocytes undergo a process known as reactive gliosis. While there exists a variety of pathological manifestations associated with gliosis that depends on its severity, the most common features are upregulation of GFAP expression and cellular hypertrophy (11). Extreme cases of gliosis can, however, induce astroglial proliferation and scar formation, the latter of which

is thought to protect against further damage from infection and auto-immmune responses (12). As part of a parallel process, oligodendroglial progenitor cells (OPCs) have been found to amass at the same sites of neurologic insults, ostensibly participating in the restorative efforts of the nervous system, with clear implications for neuronal support (13). These OPCs serve as cellular intermediates between radial glial cells and oligodendrocytes, and uniquely express *neural/glial antigen 2* (*NG2*) and *platlet-derived growth factor receptor alpha* (*PDGFRα*)(14). Because OPCs persist on into adulthood through "quiescent pools" residing within the SVZ, they can be recruited for special tasks like remyelination (15).

Over the embryonic stages of development, OPCs that derive from a variety of anatomical sources produce oligodendrocytes, following their migration to different regions of the brain (15). The oligodendrocytes, or oligodendroglia, perform the important function of myelinating neuronal axons in order to facilitate transmission of evoked action potentials. Myelin consists of a mixture of proteins and phospholipids that provides an insulating sheath around multiple axons and reduces resistance to electrical signaling. Owing to the rate at which myelin is produced during neurogenesis, oligodendrocytes demonstrate ultra high metabolism (16).

2.2 Diffuse Infiltrating Gliomas

Diagnosis and Pathology

Gliomas constitute a heterogeneous class of CNS tumors that arise as a result of genotypic alterations to cells that share glial lineage. Owing to the profound complexity characterizing this family of disease, there has been an ever-evolving set of clinically relevant features pertaining to diagnosis, which are elaborated here in detail. In an effort to extract standard measures of glioma

malignancy, surgically excised tissue is routinely graded on a four-tier scale according to histopathologic criteria developed by the World Health Organization (WHO)(17). Grade I gliomas are considered benign and can typically be eradicated through surgical intervention, while infiltrating gliomas of grades II-IV represent terminal disease that is marked by diffuse invasion into surrounding tissue. Criteria for assigning malignancy to infiltrating gliomas are defined such that successive grades manifest progressively worse pathological features. Nuclear atypia, a feature common to all gliomas and observed under the microscope via hematoxylin and eosin staining (H&E), forms the basis for diagnosing grade II glioma. Grade III (anaplastic) gliomas additionally possess elevated mitotic activity, as measured by the KI-67 antibody, and thus exhibit more aggressive behavior with regard to proliferative potential. At the apex of this system of classification is the grade IV glioblastoma (GBM) whose hallmarks of necrosis and microvascular proliferation — identified through H&E and Factor VIII staining, respectively — stand alongside the most advanced mitotic activity.

The advent of novel molecular markers within the field of cancer research has caused a considerable shift in the WHO classification paradigm for gliomas as it relates to the diagnosis of histological subtypes. Whereas gliomas were previously named after the differentiated glial cells they resembled morphologically on histology, i.e., astrocytomas, oligodendrogliomas, or mixed oligoastrocytomas, the current WHO consensus criteria of 2016 also stipulate that any categorization include molecular parameters that can further inform prognosis (17). These new guidelines have allowed for more definitive classification based upon the unique biology encoded by molecular data. A notable consequence is that oligoastrocytomas were eliminated as diagnostic entities, given the ability to consistently define oligodendroglial versus astrocytic lesions using

immunohistochemical (IHC) surrogates for genetic alterations; very rarely do gliomas express genotypic evidence of both subtypes. Although not without challenges, the changes adopted in the recent criteria signal greater integration of genetic markers as they become available for clinical use.

Because many of the details behind the latest CNS WHO guidelines are beyond the scope of this thesis, the following addresses only aspects which bear relevance to the research or that offer greater insight into the mechanisms of oncogenesis. The discovery of isocitrate dehydrogenase (*IDH*) mutations, made possible through genome-wide sequencing of glioma, engendered a sort of gestalt switch in cancer research, as it revealed for the first time an early oncogenic event conserved across a broad spectrum of disease, including colorectal cancer, prostate cancer, and acute myeloid leukemia (18, 19). In the case of gliomas, clinicians have importantly identified a significant survival benefit for patients that harbor *IDH* alterations, which underlies the current rationale to assess mutational status, either via sequencing or more commonly by IHC analysis employing the IDH[R132H] (enzyme) antibody (20). While the implications of this mutation for the TCA cycle and with regard to diagnostic imaging merit further discussion (see Section 2.3), its prognostic and determinant biological value is of primary concern here. Occurring in as much as 70-80 percent of grade II and III glioma and 5 percent of GBM (18, 21), *IDH* mutations constitute the most prominent molecular feature within WHO criteria, and determine what further characterization is warranted as part of diagnosis.

On the condition that *IDH* mutational status can be established, there are subsequent molecular evaluations with which to render a determination of histological subtype in grade II and III glioma.

Loss of chromosome t(1p;19q) resulting from an unbalanced whole-arm translocation between chromosomes 19 and 1 is a signature feature of oligodendroglial tumors that is also predictive of favorable response to treatment (22-24). By contrast, completely unaltered 1p/19q or partial distal deletions of chromosome 1p, with 19q remaining intact, signify astrocytic lineage and carry a poor prognosis (25). Using fluorescence *in situ* hybridization (FISH) or more specific techniques such as comparative genomic hybridization array (aCGH), one can assay 1p/19q integrity as a means to discriminate these histological subtypes (26). Empirical evidence gathered to date suggest that the 1p/19q codeletion of oligodendroglial tumors is almost always accompanied by *IDH* mutation, but mutually exclusive with the tumor suppressor gene *TP53* mutation and epidermal growth factor receptor (EGFR) amplification, which characterize astrocytic counterparts (26, 27). Astrocytic tumors are also known to express alterations of *transcriptional regulator alpha thalassemia/mental retardation syndrome X-linked* (*ATRX*), recently implicated in both the promotion of tumor growth and impairment of nonhomologous end joining (NHEJ) DNA repair (28).

In considering the diagnosis of *IDH* wild-type for either histological subtype, one must eliminate the possibility of both *IDH1* and *IDH2* mutations. Because current methods generally only assay the most common mutation in *IDH1* (*IDH1*[R132H]) via antibody staining, this diagnosis can be somewhat dubious.

Although GBMs overwhelmingly exhibit astrocytic lineage, making the assessment of histologic subtype applicable in only very rare instances, the *IDH* mutational status remains important for purposes of classification. The WHO has made an effort to accommodate results from clinical

studies evaluating survival among patients with high-grade glioma by establishing *IDH* wild-type and *IDH*-mutant GBM as distinct diagnostic entities. In contradistinction with lower grade glioma, GBMs are dominated by the non-mutant genotype, and therefore display a comparatively worse probability of having tempered prognoses.

Summarized below are the official 2016 WHO diagnoses for infiltrating glioma, based on the incorporation of novel molecular criteria. Wherever molecular findings conflict with those of histology regarding subtype, deference is given to the former.

WHO grade II / III diagnoses

Diffuse astrocytoma, *IDH* mutant — *IDH* mutant, 1p/19q intact or partially deleted; characteristic *ATRX* and *TP53* mutations unnecessary for diagnosis

Diffuse astrocytoma, *IDH* wild-type — *IDH* wild-type; diagnosis of exclusion should rule out both *IDH1* and *IDH2* mutations, along with ganglioglioma

Oligodendroglioma, *IDH* mutant — *IDH* mutant, 1p/19q codeleted, *ATRX* wild-type

Oligodendroglioma, *NOS* (not otherwise specified) — *IDH* wild-type; diagnosis of exclusion should rule out both *IDH1* and *IDH2* mutations

WHO grade IV (GBM) diagnoses

Glioblastoma, *IDH* wild-type — *IDH* wild-type; overwhelmingly the diagnosis of primary GBM that arise de novo, lacking prior neoplastic history (infra supra)

Glioblastoma, *IDH* mutant — *IDH* mutant; commonly associated with secondary GBM that arise from malignant progression in lower grade glioma (infra supra)

Malignant Progression

The description of glioma pathology presented thus far has addressed several classifications of malignancy without explaining the inter-relationship that exists between them. This section discusses fundamental concepts in the evolution of infiltrative disease, and, in the process, introduces important nomenclature for characterizing particular aspects of diagnosis not yet considered. Once induced through mutagenesis, gliomas can undergo a further process of transformation that, according to recent data from The Cancer Genome Atlas (TCGA), likely entails progressive genetic alteration, which evolves along specific pathways (29). From a pathological standpoint, grade II and III gliomas are each capable of converting to higher grades of malignancy over the course of disease, indicating a dynamic process. Because these inter-grade transitions range in outcome at the time of clinically-defined disease progression, there is an impression given of pathologic trajectory, i.e, whether a grade II is directed to remain the same with regard to malignancy or convert to grade III or even GBM. The multiple routes followed by malignancy necessitate the distinction between what is termed as the primary, or *de novo*, grade assessed at initial diagnosis and the secondary grade that may be subsequently determined. Such terminology is applied to both grade III glioma and GBM, however the latter is more commonly

referenced by these descriptors in the literature owing to its increased incidence.

In the era of personalized medicine, where stratifying genetic strains and identifying clonality is becoming ever more imperative, the question of GBM origin holds clinical significance. Indeed, the knowledge of whether GBMs derive from primary versus secondary lineages can offer prognostic value for patient outcome irrespective of treatment, as well as predictive value for response to therapy when considering *IDH* mutation. Besides being the most frequently encountered gliomas in the clinic, primary GBMs display generally worse survival statistics relative to secondary counterparts. They may also face misdiagnosis in a small handful of cases, given the potential for secondary disease to remain clinically silent before attaining high-grade features.

Molecular Subtypes of GBM

The molecular heterogeneity of infiltrating glioma culminates in the complex genetic makeup of GBM. As a result of far-reaching collaboration, a landmark study was published in 2010 that made great strides toward deconstructing this complexity (30). By analyzing gene expression profiles from a large cohort of patients, the study managed to isolate four clinically-relevant subtypes of GBM: classical, mesenchymal, proneural, and neural. Each subtype represents a broad swathe of signature gene expression that consistently clusters together, and thereby enables reliable classification, which has practical significance. Associated patterns of somatic mutations and DNA copy number alterations were found to further characterize these subtypes by abnormalities in *platlet-derived growth factor subunit A (PDGFA), IDH1, epidermal growth factor receptor (EGFR), and neurofibromin 1 (NF1)*. In partial answer to questions of origin and etiology,

correlative analyses also demonstrated strong relationships between the classified GBM variants and specific cell lineages.

Perhaps the greatest contribution of this work (30), however, was extending the novel molecular interpretation of GBM subtypes to an understanding of clinical implications. The partitioning of aggregate patient data using newly-defined classifications provided a means by which survival analysis could be performed between therapeutic arms of different intensity. Under this study design framework, it was determined that certain molecular subtypes of GBM benefit from more aggressive therapy, while others show only limited response. Such results underscore the impact of being able to relate integrated multidimensional genomic data to patient outcome and present a model basis for continuing research. A brief synopsis of information from the study characterizing individual GBM subtypes is related in the following:

Classical — *Astrocytic lineage*, *EGFR amplification*. Subtype demonstrates the greatest response to aggressive versus less intense treatment and a propensity for EGFR amplification that is unique among GBM. *EGFRvIII* mutations are also more likely than in other GBM variants. Although occurring frequently in other molecular subtypes, the combination of Chromosome 7 amplification and Chromosome 10 loss is always present here. These features are contrasted by the lack of *TP53* mutations otherwise common to GBM. Affected signaling pathways commonly include Notch and Sonic hedgehog.

Mesenchymal — *Cultured astroglia lineage, NF1 deletion*. Subtype demonstrates heightened response to aggressive versus less intense treatment and frequent focal hemizygous deletions of a

region containing *NF1,* lowering its expression. Considering the heightened activity of mesenchymal and astroglial markers associated with epithelial-to-mesenchymal transition (EMT), such GBM may be particularly malignant. Most of the *NF1* and *phosphatase and tensin homolog* (*PTEN*) co-mutations affecting the AKT pathway are observed here. The *retinoblastoma-associated protein* (*RB1*) mutation, generally of low to zero frequency in other subtypes, occurs more often in this GBM variant. Its elevated expression of tumor necrosis factor (TNF) super family pathway (ref) and NF-κB pathway is linked to necrosis.

Proneural — *Oligodendroglial lineage, IDH1 and PDGFRA alterations*. Subtype demonstrates longer survival, strong response to treatment, and relatively frequent alterations to *IDH1* and *PDGFRA* that rarely coincide with one another. Contrary to the combined Chromosome 7 amplification and Chromosome 10 loss charactering classical GBM, this variant demonstrates few such events. The highest frequency of *TP53* mutation and loss of heterozygosity (LOH) likewise depart from that of classical GBM. Mutations are also more common in *phosphatidylinositol-4,5-bisphosphate 3-kinase catalytic subunit alpha* (*PIK3CA*)/*phosphoinositide-3-kinase regulatory subunit 1* (*PIK3R1*). Because this subtype expresses oligodendroglial development genes, including *oligodendrocyte transcription factor* (*OLIG2)*, it is particularly unique among GBMs possessing astrocytic lineage. This variant derives its namesake from the proneural development genes it bears such as *sex determining region Y-box 2* (SOX2).

Neural — *Neuronal lineage, neuron markers*. Subtype demonstrates heightened response to aggressive versus less intense treatment on par with mesenchymal subtypes and neuron markers, including *NEFL,* that have been implicated in neuron projection and axon transmission. This

variant is most closely related to normal cells, a fact which belies its pernicious nature.

2.3 Clinical Management of GBM

Epidemiology and Demography

Among infiltrating glioma and the much larger domain of CNS tumors, GBM represents the most common form of malignant disease. According to the California Cancer Registry (CCR), the annual age-adjusted incidence of GBM was 3.6 per 100,000 persons, during the evaluated period of 2001-2005 (31). While GBM incidence has risen steadily since earlier decades, this trend appears to reflect institutional improvements in the quality of reporting (32), which have been encouraged by funding agencies and other interest groups involved in the culling of data. Based on the analysis of aggregate demographic information from patients, disease rates within diverse subpopulations are now routinely being tracked, allowing knowledge of associated risk factors to grow as data accumulates. In its 2015 retrospective report, the Central Brain Tumor Registry of the United States (CBTRUS) mentions the increased incidence of disease with age: whereas elderly individuals 75-84 years old were shown to express the highest rates, young adults and children were much less susceptible (33). The same report cited males as having a 1.6 times greater likelihood of GBM diagnosis compared to females. With regard to ethnicity, non-Hispanic Whites are most prone to GBM, demonstrating a many-fold increase in incidence over Blacks and Asians/Pacific Islanders, when using age-standardized rates (34).

Survival and Prognostic/Predictive Factors

Because GBM carries a median overall survival (OS) of only 14 months, even with aggressive intervention, clinicians must carefully weigh treatment options for patients against quality of life

(35). Despite modern advances toward discriminating molecular features of this disease, there are no standardized means of addressing heterogeneity among patients in the style of personalized medicine. However, while the tailoring of treatment remains an ongoing struggle, neurooncologists have managed to validate a set of biological markers that can report on survival and the potential efficacy of standard-of-care therapy at the outset of patient management. Such prognostic and predictive factors are, by virtue of their clinical relevance, important for characterizing patient disease within the broader context of WHO classifications.

In addition to the heterogenous genetic features of GBM, it is now widely undertood that downstream epigenetic effects can influence disease response to therapy. Hypermethylation of the O^6-Methylguanine-DNA methyl transferase (MGMT) promotor in certain patients, for example, has strong predictive value for alkylating chemotherapy (36, 37). MGMT functions as a repair protein that is responsible for removing alkyl groups with mutagenic activity from the O^6-position of DNA constituent guanine. Under ordinary circumstances, the presence of a mutagen activates DNA repair mechanisms, which can remove the alkyl group directly via the MGMT promotor as a first-line defense against mutation. When this fails, O^6-alkylguanine adducts are subject to mismatch repair (MMR), base excision repair (BER), and DNA strand-break repair mechanisms that attempt to salvage even badly damaged molecules, and thus avert cell destruction if possible (38). Generally speaking, alkylating agents designed to target cancer cells undergoing high rates of mitoses will induce cell death (apoptosis) by methylating DNA and confounding its repair at the most complex levels. Hypermethylation of the MGMT promotor epigenetically silences its activity, thereby increasing the relative cytotoxicity of alkylating agents. As a result, the hypermethylated phenotype has predictive value in the treatment of patients with standard-of-care

chemotherapy, and is now routinely evaluated.

Although lacking establishment within the neurooncology community as a prognostic factor, epidermal growth factor receptor (EGFR) overexpression has been of some interest in evaluating patient survival. Being present in approximately 60% of patients, such overexpression has led several studies to investigate its clinical significance alongside the effects of the most common EGFR mutant: EGFRvIII (39). In at least one study, EGFR was found to be an unfavorable independent prognostic factor in OS (40), while others suggested EGFRvIII was an unfavorable prognostic factor only after 1 year of survival (41) and also with regard to OS (42). The last study referenced additionally demonstrated that EGFRvIII-mutant cell cultures were less sensitive to alkylating agent temozolomide. Because EGFR induces proliferation and is implicated in oncogenic signaling, attempts at using the status of EGFR overexpression and mutation for prognosis and targeted therapy will remain active.

As mentioned previously, mutations in *IDH1/2* are reported to account for a small fraction of primary GBM cases, though this may be owing to clinically silent low-grade disease that has progressed. Regardless of how these GBM arise, such mutations confer a significant survival advantage to patients, making them strong prognostic factors. Wild-type versions of these genes code for $NADP^+$-dependent oxidoreductases IDH1/2, which catalyze the conversion of isocitrate to alpha-ketogultarate (alpha-KG) in the TCA cycle. Missense mutations cause the arginine residue at the enzyme's binding site to be replaced by histidine (R132H) or other amino acids. This results in the aberrant production of onco-metabolite D-2-hydroxyglutarate (2HG) through an extraordinary gain-of-function, wherein alpha-KG becomes the substrate (43). Because 2HG has

little to no biological relevance for metabolism, it accumulates in large quantities intracellularly and is eventually exported to the extracellular space surrounding *IDH*-mutant tumor. The quantified levels of 2HG were determined to be on the same order as common neurochemicals glutamate and glutamine using *ex vivo* nuclear magnetic resonance (NMR) techniques (see Chapter 3), however *in vivo* detection remains complicated by overlapping resonances from γ-aminobutyric acid (GABA) and other chemical species (44). Despite the difficulty in resolving 2HG *in vivo*, the prospect of non-invasively obtaining information on prognosis prior to surgery and of monitoring therapeutic efficacy compels ongoing investigations, including those of Andronesi *et al.* and Choi *et al.* (45, 46).

Besides the molecular-based prognostic and predictive factors for GBM, there are also strong indicators of OS routinely observed within the clinic: younger age at diagnosis; greater extent of surgical resection; and higher Karnofsky performance status (KPS), which qualitatively measures the health condition of the patient (47).

Treatment

Although longstanding research concerning diverse aspects of GBM has greatly improved clinical characterization of the disease, significant advances in treatment have proven elusive. This is owing in part to the difficulty associated with developing agents that are efficacious against the many redundant pathways supporting tumor viability. Even when promising agents emerge from regulatory pipelines, clinical trials require considerable resources to thoroughly evaluate their efficacy, necessarily limiting institutional bandwidth by strategic prioritization. Because of the acute need for novel drug discovery, efforts are now underway to relax certain aspects of the

regulatory process and generally promote timely translation. The following summarizes the current standard-of-care treatment that has been established for patients with primary or secondary GBM, based on the clinical trial evidence presented thus far.

Surgical resection is the first line of treatment administered to patients after radiographic findings clearly indicate GBM. Beause the growth of the lesion will often impinge upon surrounding anatomy and increase intracranial pressure, surgery can potentially avert life-threatening complications in the near-term. Long term benefits, however, stem from the debulking of tumor cells that perpetuate invasive and proliferative processes. Thus, a gross total resection (GTR), which removes all radiographically-indicated regions of tumor, is most desirable, but cannot always be accomplished, given that some of the tumor may reside in critical anatomy, such as language centers or significant commisures.

Following surgery, clinicians adhere to the Stupp protocol originating in 2005 that combines radiotherapy and chemotherapy to synergistically enhance OS (48). This regime importantly stipulates 6 weeks of fractionated radiotherapy (Rx; 60 Gy total; 2 Gy per fraction) with concomitant alkylating agent temozolomide (TMZ; 75 mg/m^2 body surface area), administered each day and for 6 months after the end of radiation. Radiotherapy uses ionizing radiation to damage DNA in rapidly dividing cells and is critically mediated by reactive oxygen species (ROS) (49). Depending on the local dosage, patients can experience mild to acute acute radiation injuries that manifest anywhere from days to years after treatment. While the mechanism of action for TMZ was previously elaborated above, it should be noted that this chemotherapeutic induces mutations that alter the constitution of glioma, and may even drive the evolution of TMZ-resistance

in GBM (50). The efficacy of the Stupp protocol derives from the synergistic effects of radiation plus TMZ, whose combination is especially potent to GBM, while still being well tolerated by patients.

In addition to the standard-of-care chemotherapy, patients on clinical trials are often given adjuvant agents and therapies to determine whether they offer any further benefits. One of the most widely employed adjuvant agents is the mono-clonal antibody bevacizumab (Avastin), which acts as an anti-angiogenic for blocking vascular endothelial growth factor A (VEGF-A), and also reduces swelling (51). To treat residual disease surrounding the resection cavity, the National Comprehensive Cancer Network (NCCN) guidelines for newly diagnosed and recurrent GBM support the local implantation of Gliadel wafers containing carmustine, an alkylating chemotherapeutic (52). The NCCN also recommends the use of alternating tumor-treating fields (TTF), which have been shown to interfere with GBM mitosis and work synergistically with radiation treatment (53). Patients being treated with TTF (Optune, NovoCure Ltd, Jersey) actually wear an FDA-approved device on their scalp with transducer arrays that alternate electric fields at 100-300 kHz (53).

MR Surveillance

Lying at the center of routine patient management is the role of diagnostic imaging for monitoring the course of treatment. Prior to the initiation of therapy, patients receive a clinical MR exam to establish a baseline that can be compared against subsequent exams that are carried out every 2 months. The serial exams provide non-invasive snapshots of the response to therapy over pre-determined intervals, allowing clinicians to gauge the status of a patient and compare it to others

on the same regime. While modern MR imaging protocols are multi-parametric in nature, acquiring diverse physiologic measurements, the clinical gold standard remains anatomical imaging. Given that MRI offers unprecedented soft tissue contrast in the brain, there is tremendous potential to dileneate anatomical abnormalities with relative ease. Indeed, clinical disease management relies on the radiographic evidence of such abnormalities and their evolution over time.
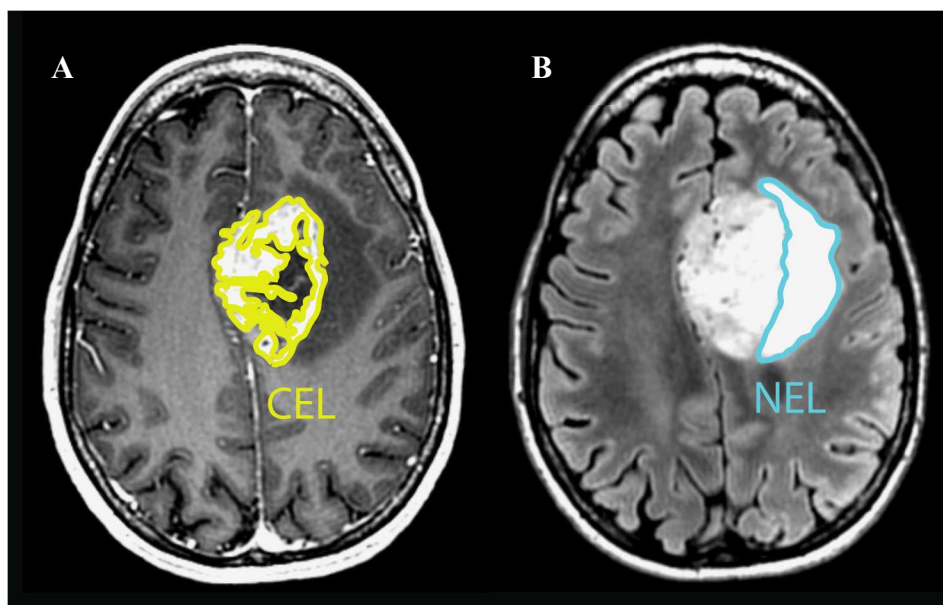
Figure 2.1. T_1- and T_2-weighted imaging. Axial MR images from a patient with GBM: T_1-weighted IRSPGR with the constrast-enhancing lesion (CEL) highlighted in yellow (A); and T_2-weighted FLAIR with the non-enhancing lesion (NEL) highlighted in blue and partitioned from the overall T_2 lesion (B)

As discussed in the subsequent chapter on elementary MR physics, there are a variety of mechanisms for generating image contrast from MRI. In clinical imaging, contrast is based on either T_1 or T_2 time constants, which reflect the rate of MR signal restoration and decay, respectively. These time constants are tissue- and field-dependent and their associated acquisition techniques are complementary in the sense that they provide unique though not completely

uncorrelated information. Figure 2.1A shows an example of an axial T_1-weighted image obtained from a patient with GBM. The T_1-weighted image can be readily identified by its white and gray matter contrast that serves to separate commisures, cortex, and deep gray structures with approximately 1 mm isotropic spatial resolution in 3-D. This particular image was acquired after the administration of gadolinium-based contrast that shortens the T_1 in the vasculature and surrounding regions where the BBB has been compromised by tumor infiltration, giving rise to hyperintense signal. The relatively bright T_1 signal from contrast extravasation is a radiographic hallmark of angiogenesis in GBM (but may also indicate radiation injury). Because of the specific contrast of this image, the edge of a centrally necrotic core is often plainly visible as a dark region in newly diagnosed patients, and the resection cavity from a patient that has undergone surgery takes on a similar appearance.

For T_2-weighted images, the abnormally hyperintense signal corresponds to the local influx of fluid that may have several non-specific causes: infiltrative tumor, edema, or the effects of treatment. In Figure 2.1B, the axial T_2-weighted image acquired from the same slice as the T_1 image illustrates the full extent of the abnormality presented by the disease and associated complications. Because tumor infiltration and edema often exceed the region of contrast extravasation, the T_2 lesion is usually much larger. Although the putative tumor lesion is radiographically defined as the union of the T_1 and T_2 lesions, only the T_1 hyperintensity is designated to contain mostly tumor. Thus, modern physiologic imaging techniques have been employed to discern which portions of the T_2 lesion also harbor GBM and require treatment.

Once a patient has initiated treatment, clinicians are tasked with monitoring serial changes on

imaging that would indicate response to therapy versus tumor progression. Owing to the dynamic nature of tissue undergoing treatment and subject to neoplastic invasion, the ongoing interpretation of imaging faces tremendous challenges, particularly with the ambiguity of non-specific changes that are commonly encountered. While the course of the T_1 lesion was historically evaluated for clinical decision-making, the advent of anti-angiogenics like Avastin, which normalize aberrant vasculature, have largely quelled the appearance of T_1 hyperintensity due to contrast extravasation, necessitating more advanced metrics. The current Response Assessment in Neuro-Oncology (RANO) criteria utilize a $\geq 25\%$ increase in the T_1 lesion or an increase in the T_2 lesion to determine disease progression; and also define various levels of non-progressive/responsive disease based on these imaging variables (54). Notwithstanding these novel criteria, terms such as *pseudo-response* and *pseudo-progression* remain ingrained in the clinician's lexicon and are symptomatic of modern challenges in radiology.

2.4 References

1. Rao MS, Mayor-Proschel M. Glial-restricted precursor are derived from multipotent neuroepithelial stem cells. Developmental Biology 188, 1997: 48-63

2. Whalley K. Development: the default position. Nature Reviews Neuroscience 12, 2011: 188-189

3. Gotz M, Huttner WB. The cell biology of neurogenesis. Nature Reviews Molecular Cell Biology 6, 2005: 777-788

4. Zolessi FR. Vertebrate Neurogenesis: Cell Polarity. Encyclopedia of Life Sciences. John Wiley

& Sons, Ltd., c2001.

5. Dimou L, Gotz M. Glial cells as progenitors and stem cells: new roles in the healthy and diseased brain. Physiol. Rev. 94, 2014: 709-737

6. Pinto L, Gotz M. Radial glial heterogeneity the source of diverse progeny in the CNS. Prog. Neurobiol. 83, 2007: 2-23

7. Sofroniew MV, Vinters HV. Astrocytes: biology and pathology. Acta. Neuropathol 119, 2010: 7-35

8. Powell EM, Geller HM. Dissection of astrocyte-mediated cues in neuronal guidance and process extention. Glia 26: 73-83

9. Christopherson KS, Ullian EM, Stokes CC, Mullowney CE, Hell JW, Agah A, Lawler J, Mosher DF, Bornstein P, Barres BA. Thrombospondins are astrocyte-secreted proteins that promote CNS synaptogenesis. Cell 2005, 120: 421-433

10. Gordon GR, Mulligan SJ, MacVicar BA. Astrocyte control of the cerebrovasculature. Glia 55, 2007: 1214-1221

11. Robel S, Berninger B, Gotz M. The stem cell potential of glia: lessons from reactive gliosis. Nature Review Neuroscience 12, 2011: 88-104.

12. Hermann JE, Imura T, Song B, Qi J, Ao Y, Nguyen TK, Korsak RA, Takeda K, Akira S, Sofroniew MW. STAT3 is a critical regulator of astrogliosis and scar formation after spinal chord injury. J Neurosci. 28, 2008:7231-7243

13. Duncan GJ, Assinck P, Hilton BJ. Canonical Wnt signaling in PDGFRa-expressing cells is a critical regulator of astrogliosis and axon regeneration following CNS injury. The Journal of Neuroscience 34(49), 2014: 16163-16165

14. Cregg JM, DePaul MA, Filous AR, Lang BT, Tran A, Silver J. Functional regeneration beyond the glial scar. Exp Neurol, 253, 2014: 197-207

15. Bradl M, Lassmann H. Oligodendrocytes: biology and pathology. Acta Neuropathol. 119, 2010: 37-53.

16. McTigue DM, Tripathi RB. The life, death, and replacement of oligodendrocytes in the adult CNS. J Neurochem 107, 2008: 1-19

17. Louis DN, Perry A, Reifenberger G, von Deimling A, Figarella-Branger D, Cavenee WK, Ohgaki H, Wiestler OD, Kleihues P, Ellison DW. The 2016 World Health Organization classification of tumors of the central nervous system: a summary. Acta Neuropathol 131(6), 2016: 803-820

18. Yan H, Parsons W, Jin G, *et al*. ID1 and IDH2 mutations in gliomas. NEJM 360, 2009: 765-773

19. Parsons DW, Jones S, Xhang X, et al. An integrated genomic analysis of human glioblastoma multiforme. Science 321, 2008: 1807-1812

20. Houillier C, Wang X, Kaloshi G, *et al*. IDH1 or IDH2 mutations predict longer survival and response to temozolomide in low-grade gliomas. Neurology 75, 2010: 1560-1566

21. Combs SE, Rieken S, Wick W, Abdollahi A, von Deimling A, Debus J, Hartmann C. Prognostic significance of IDH1 and MGMT in patients with glioblastoma: one step forward and one step back? Radiat Oncol. 6, 2011: 115

22. Bromberg JE, van den Bent MJ. Oligodendrogliomas: molecular biology and treatment. Oncologist 14(2), 2009:155–163.

23. Jenkins RB, Blair H, Ballman KV et al. A t(1;19)(q10;p10) mediates the combined deletions of 1p and 19q and predicts a better prognosis of patients with oligodendroglioma. Cancer Res. 66(20), 2006: 9852–9861.

24. Cairncross JG, Ueki K, Zlatescu MC et al. Specific genetic predictors of chemotherapeutic response and survival in patients with anaplastic oligodendrogliomas. J. Natl Cancer Inst. 90(19), 1998,1473–1479.

25. Idbaih A, Marie Y, Pierron G et al. Two types of chromosome 1p losses with opposite significance in gliomas. Ann. Neurol. 58(3), 2005: 483–487.

26. Ducray F; Idbaih A, Wang XW, Cheneau C, Labussiere M, Sanson M. Predictive and Prognostic Factors for Gliomas. Expert Rev Anticancer Ther. 2011;11(5):781-789.

27. Weller M, Stupp R, Hegi ME, van den Bent M, Tonn JC, Sanson M, Wick W and Reifenberger G. Personalized care in neuro-oncology coming of age: why we need MGMT and 1p/19q testing for malignant glioma patients in clinical practice. Neuro Oncol 14 (suppl 4), 2012: iv100-iv108.

28. Koschmann C, Calinescu AA, Nunez FJ, Mackay A, Fazal-Salom J, Thomas D, Mendez F,

Kamran N, Dzaman M, Mulpuri L, Krasinkiewicz J, Doherty R, Lemons R, Brosnan-Cashman JA, Li Y, Roh S, Zhao L, Appelman H, Ferguson D, Gorbunova V, Meeker A, Jones C, Lowenstein PR, Castro MG. ATRX loss promotes tumor growth and impairs nonhomologous end joining DNA repair in glioma. *Science Translational Medicine* 8(328), 2016: 328ra28

29. Beyond the World Health Organization grading of infiltrating gliomas: advances in the molecular genetics of glioma classification Vigneswaran K, Neill S, Hadjipanayis CG. Ann Transl Med 2015;3(7):95.

30. An integrated genomic analysis identifies clinically relevant subtypes of glioblastoma characterized by abnormalities in PDGFRA, IDH1, EGFR and NF1 Verhaak RGW, Hoadley KA, Purdom E, Wang V, Qi Y, Wilkerson MD, Miller CR, Ding L, Golub T, Mesirov JP, Alexe G, Lawrence M, O'Kelly M, Tamayo P, Weir BA, Gabrie S, Winckler W, Gupta S, Jakkula L, Feiler HS, J. Hodgson G, C. James D, Sarkaria JN, Brennan C, Kahn A, Spellman PT, Wilson RK, Speed TP, Gray JW,]Meyerson M, Getz G, Perou CM, Hayes DN, and The Cancer Genome Atlas Research Network . *Cancer Cell*. 2010; 17(1): 98.

31. Glioblastoma in adults age 20 years and older. California Cancer Registry (2005). https://www.cdph.ca.gov/programs/ccr/Documents/GlioblastomaAdult-08.pdf

32. Hess KR, Broglio KR, Bondy ML. Adult glioma indcidence trends in the United States, 1977-2000. Cancer 101(10), 2004: 2293-2299

33. Ostrom QT, Gittleman H, Fulop J, Liu M, Blanda R, Kromer C, Wolinsky Y, Kruchko C, Barnholtz-Sloan JS. CBTRUS statistical report: primary brain and central nervous system tumors diagnosed in the United States in 2008-2012. Neuro-Oncology 17, 2015: iv1-iv62

34. Dubrow R, Darefsky AS. Demographic variation in incidence of adult glioma by subtype, United States, 1992-2007. BMC Cancer 11, 2011: 325

35. Johnson DR, O'Neill BP. Glioblastoma survival in the United States before and during the temozolomide era. J Neurooncol. 107, 2012: 359-364

36. Hegi ME, Diserens AC, Corlia T. MGMT gene silencing and benefit from temozolomide in glioblastoma. N Engl J Med. 352(10), 2005: 997-1003

37. Rivera AL, Pelloski CE, Gilbert MR, Colman H, De La Cruz C, Sulman EP, Bekele BN, Aldape KD. MGMT promotor methylation is predictive of response to radiotherapy and prognostic in the absence of adjuvant alkylating chemotherapy for glioblastoma. Neuro-Oncology 12(2), 2010: 116-121

38. Yoshimoto K, Mizoguchi M, Hata N, Murata H, Hatae R, Amano T, Nakamizo A, Sasaki T. Complex DNA repair pathways are possible therapeutic targets to overcome temozolomide resistance in glioblastoma. Front. Oncol. 2, 2012: 186

39. Delgado-Lopez PD, Corrales-Garcia EM. Survival in glioblastoma: a review on the impact of treatment modalities. Clin transl Oncol 18, 2016: 1062-1071

40. Shinojima N, Tada K, Shiraishi S, Kamiryo T, Kochi M, Nakamura H, Makino K, Saya H, Hirano H, Kuratsu J, Oka K, Ishimaru Y, Ushio Y. Prognostic value of epidermal growth factor receptor in patients with glioblastoma multiforme. Cancer Res. 63(20), 2003: 6962-70

41. Heimberger AB, Hlatky R, Suki D, Yang D, Weinburg J, Gilbert M, et al. Prognostic effect of epidermal growth factor receptor and EGFRvIII in glioblastoma multiforme patients. Clin Cancer Res. 63(20), 2003: 6962-6970

42. Montano N, Cenci T, Martini M, D'Alessandris QG, Pelacchi F, Ricci-Vitiani L, Maira G, De Maria R, Larocca LM, Pallini R. Expression of EGFRvIII in glioblastoma: prognostic significance revisited. Neoplasia 13(12), 2011: 1113-1121

43. L. Dang, D. W. White, S. Gross, B. D. Bennett, M. A. Bittinger, E. M. Driggers, V. R. Fantin, H. G. Jang, S. Jin, M. C. Keenen, K. M. Marks, R. M. Prins, P. S. Ward, K. E. Yen, L. M. Liau, J. D. Rabinowitz, L. C. Cantley, C. B. Thompson, M. G. Vander Heiden, S. M. Su, Cancer- associated IDH1 mutations produce 2-hydroxyglutarate. Nature 462, 2009: 739–744

44. Elkhaled A, Jalbert LE, Phillips J, Yosihara HAI, Parvataneni R, Srinivasan R, Bourne G, Berger MS, Chang SM, Cha S, Nelson SJ. Sci. Transl. Med. 4(116), 2012: 116ra5

45. Andronesi OC, Kim GS, Gerstner E, Batchelor T, Tzika AA, Fantin VR, Heiden MGV, Sorenson AG. Detection of 2-hydroxyglutarate in IDH-mutated glioma patients by in vivo spectral-editing and 2-D correlation magnetic resonance spectroscopy. Sci. Transl. Med. 4(116): 116ra4

46. Choi C, Raisanen JM, Ganji SK, Zhang S, McNeil S, An Z, Madan A, Hatanpaa KJ, Vemireddy V, Sheppard CA, Oliver D, Hulsey KM, Tiwari V, Mashimo T, Battiste J, Barnett S, Madden CJ, Patel TR, Pan E, Malloy CR, Mickey BE, Bacho RM, Maher EA. Prospective longitudinal analysis of 2-hydroxyglutarate magnetic resonance spectroscopy identifies broad clinical utility for the management of patients with IDH-mutant glioma. J Clin Onc 34(33), 2016: 4030-4040

47. Lamborn K, Chang SM, Prados MD. Prognostic factors for survival of patients with glioblastoma: recursive partitioning analysis. Neuro-Oncology 6(3), 2004: 227-235

48. Stupp R, Mason WP, van den Bent MJ, et al. Radiotherapy plus concomitant and adjuvant temozolomide for glioblastoma. N Engl J Med. 352, 2005: 987-996

49. Liou GY, Storz P. Reactive oxygen species in cancer. Free Radic Res. 44(5), 2010: 1-31

50. Johnson B, Mazor T, Hong C, et al. Mutational analysis reveals the origin and therapy-driven evolution of recurrent glioma. Science 343(6167), 2014: 189-193

51. Gilbert M, Dignam JJ, Armstrong TS, *et al*. A randomized trial of bevacizumab for newly diagnosed glioblastoma. N Engl J Med. 370, 2014: 699-708

52. Westphal M, Hilt DC, Bortey E, Delavault P, Olivares R, Warnke PC, Whittle IR, Jaaskelainen J, Ram Z. A phase 3 trial of local chemotherapy with biodegradable carmustine (BCNU) wafers (Gliadel wafers) in patients with primary malignant glioma. Neuro-Oncology 5(2), 2003:79-88

53. Kim EH, Kim YJ, Song HS, Jeong YK, Lee JY, Sung J, Yoo SH, Yoon M. Biological effect of an alternating electric field on cell proliferation and synergistic antimitotic effect in combination with ionizing radiation. Oncotarget 7(38), 2016: 62267-62279

54. Wen PY, MacDonald DR, Reardon DA, Cloughesy TF, Sorenson G, Galanis E, DeGroot J, Wick W, Gilbert MR, Lassman AB, Tsien C, Mikkelsen T, Wong ET, Chamberlain MC, Stupp R, Lamborn KR, Vogelbaum MA, van den Bent MJ, Chang SM. Updated response assessment criteria for high-grade gliomas: response assessment in neuro-oncology working group. Journal of

Clinical Oncology 28(10), 2010: 1963-1972

Chapter 3: Nuclear Magnetic Resonance

This chapter provides a brief overview of the principles governing nuclear magnetic resonance and their application to the study of infiltrating glioma via spectroscopic techniques. Presented at the outset is a discussion on the underlying property of spin that intimately characterizes the magnetic behavior of fundamental particles and the nuclei they compose. After providing details relating to the phenomenological basis for nuclear magnetic resonance and its measurement, the attention turns toward specialized *ex vivo* techniques enabling metabolomics-driven biomarker analysis of image-guided tumor samples. The final sections cover the analogous *in vivo* techniques that are applied to patients with the intention of monitoring specific biomarkers determined to be of interest in the evolution of disease or the effects of treatment.

3.1 Preliminary Context

The phenomenon known as nuclear magnetic resonance, or NMR, was first discovered in 1944 by the notable physicist Isidor Rabi, who subsequently received the Nobel Prize for his contribution to science. As with most revolutionary discoveries, this one yielded important insight, which paved the way for future exploration on the promise of a new paradigm. In the wake of Dr. Rabi, contemporary experimentalists Felix Bloch and Edward Purcell soon developed their own approaches independently to characterizing NMR that earned them Nobel status for the ensuing conceptual framework (1, 2). Although these early pioneers helped engender the modern field of research, viewing their work in isolation would be a gross oversight of historical contributions

made by a long line of prominent and lesser known physicists whose experiments were ground-breaking in and of themselves. The cumulative dispensation of these efforts has produced a body of work that is steeped in quantum mechanical theory and mathematical formalism. Because the underlying principles of NMR pertaining to engineering are thankfully accessible through classical physics, the topic of quantum mechanics is addressed only for purposes of clarifying terminology and noting where intuition breaks down. What follows is a discussion on the established laws governing magnetic resonance in which the relevant concepts are treated systematically.

According to our modern understanding, an atom can be described as a nucleus surrounded by one or more electrons that occupy relatively removed and probabilistic orbits. For most elements, this nucleus consists of some combination of protons and neutrons held together via strong interaction. Ever more sophisticated experiments conducted in particle physics have shown that such nuclear constituents are, in turn, composed of quarks and gluons (3), which represent fundamental ingredients of matter at the periphery of our knowledge of the very small. Of particular importance to NMR is that these miniature particles exhibit an intrinsic and immutable property known in quantum mechanics as spin. While the term spin might cause one to infer there is a rotation taking place, and indeed rotation forms the closest analogy in classical physics, it is actually an abstract concept that cannot be explained beyond the empirical behavior observed (4). As a result of the spin contributed by individual quarks, atomic nuclei are also shown to possess spin as a whole, defined by the spin quantum number $s = \frac{n}{2}$, where n is a non-negative integer (5). Isotopes with odd mass numbers — i.e, ^1H, ^{13}C, ^{31}P, ^{129}Xe — have half-integer spins in their ground state and demonstrate NMR (6). The most abundant isotope of hydrogen, ^1H, contains a single proton in its spin-$\frac{1}{2}$ ($s = \frac{1}{2}$) nucleus.

Another property of quarks that bears relevance to this discussion is their charge. The lone proton of ^{1}H is formed of three quarks: two "up" quarks and one "down" quark, with electric charges of $+\frac{2}{3}e$ and $-\frac{1}{3}e$, respectively, where e represents the physical constant of elementary charge (4). Besides conferring a net charge of +e to the nucleus, these quarks also create a sort of dipole, given the positive-negative opposition they display. Such dipolar characterization will become important for subsequent commentary on how NMR-active nuclei orient themselves when subjected to external influence. If we entertain the inaccurate but conceptually useful idea that a nucleus with spin is rotating on an imaginary axis, this movement of charge must induce a magnetic field, in keeping with classical physics. Hence, hydrogen and other NMR-active nuclei are commonly depicted as spinning magnets.

The famous Stern-Gerlach experiment of 1922 provided incidental evidence of spin in relation to magnetic properties, despite being designed to interrogate a pressing hypothesis of the time: that electrons possessed quantized orbital angular momenta (7). In this experiment, an inhomogeneous magnetic field was constructed through which a beam of neutrally charged silver atoms carrying a single valence electron was passed. Because electrons were impossible to test in isolation owing to their charge and small mass, which would undergo massive field-dependent deflection, the neutral silver atoms had served as passive vehicles for their transport. The underlying rationale was that orbital angular momenta exhibiting classical behavior must cause a continuous range of deflections, based on the orientation of incoming atoms, that would be exaggerated by field inhomogeneity; whereas quantized orbital angular momenta must yield an odd number of theorized deflections (8). To the dismay of the experimenters, neither case was observed, but rather

a splitting of the beam into two distinct lines of deflection. While not appreciated at the time, this finding provided the first evidence of electron spin, later postulated by contemporary graduate students Uhlenbeck and Goudsmit.

In the aftermath of the Stern-Gerlach experiment, Wolfgang Pauli and others had made great strides toward advancing the theoretical underpinnings of spin and the intimately related concept of spin angular momentum (9). As Pauli had conceived of it, spin angular momentum, denoted conventionally by $\mathbf{S}$, was a quantized vector with both magnitude and direction. Its magnitude is given by $\frac{h}{2\pi}\sqrt{s\,(s+1)}$, where h is Planck's constant 4.14 x 10^{-15} eV s and s is the previously defined spin quantum number. The number of directions this vector can assume follow a pattern of 2s + 1, and these directions are defined by the magnetic quantum numbers, m = -s, -s+1, …, s - 1, s. Implications of the Heisenberg uncertainty principle make a projection of $\mathbf{S}$ onto the z-axis most appropriate for representing orientation, given that only the position along one axis may be determined in quantum mechanics, while positions along other axes remain equally probable (10). For a spin-$\frac{1}{2}$ particle like ^{1}H, the magnitude of $\mathbf{S}$ is $\frac{h}{2\pi}\sqrt{\frac{3}{4}}$, and magnetic quantum numbers m= +$\frac{1}{2}$ and -$\frac{1}{2}$ confer relative direction with associated probabilities α and β, respectively. Figure 3.1 provides an illustration of this quantized spin angular momentum for ^{1}H in which $\mathbf{S}$ is shown to trace a cone of possible orientations related to either the +$\frac{1}{2}$ or -$\frac{1}{2}$ quantum states (the so-called magic angle, θ_m, that either vector makes with respect to the z-axis can be computed as $\cos^{-1}\left(\frac{h}{2\pi}\sqrt{\frac{3}{4}} \div \frac{h}{2\pi}\frac{1}{2}\right) \sim 54.7°$). As it turns out, the same quantum states representing spin were
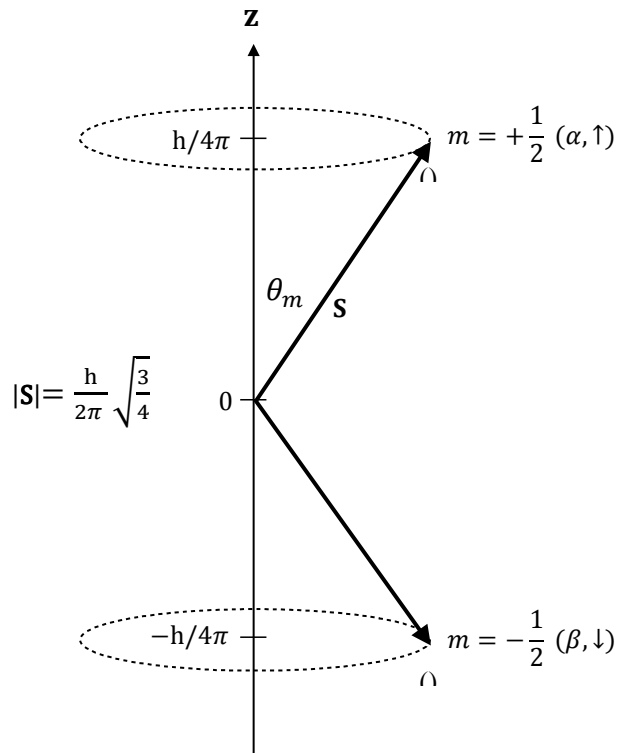
Figure 3.1. Nuclear spin. Spin-1/2 nuclei like the proton of ¹H can exist in a superposition of +1/2 (↑) and -1/2 (↓) quantum states that have associated probabilities of α and β, respectively. Spin angular momentum vectors denoted by S have a magnitude |S| and a direction that points away from the z-axis by the magic angle θ_m, with multiple orientations being equally probable in x-y according to Heisenberg's uncertainty principle, as shown from the dotted trace.

nt and fully

Having provided some preliminary context, the classical description of NMR follows in a natural

manner. As previously mentioned, depicting nuclei with half-integer spin as rotating magnets is

inaccurate from the standpoint of quantum mechanics, but will prove useful in showing how they

behave in a practical sense. The movement of charge under such rotation is what gives rise to the magnetic properties of the nucleus, and may be interpreted to confer a "north" and "south" pole like that of a regular magnet. In the presence of an external magnetic field, NMR-active nuclei express a familiar tendency to align themselves to the field by virtue of their own magnetism; accordingly, a magnetic dipole moment, μ, is shown to exist. It becomes clear from Figure 3.2 that this alignment takes on a characteristic response with regard to the applied magnetic field, denoted by B. As the nucleus revolves about an imaginary axis specified by μ, there is also observed a rotation of μ about B, traced by the dotted line in the figure. This secondary rotation occurs as a result of the torque, Γ, that B exerts on μ, which can be expressed as a rate of change in angular momentum — considered here in a classical sense:

$$\Gamma = \frac{dS}{dt} = \mu \times B \qquad \text{(Eq. 3.1)}$$

From the perspective of physics, the precession of the nucleus bears a strong analogy to a whirling top that wobbles in response to gravitational torque, while conserving angular momentum. In this case, the torque represented by the cross-product indicates that Γ, dS, and dμ are orthogonal to both μ and B, and, according to the negative sense of the right-hand rule (infra supra), pointing into the page (Fig. 3.2). Although somewhat counter-intuitive, dμ points in a different direction from μ.

Vector μ importantly relates to angular momentum via a constant of proportionality known as the gyromagnetic ratio (γ), which is specific to individual nuclei and empirically determined:

$$\mu = \gamma S \qquad \text{(Eq. 3.2)}$$

Multiplying equation 2.1 by gamma thus gives

$$\frac{d\mu}{dt} = \mu \times \gamma B \qquad \text{(Eq. 3.3)}$$
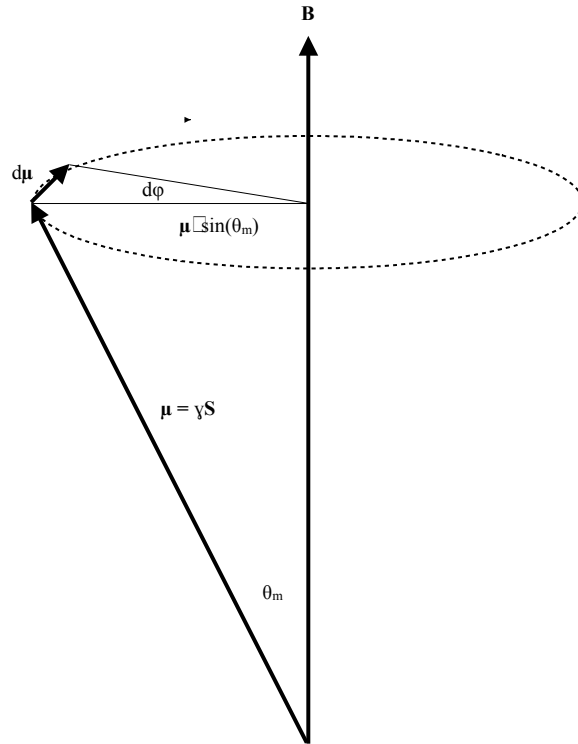
Figure 3.2. Magnetic dipole moment. The magnetic dipole moment μ precesses about external field B at the magic angle θ_m. For ^{1}H, this precession occurs counter-clockwise to the direction of B at a rate of dφ/dt. The instantaneous change in μ, represented by dμ, is orthogonal to both B and μ, and accordingly points into the page. Torque Γ exerted by B on μ shares the same direction as dμ.

Because bioengineering applications of NMR concern an ensemble of nuclei rather than a single nucleus, we can sum over a unit volume of μ to obtain the magnetization vector M (5):

$$\frac{dM}{dt} = M \times \gamma B \qquad\qquad (Eq.\ 3.4)$$

The advantage of using this formulation is that it perfectly describes the scale of system ordinarily studied without having to resort to relativistic quantum mechanics and the associated complexity. Solving Eq. 3.4 (see Section 3.6) reveals the most fundamental relationship in NMR: that M precesses about B at a rate determined by γ whose units $[\frac{rad}{s \cdot Tesla}]$ show a dependence on the strength of the applied field. Explicitly, this rate, termed the Larmor frequency, is expressed as

$$\omega_o = -\gamma B \qquad\qquad (Eq.\ 3.5)$$

, where ω_o represents the angular frequency $[\frac{rad}{s}]$ of precession demonstrated by M in the presence of a magnetic field with flux density, or strength, B [Tesla]. The negative sign indicates the direction of precession, designated according to convention.

By examining the γ of ^{1}H, determined as $267.52 \times 10^6 \frac{rad}{s \cdot Tesla}$, we can see that a 1 Tesla magnetic field would generate a resonant precessional frequency of $267.52 \times 10^6 \frac{rad}{s}$ with respect to the magnetization vector. To provide a sense of magnitude, this translates into 42.577 million rotations per second when equivalently represented using linear terms: $\frac{\gamma}{2\pi}$ $[\frac{MHz}{Tesla}]$. Because the sign of γ is positive for ^{1}H, Eq. 3.5 shows that precession occurs in the negative sense —- i.e., by way of counterclockwise rotation observed relative to the direction of B (4). While most NMR-active nuclei exhibit positive gyromagnetic ratios like ^{1}H, some, including ^{15}N and ^{17}O, display negative ratios that manifest as clockwise precession of the magnetization. The differences in sign demonstrated among the γ of these nuclear species bears no practical implication for NMR, though the magnitude of γ will be shown to dictate the amount of signal that one can obtain.

3.3 Magnetization

Without external influence, the magnetization vector M depicted in the previous section points in the same direction as the applied magnetic field. From the perspective of individual ^{1}H nuclei, however, a magnetic moment may align itself in either a parallel (n+) or antiparallel (n-) configuration with respect to this field, which corresponds to the $+\frac{1}{2}$ and $-\frac{1}{2}$ quantum states,

respectively. While only these two quantum states can be measured, the Copenhagen interpretation of quantum mechanics describes ^{1}H as being able to assume a variety of quantum states that are a linear combination of $+\frac{1}{2}$ and $-\frac{1}{2}$, making the n+/- convention useful but descriptively inaccurate (4,11). The potential energy, E, of a magnetic moment, given its principal orientation to the field, takes the form

$$E = - \mu \cdot B_{z,o} \qquad \text{(Eq. 3.6)}$$

where $Bz_{,o}$ is a static magnetic field along the z-direction (5). According to this relationship, both the strength of the magnetic moment and surrounding field are shown to contribute to the overall potential energy of the system. The definition of E related above is fundamental to NMR and underlies the quantum mechanical Hamiltonian operator that evaluates the set of possible energies that may be assumed by a spin system as it evolves over time (8).

Owing to the diametric alignment of magnetic moments in the presence of $B_{z,o}$, n+ and n- nuclear populations occupy distinct energy levels whose relative separation is expressed by

$$\Delta E = \frac{h}{2\pi} \gamma\, B_{z,o} = \frac{h}{2\pi} \omega_o \qquad \text{(Eq. 3.7)}$$

with ΔE being the difference in potential energy. The disparity between the two energy states is seen here as depending only on the strength of $B_{z,o}$ and the ɣ specific to ^{1}H, such that increasing the field has the proportional effect of widening the energy gap. As alluded in the latter form of Eq. 3.7, which resembles the Einstein-Planck relation (12), it is the Larmor frequency that governs the transmission of energy across ΔE; other frequencies are therefore of lesser consequence to the two-state system illustrated. Because the most energetically favorable configuration of the magnetic moment is in alignment with the direction of the field, n+ nuclei are slightly more probable than their anti-aligned counterparts, which have greater energy. This slight bias toward

n+ nuclei accounts for the observable NMR signal, however the transitional energy (ΔE) promoting the conversion between these two configurations is small. Given that thermal energy resulting from various forms of atomic motion can exceed ΔE, relative populations of n+ and n- are probabilistically determined on the basis of the Boltzmann distribution:

$$\frac{n-}{n+} = e^{-\Delta E/kT} \qquad \text{(Eq. 3.8)}$$

, where k is the Boltzmann constant, 8.62×10^{-5} eV K^{-1}, and T is the absolute temperature in Kelvin (K). Under standard conditions, the populational difference favoring the n+ orientation amounts to only a few nuclei per million within a sample, making NMR a fairly insensitive technique.

At the macroscopic level, this polarization of magnetic moments produces a net equilibrium magnetization, $M_{z,e}$, along the direction of $B_{z,o}$ (5):

$$M_{z,e} = \frac{N \gamma^2 \left(\frac{h}{2\pi}\right)^2 I_z(I_z+1)B_o}{3kT} \qquad \text{(Eq. 3.9)}$$

, where N is the number of ^{1}H nuclei and I_z is the quantum mechanical spin operator, defined along z as +/- 1/2. Since $M_{z,e}$ dictates the maximum amount of signal that can be generated via NMR, considerable attention is paid to its contributing factors. With regard to ^{1}H, having a natural isotopic abundance of 99.9844% (13), N is ensured to be relatively high, as most biological tissues derive the bulk of their mass from water and contain a wide range of organic compounds. Compared to other stable nuclei exhibiting half-integer spin, ^{1}H also demonstrates the largest gyromagnetic ratio while showing similar spin characteristics. For these reasons, ^{1}H constitutes the most utilized nuclear species for NMR, and is emphasized as the primary focus of this work. Enhancing equilibrium magnetization through manipulation of $B_{z,o}$ and T is typically application- and instrument-dependent and carries a variety of trade-offs that impose practical limits on what can be achieved.

3.4 Excitation & Detection

Harnessing the potential of $M_{z,e}$ for imaging necessarily requires introducing energy in such a way as to cause a deviation from the equilibrium state. This can be accomplished through the application of a radiofrequency (RF) pulse that oscillates at the Larmor frequency. Inasmuch as an RF pulse is itself a magnetic field, there is a potential to effectively impart energy to an ensemble of nuclei by matching their rate of precession, in accordance with the resonance condition stated by Eq 3.5. Recalling the earlier depiction of $M_{z,e}$ that has developed as a result of the static field $B_{z,o}$, it can be shown that application of RF pulse $B_{1,x}$ along the positive x-axis induces a torque on the magnetization vector, depicted in Figure 3.3. As the torque causes the magnetization vector to tip away from its initial position along the z-axis, this magnetization (now simply termed M) would be observed to simultaneously spiral around $B_{z,o}$ at resonance. To simplify the vectorial representation of M undergoing such nutation, I will here introduce the rotating frame as that which follows the path of magnetization at the Larmor frequency, thereby isolating the specific motion of deflection from z. Using this frame of reference, the torque of $B_{1,x}$ clearly rotates M into the positive y-axis, whereupon the magnetization assumes some angular displacement (Fig. 3.3). Achieving a specific nutation, or "flip", angle entails applying a B_1 of sufficient amplitude to match the frequency of nuclear precession over a duration that determines the amount of torque being exerted:

$$\theta_{flip} = \gamma\, B_1\, t \qquad\qquad\qquad \text{(Eq. 3.10)}$$
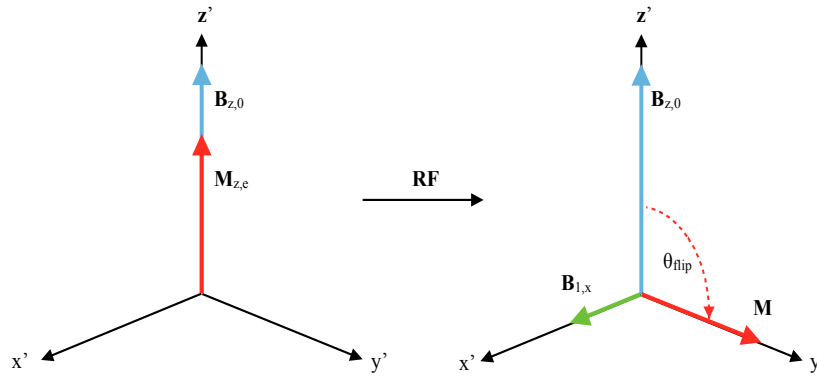
Figure 3.3. RF excitation. In the context of the rotating frame, equilibrium magnetization $M_{z,e}$ points along the main field, which is aligned to z' by convention. During RF excitation, $B_{1,x}$ exerts a torque on M that causes its rotation about x' in the z'-y' plane. Because of the positive γ of ^{1}H, the direction of rotation is toward y', with a nutation angle described by θ_{flip}. If regarding the excitation process in the laboratory frame, M is seen to undergo complex nutation with influence from both $B_{z,0}$ and $B_{1,x}$.

where θ_{flip} [rad] is the flip angle, B_1 [Gauss] is the RF amplitude, and t [μs] is the duration of B_1. Neglecting, for now, the specifics of RF pulse design, the production of B_1 from a hardware standpoint requires the assembly of an RC circuit that is tuned to the resonant frequency of the nucleus of interest:

$$\omega_o = \frac{1}{\sqrt{LC}} \qquad\qquad\qquad \text{(Eq. 3.11)}$$

where ω_o is the Larmor frequency $[\frac{rad}{s}]$, L is the inductance [H], and C is the capacitance [F]. Driving a current through the modeled circuit creates the B_1 field and is responsible for modulating its amplitude. In order to transmit B_1 in a manner that will result in a torque on M, this circuit or coil must be oriented orthogonal to the direction of the main field, denoted previously as $B_{z,o}$. Such coils are often shaped and used independently or arrayed together, depending on a host of accompanying design factors that exceed the scope of this discussion.

Without perturbation, magnetic moments exhibit a random distribution of phase with regard to their precession about $B_{z,o}$. Following B_1 transmission, many of these magnetic moments will acquire phase coherence, which allows for M to have a non-zero component apart from equilibrium along z. Of particular importance to NMR is that any flip induced by B_1 generates a transverse component of coherent magnetization that precesses along the x-y plane. This magnetization can then, in reciprocal fashion, be received by the same coil, given Faraday's law of induction, wherein the change in magnetic flux — owing here to the precession of M_{xy} — induces an electromotive force (EMF) or voltage that drives a current (14). As the magnitude of transverse magnetization determines the amount of EMF produced by the receive coil, it becomes clear that the optimal flip angle (θ_{flip}) for excitation in order to maximize the signal is $\frac{\pi}{2}$, or 90-degrees. The resulting time-varying signal detected immediately after excitation is called the free-induction decay (FID).

3.5 Relaxation

Following excitation with an RF pulse, an ensemble of nuclei will exhibit a general tendency to restore the initial equilibrium state. This process, known as relaxation, occurs as a result of the torque exerted by the main field and fluctuations in the field that individual atoms experience via molecular motion — i.e, translation, vibration, and rotation (4). From a vectorial standpoint, the post-excitation system is characterized by decay of the transverse magnetization (M_{xy}) in the x-y plane and simultaneous regrowth of longitudinal magnetization (M_z) along z. Owing to the underlying quantum mechanical basis for relaxation, these respective processes are not necessarily taking place at the same rate, meaning the value of $|M_{xy}| + |M_z|$ can change. Although the mechanisms governing relaxation are relatively complex and demand considerable commentary,

the basic understanding is presented here.

Based on early experiments evaluating modes of relaxation, it was shown that molecular tumbling played a substantial role in modeling how magnetization evolved (15). Such tumbling is represented by a rotational correlation time, τ_c, which expresses the average duration for a molecule to rotate 1 radian. As might be expected, the size of a molecule undergoing rotation has a significant impact on tau, along with the viscosity, temperature, and ionic content of the surrounding environment (16). Given the magnetic properties of nuclei, the correlation time can also translate into the frequency of interaction $(1/\tau_c)$ between the associated dipolar fields, and provide a sense for perturbations that might occur. In the context of NMR, the frequency of interaction relative to precessional resonance is indicative of the efficiency with which molecules transmit energy. Figure 3.4 illustrates the relationship that τ_c bears to the rates of relaxation, known by convention as T_1 for the growth of M_z and T_2 for the decay of M_{xy}. While T_2 can be seen to generally decrease with respect to increasing τ_c and molecular size, T_1 demonstrates an inflection point beyond which the opposite trend is observed. This inflection point exists due to the greater efficiency of energy dissipation that occurs as $1/\tau_c$ nears resonance, and moves away from tumbling regimes at either extreme. Because of its strong dependence on B_o, T_1 is observed to increase with the application of higher field strengths, thereby changing its relation to τ_c accordingly.

Longitudinal relaxation, characterized by T_1, requires the exchange of energy between nuclei and their environment through the medium of magnetic fields. As mentioned above, this exchange is
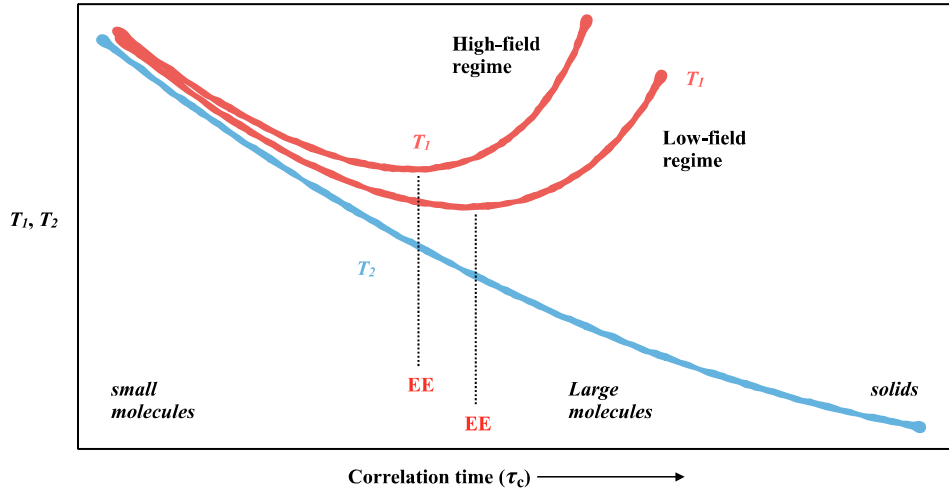
Figure 3.4. Correlation time. General trends for T_1 (red) and T_2 (blue) relaxation with regard to correlation time (τ_c). The high- and low-field regimes of T_1 demonstrate inflection points where relaxation is most energetically efficient (EE). Viscosity necessarily increases with τ_c in moving from an environment of small molecules in solution to the more rigid architecture of solids.

r

f

t

r

r

v

N

(~65%) of $M_{z,e}$. Excitation of a system at equilibrium with a $\frac{\pi}{2}$ pulse transfers all of the

magnetization into the transverse plane, thus nullifying $M_{z,i}$:
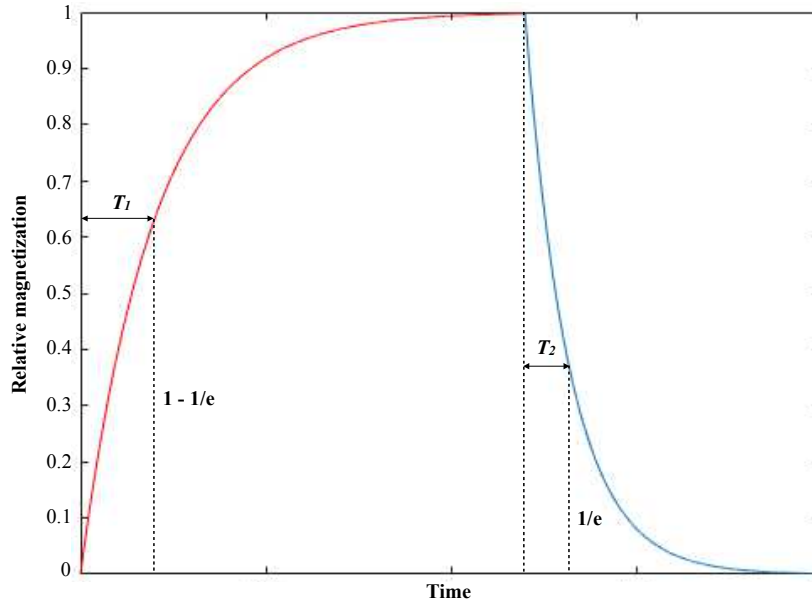
Figure 3.5. T_1 and T_2 relaxation. Longitudinal magnetization (M_z), depicted by the red trace, relaxes exponentially toward equilibrium according to T_1, while the decay of transverse magnetization (M_{xy}), shown in blue, is governed by T_2.

$$M_z = M_{z,e}\left(1 - e^{-\frac{t}{T_1}}\right) \qquad \text{(Eq. 3.13)}$$

The behavior of M_z following excitation is illustrated in Figure 3.5, where the magnetization is shown to exponentially regrow toward equilibrium in the presence of Bo, according to the rate governed by T_1. At a macroscopic level, each tissue type represents a unique admixture of nuclear environments that contribute to a composite value of T_1.

As in T_1 relaxation, fluctuating magnetic fields are responsible for transverse relaxation characterized by T_2. However, because the latter relaxation mechanism additionally depends on fluctuations along z, T_2 values are often much shorter than those of T_1 (5). Local field perturbations resulting from dipolar interactions cause each nucleus contributing to transverse magnetization to take on a slightly different precessional frequency following excitation. In the process, the once

coherent magnetization begins to dephase and thus lose magnitude as individual magnetic moments fan out in different directions along the x-y plane, leading to vectorial cancellation. Again assuming a $\frac{\pi}{2}$ excitation at equilibrium, the decay of M_{xy} can be modeled by

$$M_{xy} = M_{z,e} \; e^{-\frac{t}{T_2}} \qquad \text{(Eq. 3.14)}$$

, with M_{xy} representing the transverse magnetization and T_2 explicitly being defined as the time over which M_{xy} decays to $\frac{1}{e}$ (~37%) of its initial value. In Figure 3.5, M_{xy} is seen to exhibit exponential decay with regard to the time constant T_2, following application of an excitation pulse of $\frac{\pi}{2}$. Owing to imperfections typically present in the main magnetic field (B_o), the actual decay of M_{xy} can be much more swift than the ideal case. Such B_o inhomogeneity produces off-resonance effects that induce further dephasing, based on the local changes to precession. The resulting modification to M_{xy} decay follows T_2*:

$$\frac{1}{T_2*} = \frac{1}{T_2} + \; \gamma \Delta B_o \qquad \text{(Eq. 3.15)}$$

where ΔB_o represents the deviation from B_o. Although T_2* can dramatically impact the characteristics of M_{xy} and its measurement, there are means of circumventing this challenge that will be addressed later. Aside from their ability to determine the amount of measurable magnetization, the importance of T_2 and T_2* derives from the fact that they can uniquely identify tissues of different composition, and accordingly form mechanisms of contrast like T_1.

3.6 Spectroscopic Signal

Precession and relaxation have thus far been treated in isolation for the purpose of simplifying how they are understood amid a larger context. When taken together, these properties of magnetization

describe the dynamic behavior of NMR that can be observed from experiments with phenomenological predictability. This behavior is recapitulated by the Bloch equations, which relate the effects of external fields to the time course of magnetization, here presented as

$$\frac{dM}{dt} = M \times \gamma B - \frac{M_x i + M_y j}{T_2} + \frac{(M_{z,e} - M_z)k}{T_1} \qquad \text{(Eq. 3.16)}$$

where $M = [M_x(t), M_y(t), M_z(t)]$; $B = [B_x(t), B_y(t), B_o]$; $M_{z,e}$ is the equilibrium magnetization; and i,j,k are unit vectors along x,y,z, respectively (17, 18). As mentioned earlier, the first term represents the precession of M about B, according to the nucleus-specific rate given by the gyromagnetic ratio. The last two terms deal with the relaxation processes of T_1 and T_2 whose characteristic effects on magnetization were provided in the preceding section. Using Eq. 3.16, one can model any number of field-based perturbations, though the computation may be rather intensive, depending on the complexity of the system. In the case of a typical $\frac{\pi}{2}$ (90-degree) RF excitation pulse that has tipped magnetization into the x-y plane, solutions take the form

$$M_x(t) = M_{z,e}\, e^{-\frac{t}{T_2}} \cos(\omega_o t) \qquad \text{(Eq. 3.17)}$$

$$M_y(t) = M_{z,e}\, e^{-\frac{t}{T_2}} \sin(\omega_o t) \qquad \text{(Eq. 3.18)}$$

$$M_z(t) = M_{z,e}\left(1 - e^{-\frac{t}{T_1}}\right) \qquad \text{(Eq. 3.19)}$$

with ω_o representing the Larmor frequency. Immediately following excitation, the M_x and M_y components of magnetization are seen to oscillate in magnitude at the rate of precession (ω_o), while experiencing T_2 decay. At the same time, M_z begins its regrowth toward equilibrium governed by T_1 relaxation.

Since M_x and M_y are related in their description of precession, they can be combined as M_{xy} to facilitate the analysis of transverse magnetization. By taking M_x to be the "real" component and
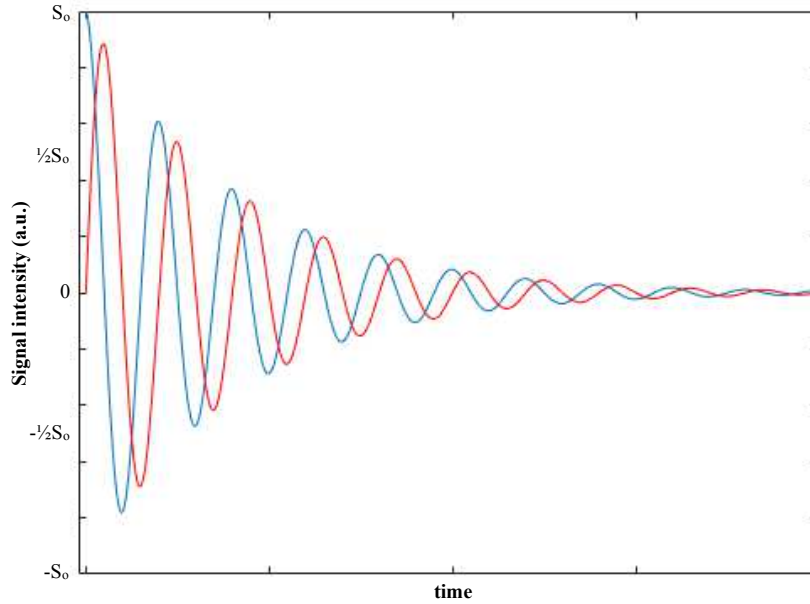
Figure 3.6. Demodulated signal from FID. Real (blue) and imaginary (red) signal components for a single nuclear spin undergoing free-induction decay according to T_2; S_o represents the initial signal corresponding to M_{xy} following excitation.

M_y the "imaginary" component of M_{xy}, we obtain

$$M_{xy}(t) = M_{z,e}\, e^{-\frac{t}{T_2}} \cos(\omega_o t) - i\, sin\,(\omega_o t) = M_{z,e}\, e^{-\frac{t}{T_2}} e^{-i\omega_o t} \qquad \text{(Eq. 3.20)}$$

where the final simplification has been made according to the Euler formula. M_{xy} is thereby shown to undergo precession about B_o in the transverse plane. This precession is observed by a receive coil as a time-dependent oscillating signal that undergoes T_2 dampening. Although the signal detected (and amplified) by hardware lies in the range of MHz, it ultimately becomes

demodulated by multiplication with sinusoidal and cosinusoidal waveforms of similar frequency, i.e., $\omega_o + \Delta\omega$, to isolate real and imaginary components in quadrature (17). Such demodulation produces signals in the range of kHz corresponding to the reference frequency $\Delta\omega$, along with side-bands of the form $2\omega_o + \Delta\omega$, which are removed via low-pass filtering (19). After analog-

52

to-digital conversion, the free-induction-decay (FID) of M_{xy} can be visualized on a scanner as oscillating principally around $\Delta\omega$, which lies at the center of an operator-defined bandwidth or sweepwidth (Figure 3.6).

Of particular interest to NMR is that the acquired FID for any given sample is modulated by a range of frequencies centered about the reference $\Delta\omega$. While the rate of nuclear resonance reflected in this signal is largely governed by B_o, it is also influenced through locally induced fields. As negatively charged electrons move about their probabilistic orbits, they generate a current with an associated magnetic field that can either align with or against B_o and, thus, alter the effective field that is experienced by individual nuclei. The extent to which electrons "shield" the applied field determines the actual frequency of precession at resonance, with faster precession being observed in situations where shielding has been diminished. Depending on the surrounding chemical environment, there exist a variety of mechanisms for altering the amount of nuclear shielding. For example, molecules with more electronegative substituents tend to de-shield ^1H nuclei owing to electron-withdrawing characteristics that, in turn, facilitate faster resonance. This can be illustrated by the hydrogens of CH_2Cl_2 resonating faster than those of CH_2Br_2 in a hypothetical experiment, given the augmented electronegativity of Cl relative to Br. The fact that different molecular functional groups express uniquely identifiable frequencies according to their local environment is the basis for spectroscopy.

With the diversity of precessional frequencies represented in the post-processed FID, one can appreciate its composite nature. The general modeling of this complex signal $S(t)$ retains the characteristic features of transverse magnetization:

$$S(t) = S_o \, e^{-\frac{t}{T_2}} \, e^{-i\omega_{cs}t} \qquad\qquad \text{(Eq. 3.21)}$$

where S_o is the initial signal of M_{xy} following excitation and ω_{cs} is the demodulated frequency $[\frac{rad}{s}]$ of the real and imaginary components relative to a reference, conventionally known as the chemical shift. Because each resonating ^1H inhabits a unique chemical environment, as described above, $S(t)$ is really a composite signal that represents a superposition of many S_o, T_2, and ω_{cs} values, which vary as a function of position within a sample. In order to extract the relevant frequency content of the time-varying $S(t)$, it is necessary to perform a Fourier transform $(\mathcal{F})$ (20), defined mathematically as

$$\mathcal{F}[S(t)] = S(\omega) = \int_0^\infty S(t)e^{-i\omega t}\, dt = \int_0^\infty S_o \, e^{-\frac{t}{T_2}} \, e^{-i\omega_{cs}t} \, e^{-i\omega t} \, dt \qquad \text{(Eq. 3.22)}$$

with $S(\omega)$ being the signal as a function of frequency and ω representing frequency $[\frac{rad}{s}]$. This transformation effectively decomposes $S(t)$ into its associated frequency components, such that the relative contribution of each precessional resonance can be represented in a spectrum described by $S(\omega)$. In practice, the Cooley-Tukey algorithm, or some variation of it, is employed to carry out the discrete version of this transform, having been optimized with regard to computation time (21).

The analytical solution of the Fourier transform presented in Eq. 3.22 demonstrates the spectral characteristics of the signal within the frequency domain:

$$S(\omega) = \frac{S_o \frac{1}{T_2}}{(\omega - \omega_{cs})^2 + \left(\frac{1}{T_2}\right)^2} + i \frac{-S_o(\omega - \omega_{cs})}{(\omega - \omega_{cs})^2 + \left(\frac{1}{T_2}\right)^2} \qquad \text{(Eq. 3.23)}$$

where the real and the imaginary terms represent the "absorption" and "dispersion" modes of the
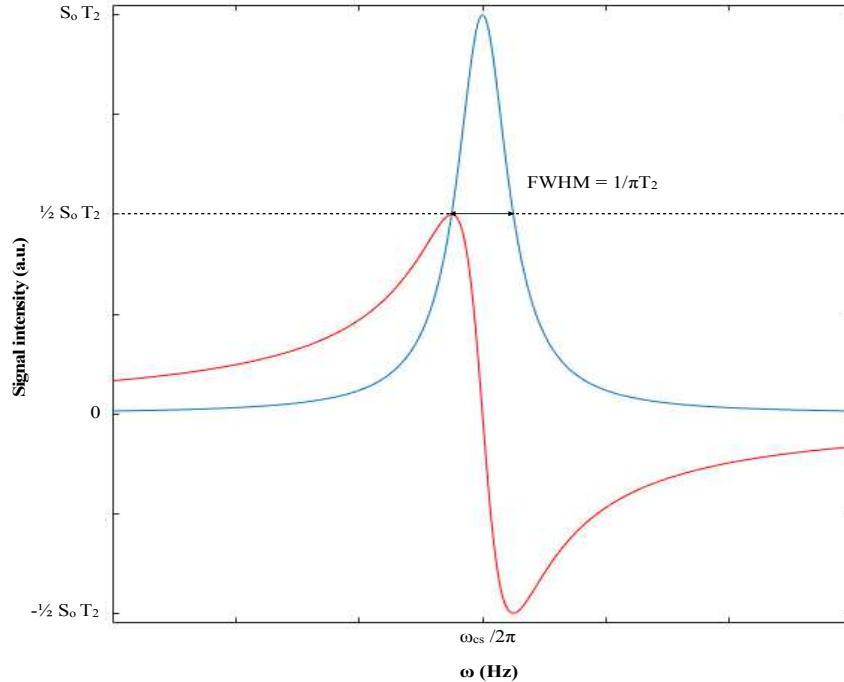
Figure 3.7. NMR Spectrum. Real (blue) and imaginary (red) spectra with Lorentzian lineshapes resulting from Fourier transformation of the respective FIDs for a single resonance centered at ω_{cs} /2π (Hz). The full-width-at-half-maximum (FWHM) of the real spectrum is defined by $1/\pi T_2$, while its amplitude follows $S_o T_2$.

complex spectrum, respectively (4, 22). Figure 3.7 illustrates the Lorentzian lineshapes of these two component modes whose phase is offset by 90-degrees, in the same fashion as the received signal, which has been mixed with sinusoidal and cosinusoidal waveforms. Considering a single resonance ω_{cs}, the component modes display a relative shift of $\omega = \omega_{cs}$ on the frequency axis, here shown in Hz as $\omega_{cs}/2\pi$. As might be expected based on the formulation of $S(\omega)$, T_2 strongly characterizes how individual resonances derive their particular shape. With regard to the commonly referenced absorption mode spectrum, the full-width-at-half-maximum (FWHM) of the Lorentzian is defined as $1/\pi T_2$ in Hz, and the maximum height is T_2 by comparative proportion when S_o is normalized to 1 (Figure 3.7). It follows that slow moving tightly bound nuclei, such as those found in lipid, which have shorter than average T_2/T_2* values, exhibit broadened signals with
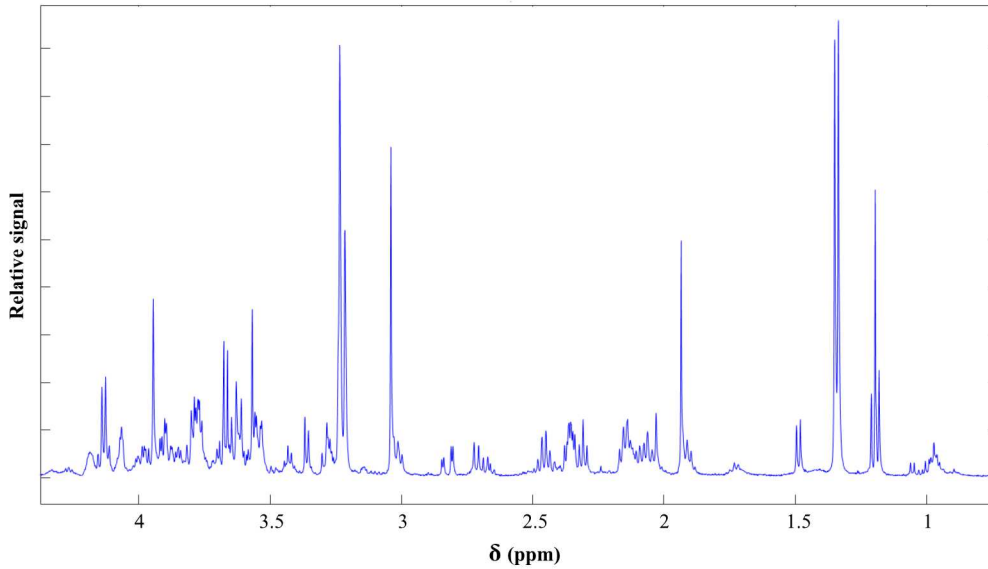
Figure 3.8. Glioma spectrum. *Ex vivo* [1]H HR-MAS spectra acquired from a glioma sample at 11.7T (500 MHz). Individual functional groups of various metabolites resonate with increasing frequency from right to left on the ppm scale.

lower overall amplitude. In order to optimally reduce experimental linewidths and improve spectral resolution, one must reduce the B_o imhomogeneity that impacts T_2* using supplemental field gradients to "shim" the main field (23).

The technique of NMR spectroscopy accordingly obtains information on the frequency of nuclear resonance from a volumetric signal that is agnostic to the position of the source. An important feature of spectroscopy is that the area under each resonance describes the relative proportion of nuclei contributing to the often multi-resonance signature of a molecule, and can therefore be used to infer composition, based on known empirical formulae. The frequency of every resonance in such a molecule is represented by its characteristic chemical shift (δ), defined as

$$\delta = \frac{\omega_{cs} - \omega_{TSP}}{\omega_{TSP}}$$ (Eq. 3.24)

56

, where ω_{TSP} denotes the known frequency of the reference compound trimethylsilylpropionic acid (TSP)(24). This definition of δ, with units of parts per million (ppm), was devised for assigning standard shifts to unique resonances in a manner that is independent of field strength, allowing their comparison across multiple instruments with varying B_o (to convert between ppm and Hz, one need only apply the relation $\delta[\text{ppm}]\,\gamma B_o = \delta[\text{Hz}]$). In Figure 3.8, sample NMR spectra from a glioma are shown on the chemical shift axis. By convention, δ increases from right to left, with 0 ppm corresponding to the reference peak of TSP (not shown), which exhibits tremendous electronic shielding. Chemical shifts observed further away from TSP, or "downfield", indicate nuclei with faster resonance, whereas shifts toward TSP, or "upfield", indicate slower resonance.

3.7 Coupling

While the signal processing interpretation of spectroscopy elaborated above has a strong mathematical underpinning that allows us to understand how frequency components can be discriminated from the time domain, it cannot account for the diversity of spectral characteristics typically on display. To fully appreciate the intricate nature of spectra, one must delve into the physics of spin interactions that determine the relative shape and location of each resonance. The earlier described concept of chemical shift may, in fact, be interpreted as an *interaction* between nuclear spins and B_o, which is modulated via electrons. Because electron clouds sometimes exhibit non-uniform geometry, both regionally and over the entirety of a molecule, in the case of aromatics, there exist a range of resonances associated with the orientation of the molecule relative to B_o. This gives rise to a resonance-broadening effect known as chemical shift anisotropy (CSA), which is most pronounced in condensed phase samples that restrict the orientation of molecules;

conversely, fluids manifest the least CSA owing to motional averaging. Although a variety of other interactions are possible within a sample, the purpose of this section is to introduce those which describe the magnetic coupling between ^{1}H spins typically demonstrated in spectra.

As a result of the magnetic field produced by each spin and propagated through space, we can anticipate how magnetic dipole moments will influence one another. The dipole-dipole (DD) coupling constant, designated by b_{jk}, for any two arbitrary spins j and k can be expressed as

$$b_{jk} = -\frac{\mu_o \gamma_j \gamma_k h}{8\pi^2 r_{jk}^3} \tag{Eq. 3.25}$$

where b_{jk} has units of rad/s; γ_j and γ_k represent the gyromagnetic ratios of the two spins; r is the distance [meters] separating j and k; h is Planck's constant; and $\mu_o = 4\pi \times 10^{-7}$ [Henry/m] is a necessary factor in SI units (4). From this relationship, the homonuclear interaction between ^{1}H spins can be given as a frequency that scales linearly according to γ and with the inverse cube of r. The DD spin Hamiltonian modeling spin evolution is importantly governed by the secular DD coupling term:

$$d_{jk} = b_{jk} \frac{1}{2}(3\cos^2\theta_{jk} - 1) \tag{Eq. 3.26}$$

with d_{jk} having units of rad/s and θ_{jk} being the angle formed between B_o and a vector pointing through j and k (4). Such formulation shows that DD coupling bears a strong orientation dependence with respect to nuclear alignment. Solving for the roots of $3\cos^2\theta_{jk} - 1$ in Eq. 3.26 reveals null points at $\theta_{jk} \sim \pm 54.74^o$, where coupling effects vanish from predictions of spin evolution (these roots, commonly known as magic angles, harken back to the discussion on magnetic dipole moments and the angular deflection they assume during precession in either $+1/2$ or $-1/2$ spin states). Since DD coupling is a mechanism for both T_1 and T_2 relaxation processes, it
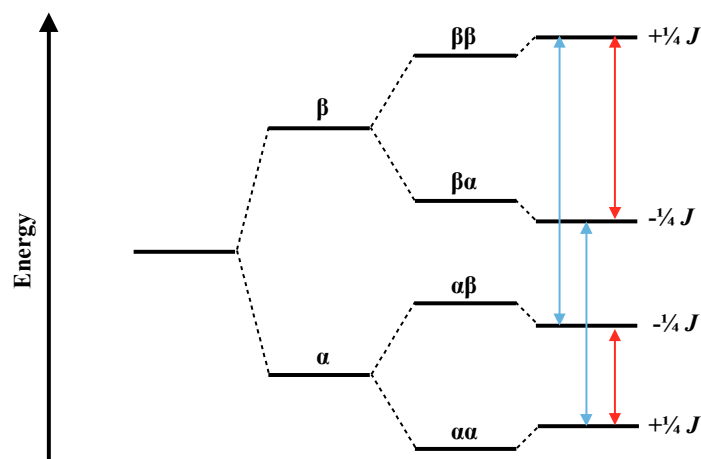
Figure 3.9. AX energy levels. Energy levels of a weakly coupled two-spin system that are influenced by way of *J*-coupling. Although not drawn to scale, in such a system, βα and αβ levels are relatively close together in energy (Hz) compared to αα and ββ (MHz). Blue arrows indicate transition frequencies of each resonance in the upfield spectral doublet; whereas red arrows indicate transition frequencies for the downfield doublet.

will naturally affect the amplitude and FWHM of spectra obtained from non-isotropic liquids and solids with biased nuclear alignments, while being motionally averaged away in isotropic liquids.

Besides the direct coupling between nuclear spins, there is also an indirect mechanism of magnetic interaction, mediated via intramolecular bonding electrons. When two or more spins are sufficiently close together, i.e., within 2-3 bond lengths, such *J*-coupling produces energy level splitting that translates into well-characterized spectral patterns. In the case of coupled nuclear spins A and X, one can permute the possible spin states as: $\beta\beta$ (↓↓), $\beta\alpha$ (↓↑), $\alpha\beta$ (↑↓), and $\alpha\alpha$ (↑↑), with both parallel and anti-parallel alignments. Figure 3.9 shows that each theorized spin state has an associated energy level, which depends on the strength of B_o. Because of hyperfine interactions with electrons that undergo their own alignment as spin-1/2 particles, these energy levels are altered either positively or negatively by an amount proportional to *J*-coupling constants (Fig. 3.9).

Values of J are given in Hz and exhibit field-independence. Of particular importance is that (single-quantum) transitions between energy levels involving one spin changing its state represent specific spectral frequencies, explicitly declared by: $\frac{\omega_X}{2\pi} - \frac{1}{2}J_{AX}$ ($\alpha\alpha \to \alpha\beta$), $\frac{\omega_X}{2\pi} + \frac{1}{2}J_{AX}$ ($\beta\alpha \to \beta\beta$), $\frac{\omega_A}{2\pi} - \frac{1}{2}J_{AX}$ ($\alpha\alpha \to \beta\alpha$), and $\frac{\omega_A}{2\pi} + \frac{1}{2}J_{AX}$ ($\alpha\beta \to \beta\beta$) (Fig. 3.9)(25, 26, 27). Thus, A and X display doublet (*d*) resonances centered at $\frac{\omega_A}{2\pi}$ and $\frac{\omega_X}{2\pi}$, respectively, where the two peaks of each *d* are separated by J_{AX}. By convention, all NMR-active spins representing a particular molecular spin system are designated alphabetically based on their chemical shift proximity. Since A and X lie far apart in the alphabet, they denote weakly coupled spins whose chemical shift difference is much greater than the associated coupling constant ($\delta_{AX} \gg J_{AX}$).

For weak coupling, the number of peaks observed from spectra follows the $n + 1$ rule, with n being the number of spins. Using this guideline, a lone hydrogen split by a neighboring methyl group (CH_3) would display a quartet (*q*), whereas the methyl group would present as a doublet; the ratio of these multiplet amplitudes conforms to Pascal's triangle as 1:3:3:1 (*q*) and 1:1 (*d*), neglecting the "roof effect" that slightly enhances spectral amplitudes in the direction of the coupling partner resonances. The example provided describes the AX_3 spin system of lactate, wherein the spin state energies of the inner peaks for A are equivalent (degenerate), thereby increasing their corresponding spectral amplitudes. Because the area under these curves is proportional to the relative number of nuclei and peak multiplicity provides information on the connectivity of molecular substituents, one can readily interrogate unknown substances from spectra.

When J is on the same order as the chemical shift difference ($\delta / J \sim 1$), complex coupling produces
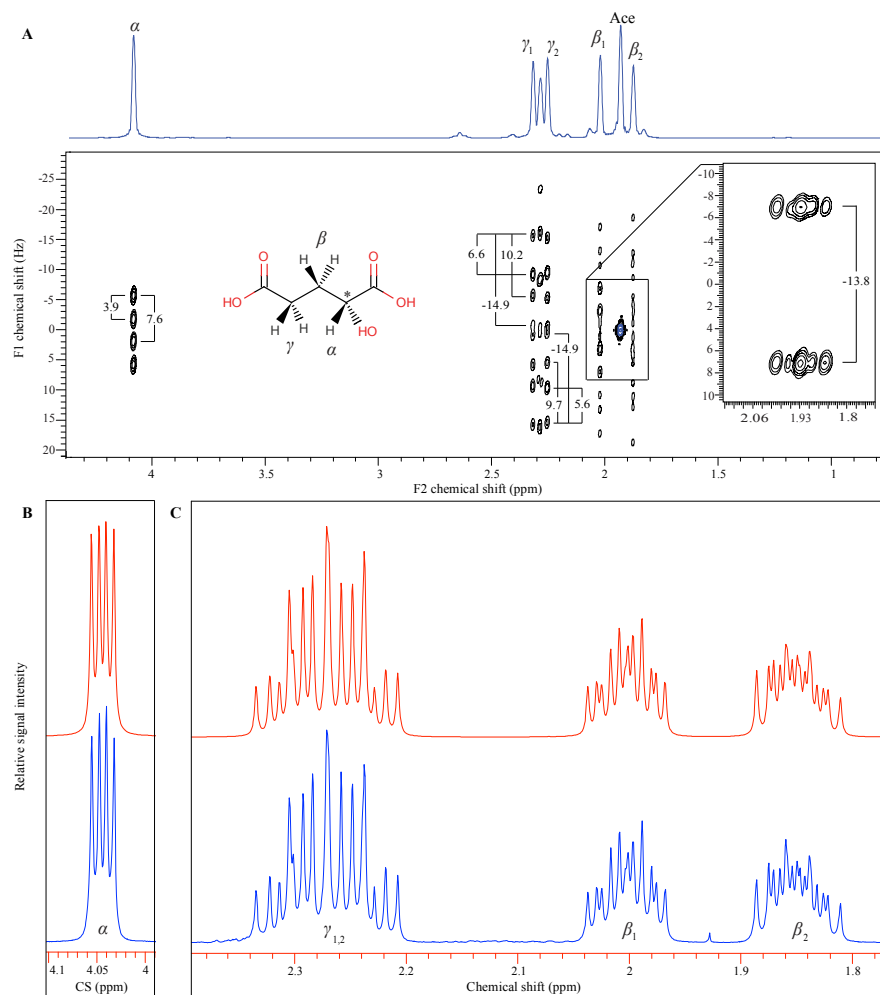
Figure 3.10. Complex coupling in AMNPQ spin system. *J*-resolved NMR spectra of 2HG at 11.7T (500 MHz) after 45° rotation shows empirically-derived coupling constants. The projection of F2 reveals a strong coupling artifact between γ-protons; acetate (Ace) was a by-product of 2HG formation. Inset depicts separate SERF experiment for resolving β-peaks (**A**). Reference NMR spectra from prepared solution of 2HG are illustrated by the blue trace, while spectra simulated from coupling and chemical shift information are shown in red (**B**,**C**).

second-order spectra due to the heightened interactions. Onco-metabolite D-2-hydroxyglutarate (2HG), aberrantly produced in *IDH*-mutant glioma, demonstrates this complex coupling owing to its AMNPQ spin system, which posseses five chemically distinct nuclei that resonate close together. To determine some of the intrinsic coupling constants of 2HG amid the complicated

spectral landscape, it was necessary to perform a 2-D J-resolved experiment, as shown in Figure 3.10A. Here, the spectra are rotated by 45-degrees on the two chemical shift axes (F1, F2) such that the diagonal and the resulting projection of cross-peaks are clearly visible along the indirect dimension (F2). A selective excitation and refocusing (SERF) variant (28) of the 2-D experiment was used to measure $^2J_{\beta1-\beta2}$, with an excitation band-selective uniform response pure phase (EBURP) pulse to selectively excite the β_1 multiplet, followed by a refocusing EBURP pulse to refocus both β_1 and β_2 (Figure 3.10A, inset). In Figure 3.10B,C, the chemical shift and J-coupling information obtained from the experiment was used to simulate 1-D spectra for 2HG (29).

An important implication of J-coupling is that the magnetization of each spin evolves independently in a process known as J-modulation (30). This leads to the phase of the spectra being modulated with different outcomes among the various molecular signals. Ensuring that these signals are upright and in-phase entails finding the optimal delay between excitation and detection, which will be some multiple of $1/J$.

3.8 CPMG

The broad repertoire of experiments available to spectroscopists allows for considerable tailoring based on the desired composition of the signal being investigated. In the most basic experiment known as the pulse-acquire, nuclei are excited with a 90-degree RF pulse, and, after some prescribed delay (τ), the resulting FID is received by the coil. Such a scheme can be parameterized according to a sequence of events whose timing determines the evolution of a signal: i.e., 90_x—τ –acq, where x represents the RF axis and *acq* stands for acquisition. Using this convention, it

becomes clear that the interval over which the signal evolves from excitation to acquisition, termed the echo time (TE), is simply τ. Following the recovery of longitudinal magnetization, one can repeat the pulse sequence in order to average the infinitesimally small signal over multiple scans and, thus, improve the SNR. To iterate through several scans in programmatic fashion entails specifying a repetition time (TR) that describes the interval between excitations. The number of repeated scans multiplied by the TR gives the total scan time of the sequence.

Although the pulse-acquire experiment offers several advantages with regard to the overall SNR, it is beset by issues stemming from NMR-active solvents that produce strong background signal. Under such circumstances, the solvent, being more concentrated than the molecules of interest, will manifest confounding spectra by virtue of the characteristically broad base of the Lorentzian lineshape. The essential problem lies in the fact that there is insufficient time available to establish T_2*-based contrast between dissolved compounds and the surrounding solvent before the former decays below the limit of detection. Thus, whenever possible, experiments are typically performed with deuterated (^{2}H) solvents like D_2O, which have completely different bandwidths of resonance apart from ^{1}H.

Experimental prospects changed with the foundational discovery made by Erwin Hahn relating to signal preservation. While irradiating samples with RF, Hahn observed the interesting phenomenon that one could, in part, recover signal as a "spin echo" using either a 180-degree or two 90-degree pulses following excitation (31, 32). By placing the 180-degree pulse exactly in the middle of the sequence, i.e., 90_x—τ—180_x—τ—acq, he managed to counter the effects of T_2* on excited nuclei, and instead promote the more protracted T_2 decay regime. The mechanism for this
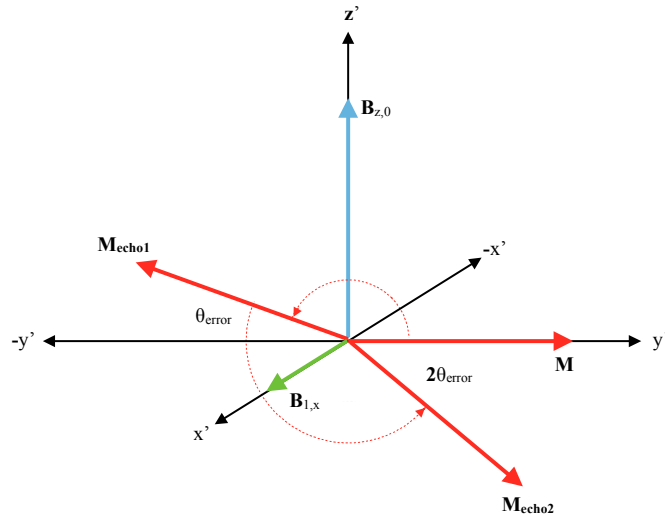
Figure 3.11. Carr-Purcell errors. Following excitation with $B_{1,x}$, magnetization vector M lies along the positive y-axis of the rotating frame. Application of an imperfect refocusing pulse π_x in a Carr-Purcell sequence causes magnetization at the first echo (M_{echo1}) to be angularly displaced by θ_{error} from the negative y-axis. With the second π_x pulse, magnetization (M_{echo2}) refocuses with an angular displacement error of $2\theta_{error}$ relative to the positive y-axis. Subsequent refocusing pulses further compound this error according to $n\theta_{error}$, while M alternates between the positive and negative y-axes. Rapid phase decoherence occurs as a result of the cumulative errors in the nutation angle.

phenomenon can be explained as a differential expression in phase ($\omega_{cs}\, t$) among the ensemble of

nuclei being interrogated. Once excited nuclei are allowed to freely precess in the transverse plane

over the first period of τ, they will each move at a frequency that depends on the local magnetic

environment. The resulting range of precessional frequencies gives rise to phase decoherence as

individual nuclei lose their original synchrony from excitation. If one then applies a 180-degree

refocusing pulse at time τ=TE/2, the de-phased spin vectors are flipped such that their direction of

evolution reverses and they begin to converge on the starting/readout position. Because the faster

precessing vectors are angularly displaced further away from the signal readout position, while the

slower precessing vectors are made closer to it, they meet at precisely the same time (2τ, TE),

having been rephased. The terminology of the echo refers to the fact that the acquired signal is

symmetric about the TE—increasing on one side and decreasing on the other, relative to the associated phase dispersion— or in effect echoing itself.

Recognizing the potential of this discovery, Henry Carr and Edward Purcell managed to further enhance the utility of the spin echo with a pulse sequence of their own. They devised a scheme wherein several 180-degree pulses are placed together in series, i.e., 90_x— $[\tau$ —180_x —$\tau]^n$ —acq ($n = 2, 3, 4 \cdots$), so as to propagate the signal generated at excitation over several decay cycles (33). This pulse train generates spin echoes every 2τ that successively decay in maximum amplitude according to a T_2 envelope, despite experiencing the effects of T_2* on an individual basis. Drawing from their experimental groundwork, the two physicists were able to develop a technique for measuring relatively long T_2 values by fitting the acquired signals to Eq. 3.14. However, because the refocusing pulses had non-ideal characteristics, producing less than 180-degree rotations of the magnetization, the derived mono-exponential curves systematically underestimated true decay. Figure 3.11 illustrates the implications of imperfect refocusing pulses for the Carr-Purcell sequence. In the context of the rotating frame, excitation from $B_{1,x}$ leads to the magnetization vector pointing along the positive y-axis. Subsequent application of a non-ideal refocusing pulse induces further yet incomplete rotation ($\pi - \theta_{error}$) toward the negative y-axis, which consequently demonstrates reduced magnetization in the transverse plane. As the ensuing pulses are played out, this magnetization alternates between the positive and negative y-axes, with accumulating rotational errors that hasten the loss of phase coherence.
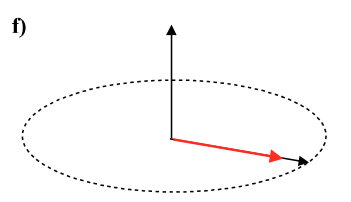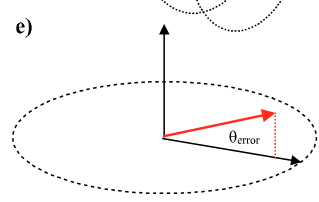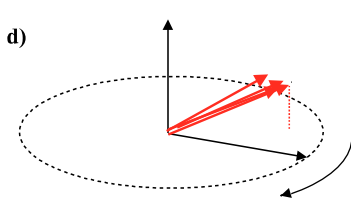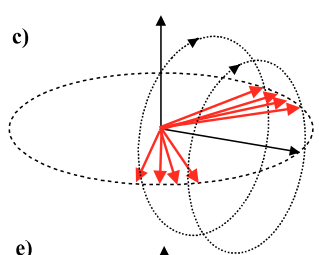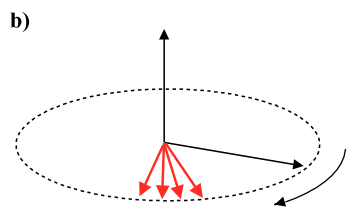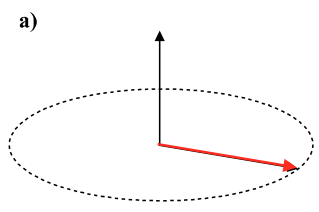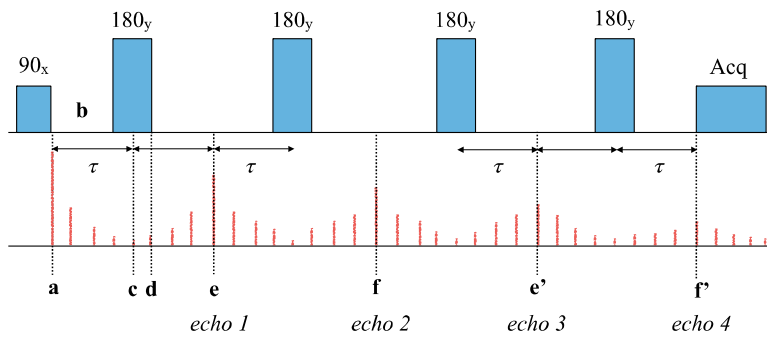
cumulative errors, as demonstrated above. Given the difficulty associated with producing ideal pulses, contemporary scientists S. Meiboom and D. Gill formulated an alternative approach to improve upon the performance of the sequence that emphasized pulse delivery (34). By shifting the phase of the refocusing pulses by 90 degrees relative to excitation, i.e., 90_x— $[\tau$ —180_y —$\tau]^n$ —acq (n= 2, 3, 4 ···), they were able to demonstrate a measurable increase in the fidelity of the signal over time, which more accurately modeled T_2 decay. This improvement can be explained mechanistically through the compensatory effect of the phase shift, illustrated in Figure 3.12. With the magnetization residing, as before, on the positive y-axis of the rotating frame following excitement by $B_{1,x}$, we can imagine it to evolve in the transverse plane due to off-resonance ($\omega \neq \omega_o$) while undergoing simultaneous dephasing. Subsequent application of an imperfect refocusing pulse $B_{1,y}$ at time τ causes the dephased magnetization to rotate about y. Although the rotation is non-ideal ($\pi - \theta_{error}$) and leads to rephasing above the transverse plane, repeating the pulse after 2τ automatically corrects the nutation angle by returning the spins to their original alignment in x-y. This cyclical process continues for the duration of the eponymous Carr-Purcell-Meiboom-Gill (CPMG) sequence, with magnetization refocusing along the positive y-axis at each echo, rather than alternating directions.

The timing of refocusing pulses in the CPMG sequence plays a critical role in determining how the signal evolves for a particular spin system via J modulation. Here we define the time between consecutive 180-degree pulses as t_{ref}, such that the associated repetition rate of a pulse train is $1/t_{ref}$. In the case of a strongly coupled AB system, where the coupling constant J_{AB} is on the same order as the chemical shift difference δ_{AB}, Allerhand approximated the modulation frequency to be ½ J_{AB} (35). However, under conditions of very high pulse rates, indicated by $|J_{AB}|\, t_{ref} \ll 1$ and $|\delta_{AB}|$

$t_{ref} \ll 1$, the decay of the signal becomes unmodulated, despite strong homonuclear coupling. The significance being that without a rapid pulse regime, strong coupling causes a considerable reduction in the apparent T_2, which is manifest as bi-exponential decay for metabolites like glutamate and glutamine (36). When the pulse rate fails to satisfy the criteria presented above, the amplitude of J modulation necessarily depends on a factor R t_{ref}, with

$$R = \sqrt{\delta_{AB}{}^2 + J_{AB}{}^2} \qquad \text{(Eq. 3.27)}$$

representing the difference between partially mixed spin state energy levels for $\beta\alpha$ and $\alpha\beta$ (34). These results are generalizable to other strong coupling systems and provide guidance for designing experiments to maximize signal. Although *ex vivo* applications permit large duty cycles that support near constant irradiation by refocusing pulses, implementing the sequence *in vivo* faces limitations on how much energy can be deposited in tissue from pulse power, according to the specific absorption rate (SAR)(37).

Owing to its robust performance across multiple applications, the CPMG has been used rather extensively in NMR. Such robustness is highlighted under conditions of inhomogeneous magnetic fields and gradients, where the CPMG maintains signal fidelity as an extension of the self-correcting property lent by dual RF axes (38). Based on these commonly encountered field inhomogeneities, which can have both static and dynamic contributions, the CPMG may also be applied to the study of quantum information processing (QIP), dealing with very small-scale interactions (39, 40). Perhaps more important to common usage, however, is the ability of the sequence to filter broad signals from samples that contain macromolecular contaminants. In experiments involving tissue, for example, lipid resonances can overwhelm the signal of interest and produce low-frequency distortions in the spectral baseline representative of the enlarged range

of precessional rates. To improve spectral quantification, the lipid signature is allowed to decay over the course of several hundred refocusing pulses due to its relatively short T_2 characteristics. For similar reasons of performance stability demonstrated above, the CPMG has also been employed for the measurement or estimation of slow timescale dynamic processes like T_1, T_2, diffusion, and chemical exchange (41, 42).

3.9 HR-MAS Spectroscopy

How NMR experiments are carried out depends critically on the phase of the material under investigation. For isotropic liquids whose molecular motion is approximated as the same in all directions, the effects of dipolar coupling and CSA are reduced through the averaging of spin orientation. More structured materials like tissue, however, restrict the motional freedom of spins and display spectra with severe line broadening as a consequence of spin interactions. The NMR technique known as high-resolution magic angle spinning (HR-MAS) spectroscopy was developed to overcome such issues with solid-state experiments. In HR-MAS, a sample is placed inside a rotor that is spun at the magic angle ($\theta_m \sim 54.74°$) with respect to the main field, as illustrated in Figure 3.13. By aligning the sample to the magic angle during rotation, one can minimize scaling of the dipolar coupling Hamiltonian that bears an orientation factor $3\cos^2\theta - 1$ (see Section 3.7), since θ_m forms a root to this second-order Legendre polynomial (43, 44). Rotating the sample simulates a more isotropic environment because of the motional averaging that reduces the impact of dipole-dipole and, to a lesser extent, CSA interactions on spectra. While the effects of dipolar coupling are substantially diminished upon spinning at the magic angle, CSA can still cause
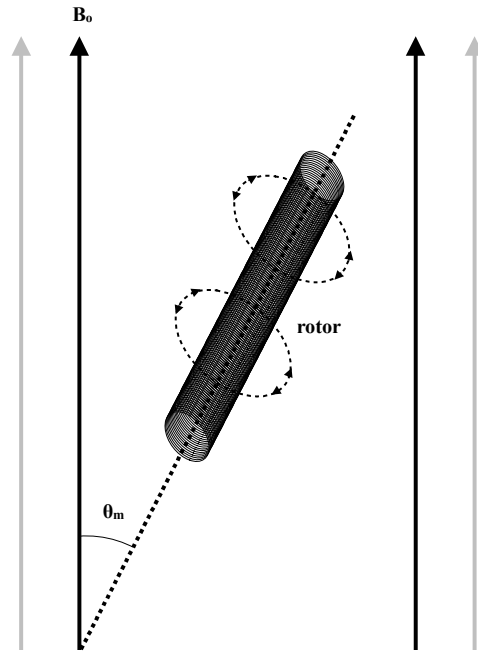
Figure 3.13. HR-MAS spectroscopy. In the solid-state NMR technique of HR-MAS spectroscopy, certain spin interactions are reduced by rotating samples about an axis that is oriented at the magic angle (θ_m) with respect to B_o. The rotor houses the sample and can be spun in either direction to facilitate motional averaging.

spectral artifacts if the rate of sample rotation ω_r is insufficient: i.e., whenever ω_r is less than the frequency of CSA interactions (45). These artifacts appear as sidebands in the spectra around the isotropic resonances at a distance of $\omega_r / 2\pi$ in Hz, and have an amplitude that depends on the CSA tensors (45). For tissue specimens of the brain an appropriate $\omega_r / 2\pi$ would be on the order of 2200 Hz to keep sidebands outside the bandwidth of interest (see Figure 3.8), whereas more solid substances may require rotation in excess of 50kHz.

Due to the ultra-high field strength of NMR spectrometers and compensation for condensed phase samples, HR-MAS experiments exhibit extraordinary spectral resolution. Multipulse sequences such as the CPMG help further improve linewidths and can even be designed to refocus magnetization with ω_r in mind, based on the period of rotation. The collective utility of HR-MAS

methodology allows for robust metabolomic probing of brain tumor samples acquired via intra-operative tissue sampling, which is an early focus of the research presented here.

3.10 *In vivo* Carr-Purcell PRESS

While the principles of NMR, undergirded by quantum mechnanics, are universally applicable to systems involving magnetic resonance, it is customary to reserve the designation of NMR for *ex vivo* techniques. The *in vivo* analogue to NMR is known as magnetic resonance spectroscopic imaging (MRSI) and deals with a unique set of challenges regarding the acquisition of patient data. Generally speaking, MRSI utilizes lower field strengths, has less sensitive coil configurations, and more field heterogeneity as compared to NMR, but its benefit is being able to study disease in an intact biological setting, without modeling and or oversimplification of the system. Whereas NMR affords considerably greater spectral resolution and sensitivity important for biomarker development and fine-level characterization, MRSI offers a platform to validate the diagnostic utility of such markers in routine clinical practice. To improve the validation of strong-coupling metabolites as biomarkers of GBM and treatment-induced injury, work was performed to translate the CPMG into a 3-D MRSI-compatible sequence at 3 Tesla. The following outlines some of the design considerations that were involved in undertaking this project and also presents findings of interest.

Among the many available MRSI sequences, Point RESolved Spectroscopy (PRESS) is perhaps the most utilized and commonly cited in the literature, based on the relative ease of implimentation. It consists of three consecutive RF pulses whose relative timing and phase offsets resemble that of

the CPMG: 90_x—τ—180_y—2τ—180_y—τ—acq. Because of previously mentioned SAR contraints on pulse power, τ here is on the order of ms rather than μs and the number of refocusing pulses has been substantially reduced to accommodate patient tolerances. PRESS can also be distinguished from *ex vivo* precursors on account of its spatial localization via magnetic gradients, allowing for multi-voxel acquisitions that sample ~1 cm^3 regions of the brain. These gradients are magnetic fields that vary 2-4 G/cm in three orthogonal directions so as to generate different spin frequencies that can be related to location by means of Fourier transformation during post-processing. In PRESS, every RF pulse has an associated gradient that is simultaneously played out, such that successive selection of orthogonal slabs localizes a volume. Localization of a single plane during excitation along z would take the form:

$$\Delta z = \frac{BW}{\left(\frac{\gamma}{2\pi}\right) G_z} \qquad \text{(Eq. 3.28)}$$

where Δz is the slice thickness along z [cm], BW is the pulse bandwidth [Hz], and G_z is the gradient strength along z [G/cm]. To minimize the acquisition time for a multi-voxel 3-D sequence, one can first localize an overall volume of interest as shown above, and then localize individual voxels with a flyback readout gradient (46).

Although the conventional PRESS sequence is amenable to relatively short echo times (TE~29ms), there are several drawbacks that deal with limitations in RF pulse design. Because standard sinc refocusing pulses have effective bandwidths near 1100 Hz, there are chemical shift misregistration errors of the selected volume that occur at 3 Tesla relating to the distinct Larmor frequency of each resonance. This is often addressed through excitation of a larger volume by so-called overpress factors and saturating the undesired signal along the periphery (47), however the trade-off for whole-brain spectroscopy is potentially worse lipid contamination. Another limitation is that

PRESS refocusing pulses are designed to produce nutation angles less than 180-degrees due to SAR concerns, causing premature signal dephasing. These issues present a more obvious problem when considering the detection of strongly coupled metabolites that have lower SNR and are obscured by broad macromolecular (MM) signals at short TEs.

Given the difficulty associated with detecting such metabolites, the Carr-Purcell PRESS (CPRESS) sequence was specifically designed to minimize the effects of complex interactions on MR signal fidelity (36). When first proposed by Jurgen Hennig *et al*. to more accurately measure *in vivo* T_2 values, this CPMG-inspired sequence had as its key feature the multiplicity of refocusing pulses, which preserved the coupled resonances over a longer duration of time, while allowing MM signals to decay. Later iterations of CPRESS focused on SAR compliance for clinically-oriented acquisitions, with one study demonstrating the robust quantification that could be obtained using four true 180-degree refocusing pulses with non-linear phase (48). Because CPRESS sequence design has revolved around single-voxel applications, my particular interest has been in adapting the framework for 3-D whole-brain spectroscopy (MRSI). To that end, I am currently working on the most difficult portion of this engineering problem that concerns the proper implementation of RF pulses.

Using techniques (49) based on the Shinar-Le Roux (SLR) algorithm (50) for designing RF pulses, I pursued the development of a variety of non-linear pulses that satisfied specific requirements for the 3-D CPRESS sequence. Since quadratic phase refocusing pulses appeared to offer the best prospects in terms of short duration/high bandwidth under low power, they became the ad hoc construct with which to optimize design performance. Other techniques that modulated the pulse

and gradient in tandem to achieve further time/SAR reduction were avoided over concerns related to unnecessary technical complexity and limited extensibility. Convex optimization was used to minimize the transition widths during design and passband ripple was kept relatively small (0.005) to achieve robust spin echo profiles from simulation. Each of the quadratic phase pulses was implemented in a GE-based pulse sequence definition (PSD) that had been modified for 3-D whole-brain MRSI by incorporating existing atlas-based prescription code and a flyback echo-planar readout. The 3-D CPRESS sequence featuring 4 refocusing pulses was evaluated on a 3 Tesla GE scanner utilizing both an 8- and 32-channel headcoil, along with a standardized phantom containing common brain metabolites.
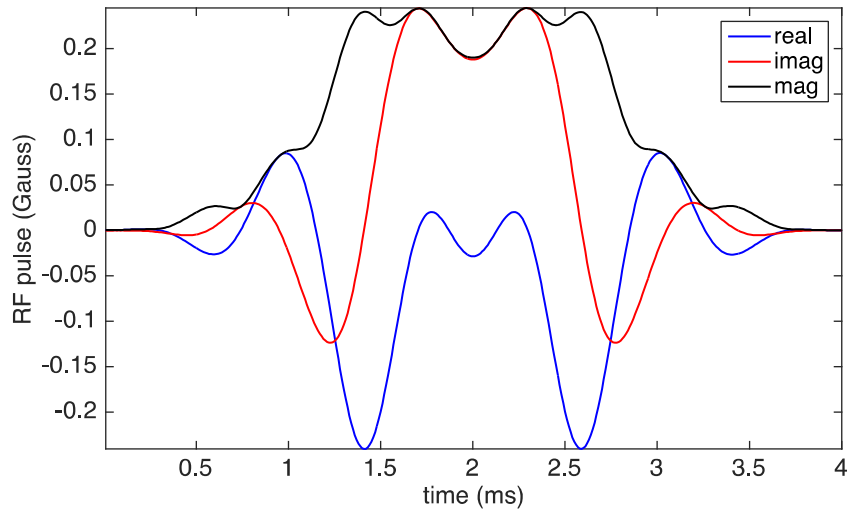
Figure 3.14. Quadratic phase RF pulse. Magnitude of SLR-based pulse along with real and imaginary components; phase not shown. Duration=4ms, BW=2500 Hz, TBW=10, max B_1~0.24G

As a critical design parameter, the coefficient of adiabadicity (k), which dictates the robustness of the pulse under field inhomogeneities, was the initial focus of testing. Values of k ranging from 70-200 representing practical design limits were assessed on the scanner according to power requirements and the associated bandwidths/pulse durations after any scaling due to headcoil

limitations. Of interest was that the k=115 pulse offered the highest bandwidths/shortest pulse durations for the power demand tolerated by the 32-channel heacoil prior to scaling at the B_1 max threshold (~0.23G). The k115 pulse was ultimately designed with a pulse duration/bandwidth=4 ms/2500 Hz, giving a time-bandwidth product (TBW) of 10, indicative of selectivity with moderate sharpness. Figure 3.14 shows the magnitude of the pulse waveform with its characteristically flat apex that is conducive to lower peak B_1. On the scanner, slight scaling yielded a pulse duration/bandwidth=4.2ms/2358Hz, which was a significant improvement over the 6.5ms/1100 Hz of the former 167-degree sinc pulses. The shorter pulse duration allowed for the inclusion of 4 refocusing pulses and a minimum TE=42ms.
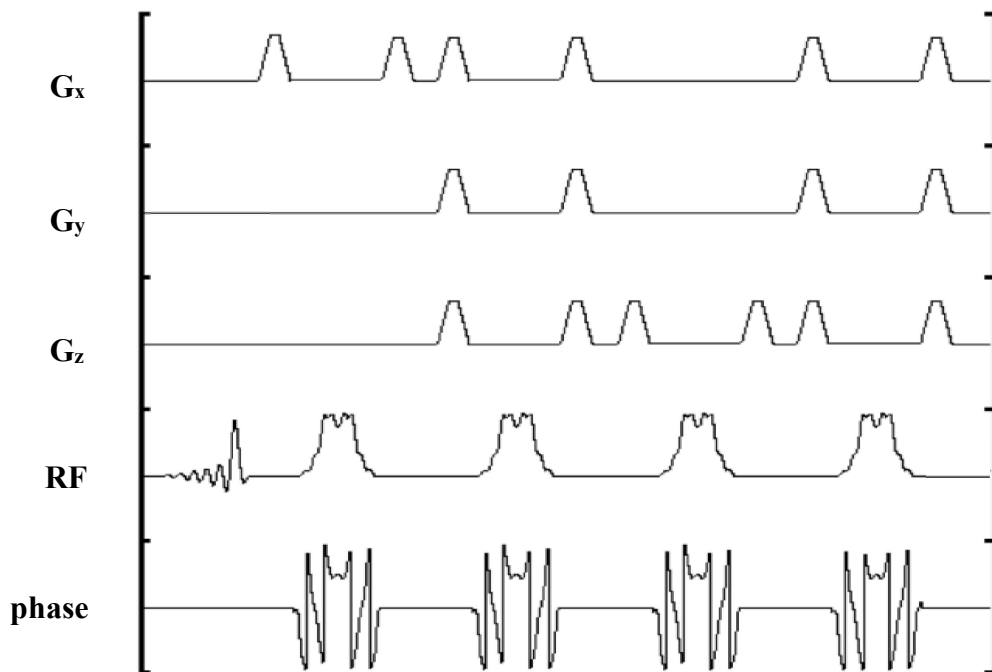
Figure 3.15. 3-D CPRESS sequence diagram. Crusher and localization gradients are shown for each orthogonal gradient direction: G_x, G_y, and G_z. The RF axis displays a minimum phase 90-degree excitation pulse followed by 4 refocusing pulses with associated quadratic phase

From the sequence diagram depicting the signature portion of CPRESS in Figure 3.15, it is clear

that the pulse waveforms differ substantially from those of conventional PRESS. In order to minimize the delay after excitation, an asymmetric 90-degree pulse (GE Healthcare, Germany) with minimum phase (bandwidth/duration=2300 Hz/3.1 ms) was incorporated, as shown on the RF axis. This is followed by the four quadratic phase pulses that are played out in pairs along the same gradient direction to mutually cancel phase nonlinearity. Comparing the simulated amplitude of these pulses to the asymmetric excitation pulse is demonstrative of their low peak B_1 characteristics. Existing crusher gradients having narrow widths and minimal area were employed to dephase unwanted coherences outside the volume of interest.

chemical shift (ppm)
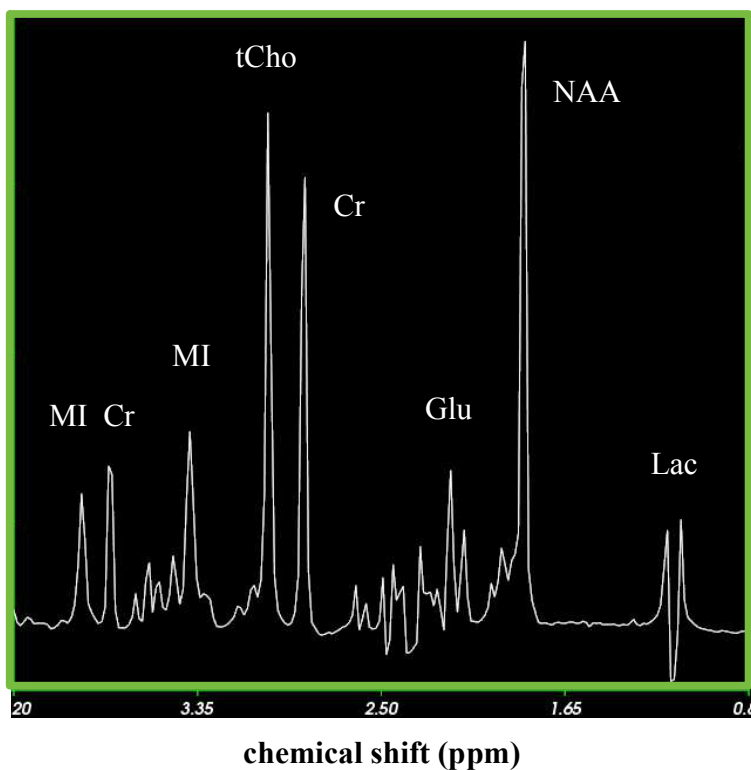
Figure 3.16. Phantom CPRESS spectra. Single-voxel (27 cm^3) acquisition of CPRESS in phantom containing common brain metabolites (TE=42ms, TR=2s, NEX=2, 128 scans)

Preliminary data from the CPRESS sequence appear promising, though development is still onging. In Figure 3.16, single voxel spectra from a phantom containing common brain metabolites demonstrate what can be achieved in terms of quality with the current features. The relative prominence of myo-inositol (MI), a strongly coupled metabolite, at TE=42ms supports the performance of refocusing pulses. Figure 3.17 displays data from a volunteer acquired with the 3-D CPRESS acquisition at TE=42ms and TE=50ms, which shows overall feasibility and preservation of MI signal over time.
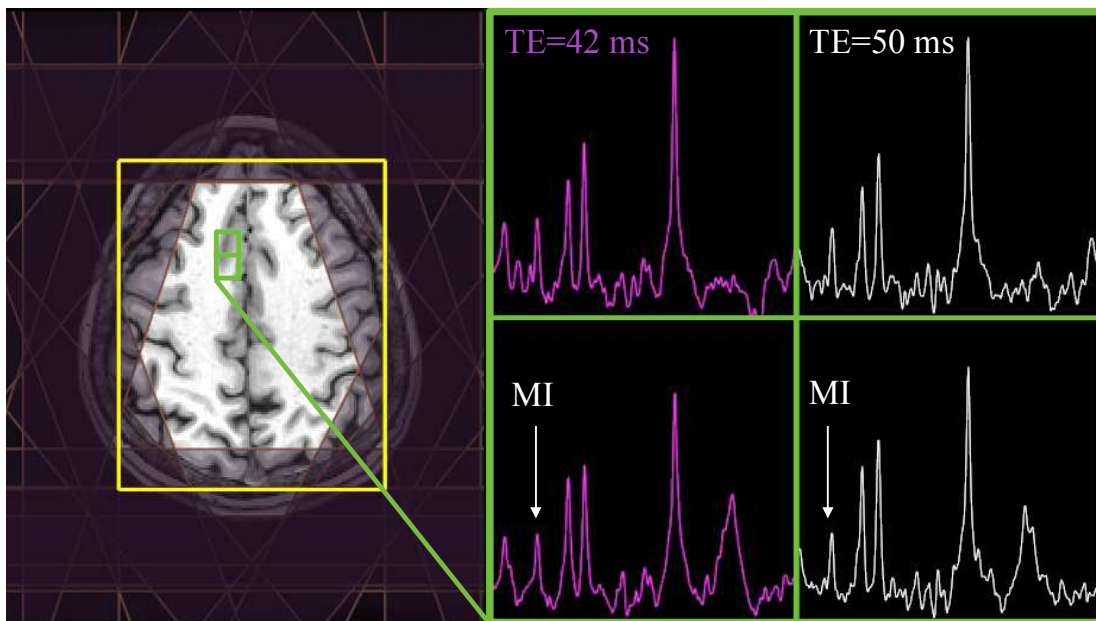
Figure 3.17. 3-D CPRESS acquisition. Voluteer data from 3-D CPRESS acquisition with automatic prescription and flyback echo-planar readout. The yellow box demarks the border of the selected region of interest ($11 \times 14 \times 60$ cm^3); dark bands on the periphery indicate very selective saturation (VSS) for lipid supression. Spectra from two 1cm^3 voxels are displayed for TE=42 and TE=50 ms to demonstrate preservation of myo-inositol (MI) signal. TR=1500ms, ~6 min. scan time.

3.11 References

1. Bloch F. The principle of nuclear induction. Nobel Lecture 1952, pp. 203-215

2. Purcell EM. Research in nuclear magnetism. Nobel Lecture 1952, pp. 219-231

3. Halogen F, Martin AD. Quarks and leptons: An introductory course in modern particle physics. John Wiley & Sons, Inc, c1984

4. Levitt, MH. Spin dynamics: basics of nuclear magnetic resonance. John Wiley & Sons, Ltd., c2001

5. Nishimura, DG. Principles of magnetic resonance imaging. Copyright 2010 by Dwight G. Nishimura

6. Slighter CP. Principles of magnetic resonance with examples from solid state physics. Harper & Row, c1963

7. Standford Encyclopedia of Philosophy. Experiment in Physics. Appendix 5: The Stern-Gerlach Experiment, c2005

8. Brown K. University of Saskatchewan. Angular Momentum and Bloch Equations, c2014

9. Pauli W jr., Zur Quantenmechanik des magnetischen Elektrons, Zeitschrift f. Physik. vol. 43, 1927

10. Landau LD, Lifshitz EM. Quantum mechanics: non-relativistic theory. Vol. 2 (3rd ed.) Pergamon Press, c1977

11. Wimmel H. Quantum physics and observed reality: a critical interpretation of quantum mechanics. World Scientific, c1992

12. French AP, Taylor EF. An introduction to quantum physics. Van Nostrand Reinhold, London, c1978

13. James TL, Nuclear magnetic resonance in biochemistry. Academic Press, New York, c1975.

14. Griffiths, DJ. Introduction to electrodynamics (3rd Ed.). Prentice Hall, c1999.

15. Bloembergen N, Purcell EM, Pound RV. Relaxation effects in nuclear magnetic resonance absorption. Physical Review 7(73), 1948: 679-746

16. Li C, Pielak GJ. Using NMR to distinguish viscosity effects from non-specific protein binding under crowded conditions. *J Am Chem Soc*. 131(4), 2009: 1368-1369

17. Bernstein MA, King FK, Zhou XJ. Handbook of MRI pulse sequences. Elsevier Academic Press, c2004

18. Bloch F. Nuclear Induction. Physical Review 70, 1946: 460-473

19. Haacke EM, Brown RW, Thompson MR, Venkatesan R. Magnetic resonance imaging: physical principles and sequence design. John Wiley & Sons, Inc, c1999

20. Gaskill J. Linear Systems, Fourier Transforms and Optics. Wiley-Interscience, c1978

21. Cooley JW, Tukey JW. An algorithm for the machine calculation of complex Fourier series. Math Comput. 19, 1965: 297-301

22. Kauppinen J, Partanen J. Fourier Transforms in Spectroscopy. Wiley-VCH, Verlag Berlin GmbH, c2001

23. Chmurny GN, Hoult DI. The Ancient and Honourable Art of Shimming. Concepts in Magnetic Resonance 2(3), 1990:131-149

24. Pohl L, Eckle M. Sodium 3-(trimethylsilyl)tetradeuteriopropionate, a new water-soluble standard for ^{1}H NMR. Angewandte Chemie International Edition in English. 8 (5), 1969: 381

25. Lange T. Detection of J-coupled metabolites in magnetic resonance spectroscopy (diss. ETH No. 17140), 2007

26. Slichter PC. Principles of magnetic resonance, 3rd Ed., Springer, Berlin, 1982

27. Bain AD, Fletcher DA, Hazendonk P. What is a transition? Concepts in Magnetic Resonance 10(1), 1998: 85-98

28. T. Fäcke and S. Berger. SERF, a new method to measure H,H coupling constants in organic chemistry J. Magn. Reson., Ser. A. 113, 1995: 114–116

29. Elkhaled A, Jalbert LE, Phillips J, Yosihara HAI, Parvataneni R, Srinivasan R, Bourne G, Berger MS, Chang SM, Cha S, Nelson SJ. Sci. Transl. Med. 4(116), 2012: 116ra5

30. Kelley DAC, Wald LL, Star-Lack JM. Lactate detection at 3T: compensating J coupling effects with BASING. JMRI 9, 1999: 732-737

31. Hahn EL. Spin Echoes. Phys. Rev. 80, 1950: 580-594

32. Hennig J. Echoes –How to generate, recognize, use or avoid them in MR-imaging sequences. Concepts in Magnetic Resoance 3, 1991: 125-143

33. Carr HY, Purcell EM. Effects of Diffusion on Free Precession in Nuclear Magnetic Resonance Experiments. Physical Review 94, 1954: 630–638

34. Meiboom S, Gill D. Modified spin-echo method for measuring nuclear relaxation times. Rev. Sci. Instrum. 29, 1958: 688-691

35. Allerhand A. Analysis of Carr-Purcell spin-spin NMR experiments on multiple-spin systems. I. The effect of homonuclear coupling. J Chem Phys. 44(1), 1966

36. Hennig J, Thiel Thorsten, Speck Oliver. Improved sensitivity to overlapping multiplet signals in in vivo proton spectroscopy using multiecho volume selective (CPRESS) experiment. MRM 37(6), 1997: 816-820

37. Homann H, Bornert P, Eggers H, Nehrke K, Dossel O, Graesslin I. Toward individualized SAR models and in vivo validation. MRM 66(6), 2011: 1767-1776

38. Mandal S, Borneman TW, Koroleva VDM, Hurlimann MD. Direct optimization of signal-to-noise ratio of CPMG-like sequences in inhomogeneous fields. J. Magn. Reson. 247, 2014: 54-66

39. Borneman TW, Hurlimann MD, Cory DG. Application of optimal control to CPMG refocusing pulse design. J. Magn. Reson. 207, 2010: 220-233

40. Criger B, Passante G, Park D, LaFlamme R. Recent advances in nuclear magnetic resonance

quantum information processing. Phil. Trans. R. Soc. A 370, 2012: 4620-4635

41. Grebenkov DS. Multiexponential attenuation of the CPMG spin echoes due to a geometrical confinement. J. Mag. Reson. 180, 2006: 118-126

42. Jen J. Chemical exchange and NMR T2 relaxation—The multisite case. J. Mag. Reson. 30(1), 1969: 111-128

43. Maricq MM, Waugh JS. NMR in rotating solids. J. Chem. Phys. 70(7), 1979: 3300 – 3316

44. Alam TM, Jenkins JE,. HR-MAS NMR spectroscopy in material science, Advanced aspects of spectroscopy, Farrukh MA (Ed.), InTech, 2012

45. Olejniczak ET, Vega S, Griffin RG. Multiple pulse NMR in rotating solids. J. Chem. Phys. 81, 1984: 4804-4817

46. Cunningham CH, Vigneron DB, Chen AP, Xu Duan, Nelson SJ, Hurd RE, Kelley DA, Pauly JM. Design of flyback echo-planar readout gradients for magnetic resonance spectroscopic imaging. MRM 54, 2005: 1286-1289

47. Scheenen TWJ, Klomp DWJ, Wijnen JP, Heerschap A. Short echo time H-MRSI of the human brain at 3T with minimal chemical shift displacement errors using adiabatic refocusing pulses. MRM 59, 2008: 1-6

48. Hancu I. Which pulse sequence is optimal for myo-inositol detection at 3T? NMR Biomed 22(4), 2009: 426-435

49. Shang H, Larson PEZ, Kerr A, Reed G, Sukimar S, Elkhaled A, Gordon J, Ohliger MA, Pauly

JM, Lustig M. Multiband RF pulses with improved performance via convex optimization. Journal of Magnetic Resonance 262, 2016: 81-90

50. Pauly J. Parameter relations for the Shinar-Le Roux selective excitation pulse design algorithm. IEEE Transactions on Medical Imaging 10(1), 1991:53-65

Chapter 4: Characterization of metabolites in infiltrating gliomas using *ex vivo* H-1 high-resolution magic angle spinning spectroscopy

Original research is presented in this chapter on the spectroscopic analysis of tissue samples acquired from patients with pathologically distinct subtypes of infiltrating glioma. Using small specimens that had been obtained through image- and MRS-guided techniques, we performed *ex vivo* HR-MAS spectroscopy to evaluate the neurochemical content with high spectral resolution. Given the interest of developing non-invasive imaging markers of tumor pathology, the goal of the study was to determine whether glioma subtypes could be characterized on the basis of their metabolomic profiles. After quantifying the data, metabolite levels were compared among WHO grade II-IV glioma and among glioma that had undergone inter-grade transitions as a result of malignant progression. Machine learning models were also employed to assess the potential for differential classification of these subtypes according to the data.

Authors:

Adam Elkhaled, Llewellyn Jalbert, Alexandra Constantin, Hikari A. I. Yoshihara, Joanna J. Phillips, Annette M. Molinaro, Susan M. Chang and Sarah J. Nelson

Abstract

Gliomas are routinely graded according to histopathological criteria established by the World

Health Organization. Although this classification can be used to understand some of the variance in the clinical outcome of patients, there is still substantial heterogeneity within and between lesions of the same grade. This study evaluated image-guided tissue samples acquired from a large cohort of patients presenting with either new or recurrent gliomas of grades II–IV using ex vivo proton high-resolution magic angle spinning spectroscopy. The quantification of metabolite levels revealed several discrete profiles associated with primary glioma subtypes, as well as secondary subtypes that had undergone transformation to a higher grade at the time of recurrence. Statistical modeling further demonstrated that these metabolomic profiles could be differentially classified with respect to pathological grading and inter-grade conversions. Importantly, the myo-inositol to total choline index allowed for a separation of recurrent low-grade gliomas on different pathological trajectories, the heightened ratio of phosphocholine to glycerophosphocholine uniformly characterized several forms of glioblastoma multiforme, and the onco-metabolite D-2-hydroxyglutarate was shown to help distinguish secondary from primary grade IV glioma, as well as grade II and III from grade IV glioma. These data provide evidence that metabolite levels are of interest in the assessment of both intra-grade and intra-lesional malignancy. Such information could be used to enhance the diagnostic specificity of in vivo spectroscopy and to aid in the selection of the most appropriate therapy for individual patients.

Introduction

Gliomas are tumors of the central nervous system that are routinely graded on a scale of I to IV according to histopathological criteria developed by the World Health Organization (WHO) (1,2). Whereas grade I gliomas are considered to be benign and can typically be treated through surgical

intervention, infiltrating gliomas of grades II–IV present a number of challenges in making an accurate diagnosis and in selecting the most appropriate therapy. Some of the complications associated with the management of infiltrating gliomas stem from the fact that individual lesions are spatially heterogeneous and small tissue samples obtained during biopsy or surgery may not represent the most malignant region of the tumor. This situation is accentuated following treatment, where a differential response to therapy and tumor progression can cause additional ambiguity. Because clinical outcomes for glioma can be quite variable, it is important to provide criteria to more accurately assess the characteristics that change both within and between pathological grades. A further complication is that grade II and III gliomas often undergo malignant transformation at the time of recurrence, which may necessitate more aggressive therapy (3–6). This raises the question of whether individual gliomas develop de novo (primary glioma) at a given grade or arise as a result of transformation from a less malignant lesion (secondary glioma) that was not detected previously. As lesions of the same histological grade may arise by different mechanisms, the designation of primary and secondary glioma may have important clinical consequences for the optimization of treatment (7).

Recent findings have indicated that the metabolite characteristics of the lesion are valuable for the investigation of underlying differences in malignancy. In vivo metabolite imaging provides a unique opportunity for the evaluation of spatial and temporal changes in the lesion and surrounding tissue that can be used to direct tissue sampling at the time of resection, as well as for the selection and monitoring of therapy. The lesion-wide data obtained using this approach are synergistic with recent results from genome-wide sequencing and informatics-driven analyses that identify different subtypes of glioma with genetic characteristics. The ability to infer the mutational status

of isocitrate dehydrogenase (IDH) genes through non-invasive MRSI of D-2-hydroxyglutarate (2HG) is an example with strong prognostic implications. This is a significant breakthrough in the realm of cancer diagnostics (8,9), because it indicates that the evaluation of new therapies that target the IDH pathway could be achieved non-invasively (10–13).

The primary goal of this study was to use the NMR technique of proton high-resolution magic angle spinning (^{1}H HR-MAS) spectroscopy to characterize the ex vivo metabolite profiles of pathologically distinct glioma subtypes at the time of initial diagnosis and at subsequent transformation. By collecting a large cohort of image-guided tissue samples, we sought to evaluate the hypothesis that different glioma subtypes have characteristic metabolite profiles that can aid in the prediction of the malignant potential. The information obtained may be used directly for improved categorization of ex vivo tissue samples, or can be translated into an in vivo setting to provide non-invasive metabolite imaging methods to direct tissue sampling, to monitor therapy and to make informed decisions about the effectiveness of different treatment strategies.

Materials and Methods

Patient Population

Our institutionally approved study comprised 126 patients receiving surgical resection as a result of suspected new or recurrent WHO grade II, III or IV glioma, who provided informed consent for image-guided tissue samples to be taken from areas designated for resection on the basis of clinical criteria. The diagnosis of grade was subsequently confirmed by a single pathologist on the basis of standard histological criteria (Table 4.1).

Table 4.1. Patient population. Patients and tissue samples were stratified according to original WHO grade and recurrence status

Table 1. Patient population. Patients and tissue samples were stratified according to original World Health Organization (WHO) grade and recurrence status			
Original WHO grade	Total	Newly diagnosed	Recurrent
	Number of patients (tissue samples)	Number of patients (tissue samples)	Number of patients (tissue samples)
II	54 (114)	0 (0)	54 (114)
III	22 (39)	5 (7)	17 (32)
IV	50 (101)	35 (70)	15 (31)
Total	126 (254)	40 (77)	86 (177)

Pre-operative MRI and MRS

Pre-operative MR examinations were conducted using either 1.5- or 3-T whole-body MR scanners (GE Healthcare Technologies, Milwaukee, Wisconsin, USA) with an eight-channel, phased-array head coil for signal reception (MRI Devices, Knaresborough, United Kingdom). The data obtained included three-dimensional T_1-weighted and T_2-weighted anatomic images, six-directional diffusion-weighted imaging acquired in the axial plane (TR/TE = 1000/108 ms; voxel size, 1.7 × 1.7 × 3 mm^3; b = 1000 s/mm^2) and, in some cases, lactate (Lac)-edited three-dimensional ^{1}H MRSI. The latter applied point-resolved spectroscopic selection (PRESS) for volume localization and very selective saturation (VSS) pulses for lipid (Lip) signal suppression (excited volume, ~80 × 80 × 40 mm^3; overpress factor, 1.5; TR/TE = 1104/144 ms; field of view, 16 × 16 × 16 cm^3; nominal voxel size, 1 × 1 × 1 cm^3; flyback echo-planar readout gradient in the superior-inferior direction; 712 dwell points; sweep width, 988 Hz) (14). Assessment of breakdown of the blood–brain barrier was made by administering a standard dose of Gd-DTPA (gadopentetate

dimeglumine; Magnevist) prior to the acquisition of T_1-weighted inversion recovery spoiled-gradient echo (IRSPGR) images (TR/TE = 8.9/2.5 ms).

Post-processing of pre-operative MR examination

In vivo data from the pre-operative examination were transferred to a Sun Ultra 10 workstation (Sun Microsystems, Santa Clara, California, USA) and in-house software was applied to derive estimates of diffusion and spectroscopic parameters. Maps of the apparent diffusion coefficient (ADC) were generated on a pixel-by-pixel basis (15). The ^{1}H MRSI data were processed in order to quantify total choline (tCho) and N-acetylaspartate (NAA) levels, from which maps of the choline to NAA index (CNI) could be derived. The CNI values were generated from an iterative linear regression-based algorithm that sequentially removes outlying values (16), and represent changes in choline and NAA levels relative to the normal voxels from the same subject.

Image-guided tissue sampling

The acquisition of pre-surgical in vivo MR data enabled the locations for tissue sampling from individual lesions to be planned prior to resection. Targets were selected from within the anatomical lesion (gadolinium-enhancing region and/or area of hyperintensity on T_2-weighted images) that demonstrated an ADC value of less than 1.5 times the value in normal-appearing white matter and/or had elevated CNI values (CNI > 3.0) from ^{1}H MRSI. Figure 4.1 depicts the selection of targets for a patient with a grade IV glioma. The CNI map highlights the relative elevation of choline species and reduction in NAA, which are consistent with malignant tissue. Two primary targets were defined, with one showing a local CNI maximum and the other corresponding to a region of hypointensity on the ADC map. Targets were designated from each patient as spherical

regions of interest with a diameter of 5 mm on co-registered MR images using BrainLAB surgical navigation software (BrainLAB Inc., Munich, Germany). Image-guided navigation was applied to locate tissue corresponding to predefined targets, and the neurosurgeon provided samples from as close as possible to the target. The actual sample location was saved on the BrainLAB workstation, and the corresponding coordinates were transferred offline for subsequent reference. After excision, the tissue samples were immediately bisected: half was snap frozen in liquid nitrogen less than 1 min after removal and stored at −80 °C for ^{1}H HR-MAS spectroscopy; the other half was fixed in 10% zinc formalin, dehydrated by graded ethanols and embedded in Paraplast Plus wax (McCormick Scientific, St. Louis, Missouri, USA) using standardized techniques for pathological analysis.

Histological analysis of the tumor

A pathologist evaluated the slides prepared from tissue samples with hematoxylin and eosin stains to determine the relative contribution of tumor cells to the overall cellularity. A score of '0' denoted neuropil without tumor, '1' indicated an infiltrating tumor margin containing detectable but not abundant numbers of tumor cells, '2' denoted a more cellular infiltrated zone, and '3' denoted highly cellular tumor with relatively few non-neoplastic cells. Tissue samples containing tumor cells (scores > 0) were classified according to WHO standards.
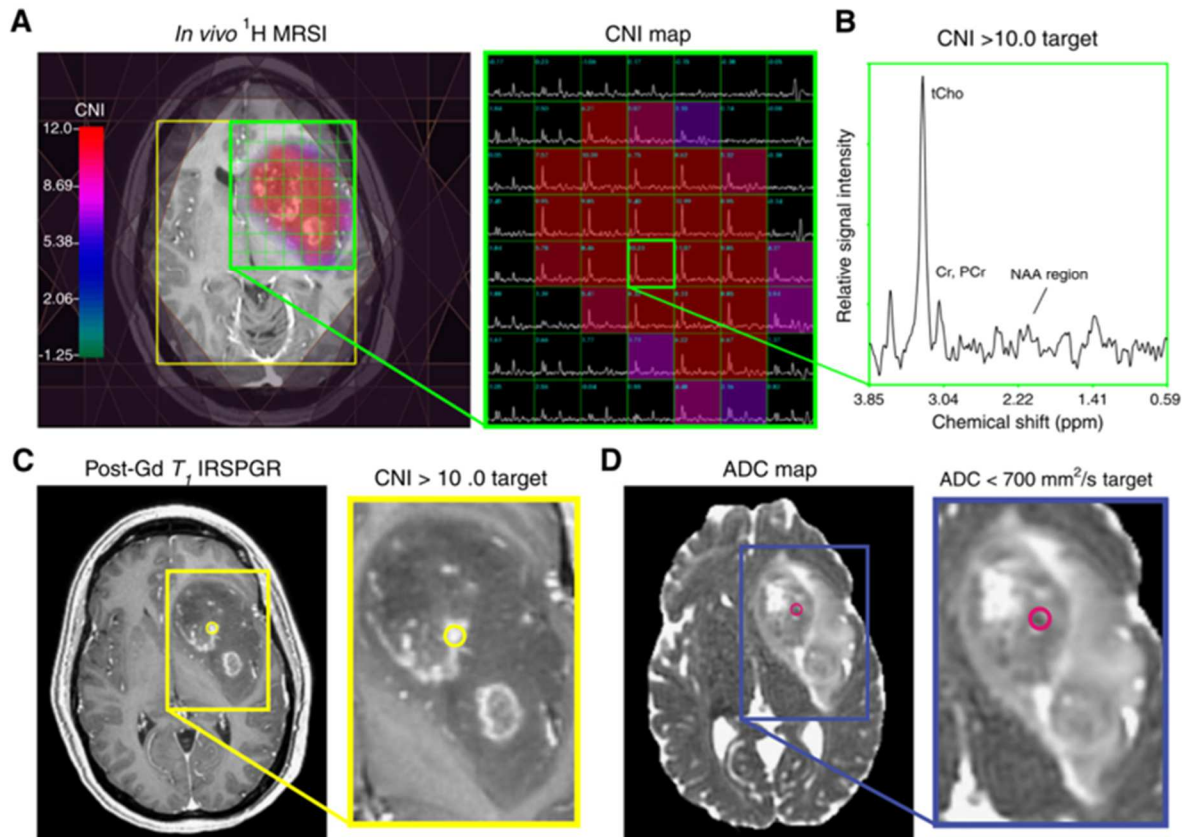
Figure 4.1. Planning of image- and MRSI-guided tissue sampling. In vivo 1H MRS of a patient diagnosed with glioblastoma multiforme. Point-resolved spectroscopic selection (PRESS) coverage defined by yellow box; outer volume suppression (OVS) of lipid shown on periphery; map of the choline to N-acetylaspartate (NAA) index (CNI) is overlaid on a T_1-weighted inversion recovery spoiled-gradient echo (IRSPGR) post-Gd image. The corresponding subsets of spectra covering the lesion are shown on the right with CNI values; voxel highlighted in green is designated as a putative tumor region on the basis of elevated CNI within the contrast-enhancing lesion (A). The spectrum from the voxel highlighted in green is enhanced to show the relative metabolite levels contributing to the CNI (B). A 5-mm-diameter target planned for surgical navigation based on this elevated CNI is shown on the T_1-weighted post- contrast image (C). An adjacent target based on restricted diffusion is shown on an apparent diffusion coefficient (ADC) map as a regional hypointensity (D). Cr, creatine; GPC, glycerophosphocholine; PC, phosphocholine; PCr, phosphocreatine; tCho, total choline ([Cho] + [PC] + [GPC]).

^{1}H HR-MAS spectroscopy

Tissue samples weighing between 0.87 and 37.86 mg (median, 9.77 mg) were evaluated. A 35-μL

zirconia rotor (custom-designed by Varian, Palo Alto, California, USA) was used with 3 µL of 99.9% atom-D deuterium oxide containing 0.75 wt% 3-(trimethylsilyl)propionic acid (Sigma-Aldrich, St. Louis, Missouri, USA) for chemical shift referencing. Data were acquired at 11.7 T at 1 °C with a spin rate of 2250 Hz in a 4-mm gHX nanoprobe with a Varian INOVA 500- MHz multi-nuclear spectrometer. The nanoprobe gHX is an inverse probe, optimized for the direct detection of ^{1}H and the indirect detection of X-nuclei (^{13}C,^{31}P,^{15}N), and equipped with a magic angle gradient coil.

A rotor-synchronized, one-dimensional, Carr–Purcell–Meiboom– Gill (CPMG) pulse sequence was run with TR/TE = 4 s/144 ms, 512 scans, 40 000 acquired points, 90° pulse and spectral width of 20 kHz for a total time of 35 min. A relatively long TE was used to maximally suppress the macromolecular background for purposes of metabolite fitting. The electronic reference to access in vivo concentrations (ERETIC) method was used to generate an artificial electronic signal that served as an external standard for the estimation of metabolite levels (17).

Pre-processing of the spectra was performed in the time domain using the Java-based Magnetic Resonance User Interface (jMRUI) (18). The estimation of relative one-dimensional metabolite levels was achieved with the semi-parametric algorithm, high-resolution quantum estimation (HR-QUEST), which fits a customized basis set of metabolites to the spectrum (19). The basis set used in this study comprised spectra from 26 metabolite solutions commonly studied in the human brain (Sigma-Aldrich): NAA, free choline (Cho), phosphocholine (PC), glycerophosphocholine (GPC), ethanolamine (Eth), phosphoethanolamine (PE), creatine/phosphocreatine (Cr/ PCr), myo-inositol (MI), scyllo-inositol (SI), glucose (Glc), glycine (Gly), total glutathione [tGSH: glutathione (GSH)

+ glutathione disulfide (GSSG)], glutamate (Glu), glutamine (Gln), 2HG, γ-aminobutyric acid (GABA), taurine (Tau), hypotaurine (hTau), threonine (Thr), acetate (Ace), Lac, alanine (Ala), betaine (Bet), aspartate (Asp), valine (Val) and succinate (Suc). It also included spectra for potential contaminants owing to the surgical sterilization agents methanol (MeOH) and ethanol (EtOH). Each spectrum was evaluated by an experienced spectroscopist to visually assess the goodness of fit, and to determine whether low spectral resolution or signal-to-noise ratio had compromised the evaluation of the metabolite levels. Tissue samples found to have ambiguous or unreliable results were eliminated from subsequent analyses.

Statistical analysis

Tissue samples with tumor scores of 1–3 and metabolite levels with Cramer–Rao error estimates of less than 11% were evaluated. To assess the association of the metabolite parameters with various pathological grades and inter-grade transitions, a proportional odds logistic regression model, adjusted for repeated measures, was applied to evaluate the probability of observing grade outcomes corresponding to different levels of malignancy. This model is written as:

$$logit\left[p\left(Y_{ij} \le K | X_i, Z_i\right)\right] = \alpha_K + X_{ij}'\beta + Z_{ij}'b_i \,; i = 1, \ldots, N_{subjects}\,; K = 1, \ldots, c-1$$

, where Y_{ij} is the ordinal outcome for subject i with biopsy measurement j (ranges from 1 to 4), c is the total number of levels of the ordinal variable, X_{ij} is the design matrix for the fixed effects, Z_{ij} is the design matrix for the random effects, α_K are rows corresponding to the jth biopsy specimen, and β and b_i are the vectors of fixed and random parameters. The intercepts are fixed and category dependent. The odds ratio and p value for each variable are reported. The ordinal-valued outcome mixed effect models were analyzed using PROC GENMOD in SAS (SAS Institute Inc., Cary, North Carolina, USA) v.9.2.

Statistical tests with *p* values of less than 0.05 were considered to be significant. Metabolites predictive of pathological grade when adjusted for repeated specimen sampling were deemed to be significant predictors and are presented in the results. Because of the exploratory nature of the study, no adjustment for type I error was included.

The second aspect of the analysis concerned the classification of glioma subtypes among relevant groups. Logistic ridge regression models with automatic feature selection were used to determine whether metabolite parameters derived from HR-MAS spectra could jointly predict pathological grades and inter-grade transitions. Classification accuracy was defined as: (number of true positives + number of true negatives)/(sample total). These accuracies were adjusted for multiple tissue samples per patient by repeatedly training the models (100 training sets per model) using only one randomly selected sample per patient, and testing them using the remaining samples. Two feature selection methods were applied. An information gain ratio filtering method was first employed to remove all variables that provided no gain in classification accuracy when evaluated individually, followed by a wrapper-based feature selection method for the evaluation of the worth of subsets of features and selection of the best parsimonious model that was encountered. Average receiver operating characteristic (ROC) curves were generated to visualize the classification performance of each model for the sampled cutoffs, and the average area under the curve (AUC) was calculated.

Results

Summary of analyzed tumor tissue

The numbers of tissue samples that were determined by pathological analysis to contain tumor are summarized according to their grade at initial diagnosis in Table 4.1. A total of 254 tumor samples acquired from 126 subjects were evaluated using ^{1}H HR-MAS spectroscopy.

Distinguishing metabolite profiles on the basis of primary glioma grade

To be included in the evaluation of profiles from primary grades, samples from recurrent lesions were required to have the same histological grade as that determined at initial diagnosis. As shown in Table 4.2, 43 of the samples were grade II, 25 grade III and 101 grade IV.

Table 4.2. Metabolite levels of primary glioma. Relative metabolite levels for each subtype of glioma, displayed as mean±SEM; no units are expressed owing to the T_2 dependence of the CPMG acquisition.

Table 2. Metabolite levels of primary glioma. Relative metabolite levels for each subtype of glioma, displayed as mean ± standard error of the mean (SEM); no units are expressed owing to the T_2 dependence of the Carr–Purcell–Meiboom–Gill (CPMG) acquisition

	Grade II (n = 43)	Grade III (n = 25)	Grade IV (n = 101)	Overall	Grade II versus III	Grade III versus IV	Grade II versus IV
	Mean levels ± SEM			Odds ratios (95% CI)			
	Number of fitted spectral samples			p values			
NAA	29 ± 6	24 ± 6	12 ± 2	0.946 (0.906–0.989)		0.927 (0.875–0.981)	0.929 (0.873–0.988)
	17	8	22	0.01	NS	0.009	0.02
Cho	38 ± 7	64 ± 9	30 ± 4			0.979 (0.959–0.999)	
	33	21	47	NS	NS	0.04	NS
PC	51 ± 7	83 ± 15	67 ± 8				
	33	20	29	NS	0.06	NS	NS
tCho	144 ± 19	183 ± 18	112 ± 8	0.996 (0.992–0.999)		0.986 (0.984–0.996)	
	39	23	53	0.02	NS	0.0007	0.08
PE	110 ± 14	203 ± 31	132 ± 12	1.010 (1.003–1.018)			
	29	17	47	NS	0.008	NS	NS
(P)Cr	187 ± 23	166 ± 20	95 ± 7	0.991 (0.986–0.995)		0.989 (0.983–0.995)	0.988 (0.981–0.994)
	37	23	50	<0.0001	NS	0.0001	0.0002
MI	382 ± 44	321 ± 40	176 ± 20	0.995 (0.992–0.999)			
	39	23	45	0.04	NS	NS	0.07
Gly	152 ± 23	269 ± 34	185 ± 20			0.997 (0.994–0.999)	
	25	20	45	NS	0.08	0.02	NS
tGSH	35 ± 4	57 ± 20	61 ± 6				1.032 (1.007–1.058)
	14	7	47	NS	0.09	NS	0.01
Glu	199 ± 21	278 ± 43	296 ± 28				
	32	22	57	NS	0.12	NS	0.09
Gln	127 ± 21	209 ± 35	149 ± 9				
	27	19	50	NS	0.14	0.06	NS
2HG	32 ± 4	34 ± 4	0*	0.907 (0.869–0.947)		0.832 (0.753–0.920)	0.827 (0.732–0.935)
	17	13	101	<0.0001	NS	0.0003	0.002
Thr	39 ± 9	82 ± 18	74 ± 12				1.019 (1.008–1.003)
	16	13	42	NS	0.07	NS	0.02
PC/GPC	111 ± 37	180 ± 81	229 ± 31				
	31	13	23	NS	NS	NS	NS
MCI	325 ± 27	192 ± 22	169 ± 14	0.993 (0.989–0.966)	0.992 (0.986–0.999)		0.992 (0.987–0.996)
	38	22	42	0.0002	0.02	NS	0.0005
tCho/(P)Cr	98 ± 13	124 ± 14	140 ± 16	1.007 (1.000–1.013)			
	37	21	76	0.04	NS	NS	0.08

2HG, ᴅ-2-hydroxyglutarate; Cho, free choline; Cr, creatine; Gln, glutamine; Glu, glutamate; Gly, glycine; GPC, glycerophosphocholine; GSH, glutathione; GSSG, glutathione disulfide; MCI, myo-inositol to total choline index; MI, myo-inositol; NAA, N-acetylaspartate; NS, not significant; PC, phosphocholine; PCr, phosphocreatine; PE, phosphoethanolamine; tCho, total choline ([Cho] + [PC] + [GPC]); tGSH, total glutathione ([GSH] + [GSSG]); Thr, threonine.
*Absence of 2HG resonances confirmed by visual inspection.

Results from the ex vivo ^{1}H HR-MAS spectra were represented in three different ways. Figure 4.2A–C shows spectra normalized with respect to the area of the ERETIC peak and then averaged to provide a single mean spectrum for each grade. These composite spectra allowed a visual assessment of differences in the relative patterns of the peaks. It should be noted that the relatively high peaks corresponding to Lac were not considered in the comparative analysis as evidence indicates that they cannot reliably reflect in vivo levels (20). Figure 4.2D shows deviations in mean metabolite levels for samples from primary grade III and IV gliomas relative to the levels in

primary grade II, with significant increases or decreases in metabolites being highlighted in red and green, respectively. Table 4.2 provides the mean and standard error of individual metabolite levels estimated using HR-QUEST and tested for significant differences between grades.
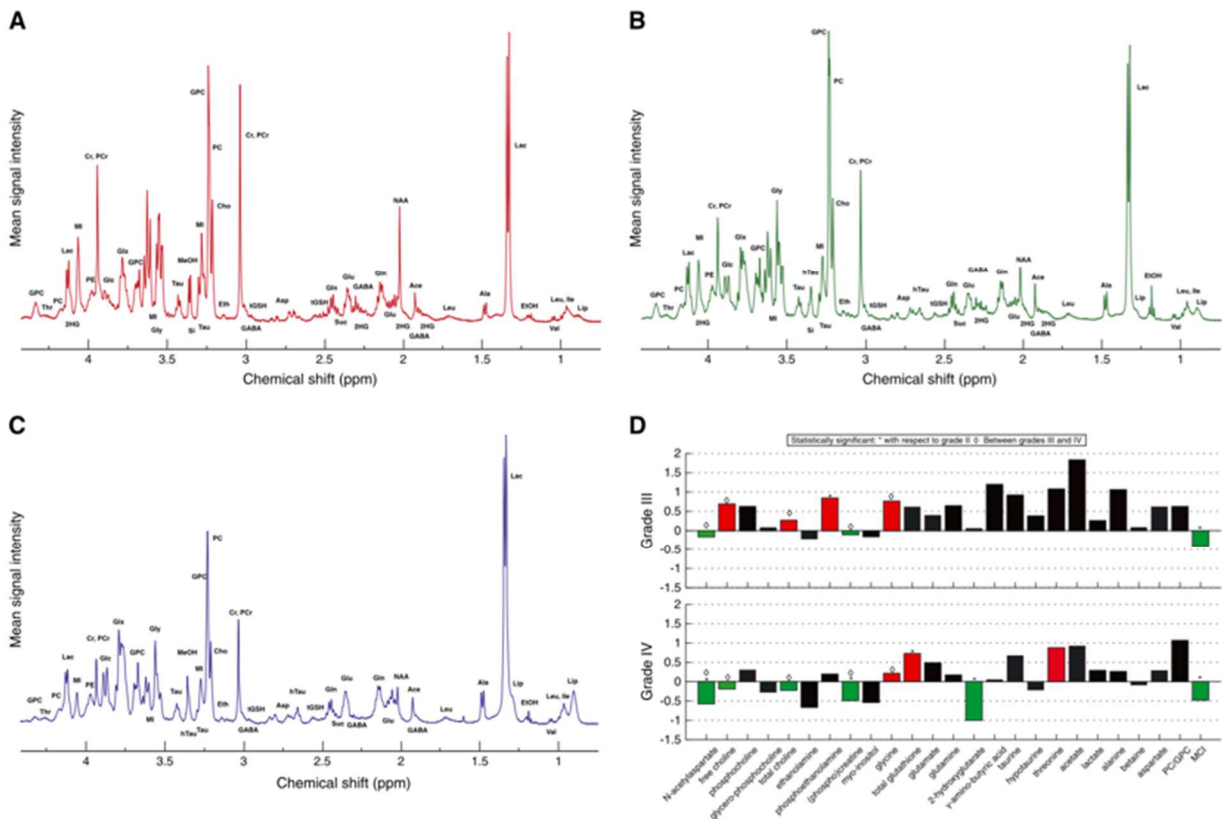
Figure 4.2. Metabolite profiles of primary glioma. Mean Carr–Purcell–Meiboom–Gill (CPMG) spectra for glioma samples histologically defined as grade II (n = 43) (A), grade III (n = 25) (B) and grade IV glioblastoma multiforme (GBM) (n = 114) (C). Deviation in quantified mean metabolite levels of grade II and IV glioma relative to grade II glioma; reported levels are unitless owing to the T_2 dependence of the CPMG acquisition (D). Significant increases or decreases in the metabolite levels displayed as residuals are highlighted in red and green, respectively. Significance was defined as p < 0.05 for the comparative analysis among subtypes using proportional odds logistic regression.

The mean spectrum for primary grade II gliomas (Fig. 4.2A) showed prominent peaks corresponding to Cr/PCr, MI, GPC, PC, Cho and NAA, with clear composite peaks corresponding

to 2HG, Glu and Gln. The tGSH resonances were relatively low. A key parameter that distinguished primary grade II lesions from the other primary grades (see Table 4.2) was the ratio of MI to tCho (MCI), which was higher than for both grade III ($p = 0.02$) and grade IV ($p = 0.0005$) lesions. Thr, which is a precursor to both Gly and acetyl-CoA, was either significantly lower or trending towards lower levels in primary grade II relative to primary grade III ($p = 0.07$) and grade IV ($p = 0.02$) lesions.

Table 4.3. Glioma classification models. Performance of the machine learning classification schemes, as well as average ROC curve areas.

Table 3. Glioma classification models. Performance of the machine learning classification schemes, as well as average receiver operating characteristic (ROC) curve areas

	Number of (patients, tissue samples) per grade or transformation	Classification model	Average classification accuracy ± SD (%)	Average ROC curve area
Primary glioma	II (21,43)	II *versus* III	73.1 ± 4.2	0.761
	III (15,25)	III *versus* IV	92.4 ± 2.8	0.960
	IV (50, 101)	II *versus* IV	84.4 ± 3.2	0.869
Recurrent low-grade		$G_{II \rightarrow II}$ *versus* $G_{II \rightarrow III}$	69.3 ± 4.4	0.746
glioma	$G_{II \rightarrow II}$ (21, 43)	$G_{II \rightarrow III}$ *versus* $G_{II \rightarrow IV}$	72.5 ± 3.1	0.550
	$G_{II \rightarrow III}$ (26, 52)	$G_{II \rightarrow II}$ *versus* $G_{II \rightarrow IV}$	73.6 ± 5.7	0.745
	$G_{II \rightarrow IV}$ (8, 19)	$G_{II \rightarrow II}$ *versus* TFD	69.9 ± 5.1	0.726
Primary *versus*	$G_{II \rightarrow III}$ (26, 52)	III *versus* $G_{II \rightarrow III}$	76.7 ± 5.6	0.676
secondary grade III	III (15, 25)			
Primary *versus*	IV (50, 101)	IV *versus* $G_{II \rightarrow IV}$	94.4 ± 0.8	0.854
secondary GBM	$G_{II \rightarrow IV}$ (8, 19)	IV *versus* $G_{III \rightarrow IV}$	95.6 ± 0.9	0.756
	$G_{III \rightarrow IV}$ (7, 14)	$G_{II \rightarrow IV}$ *versus* $G_{III \rightarrow IV}$	61.9 ± 4.1	0.698

GBM, glioblastoma multiforme; TFD, gliomas that have transformed to a higher grade of malignancy.

The mean spectrum from primary grade III glioma showed prominent peaks from GPC, PC and Cho, that were higher relative to Cr/PCr and NAA than for the mean spectrum from grade II glioma (Fig. 4.2B). There was also a more prominent Gly peak and relatively low peaks from MI. Resonances corresponding to 2HG, Glu and Gln were visible, as well as additional peaks from hTau. The statistical analysis showed that, although there was a general trend towards higher overall metabolite levels relative to primary grade II lesions (Fig. 4.2D), only the reduction in MCI

(p = 0.02) and the increase in PE (p = 0.008) reached significance (Table 4.2).

The mean spectrum from primary grade IV glioma (Fig. 4.2C) showed relatively lower GPC, Cr/PCr and NAA peaks than both of the lower grades, and lower MI and Gly peaks relative to primary grade III glioma. There were no 2HG resonances seen in individual primary grade IV samples, but relatively more PC relative to GPC, and the presence of Lip peaks at 0.9 and 1.25 ppm that were either lower or absent in grades II and III. Tests of significance showed that the levels of NAA and Cr/PCr were lower than in both grade II (p = 0.02 and 0.0002) and grade III (p = 0.009 and 0.0001) gliomas. In addition, MCI was significantly lower (p = 0.0005) and the level of tGSH higher (p = 0.01) than in primary grade II glioma, and the levels of Cho, tCho and Gly were significantly lower than in grade III glioma (p = 0.04, 0.0007 and 0.02).
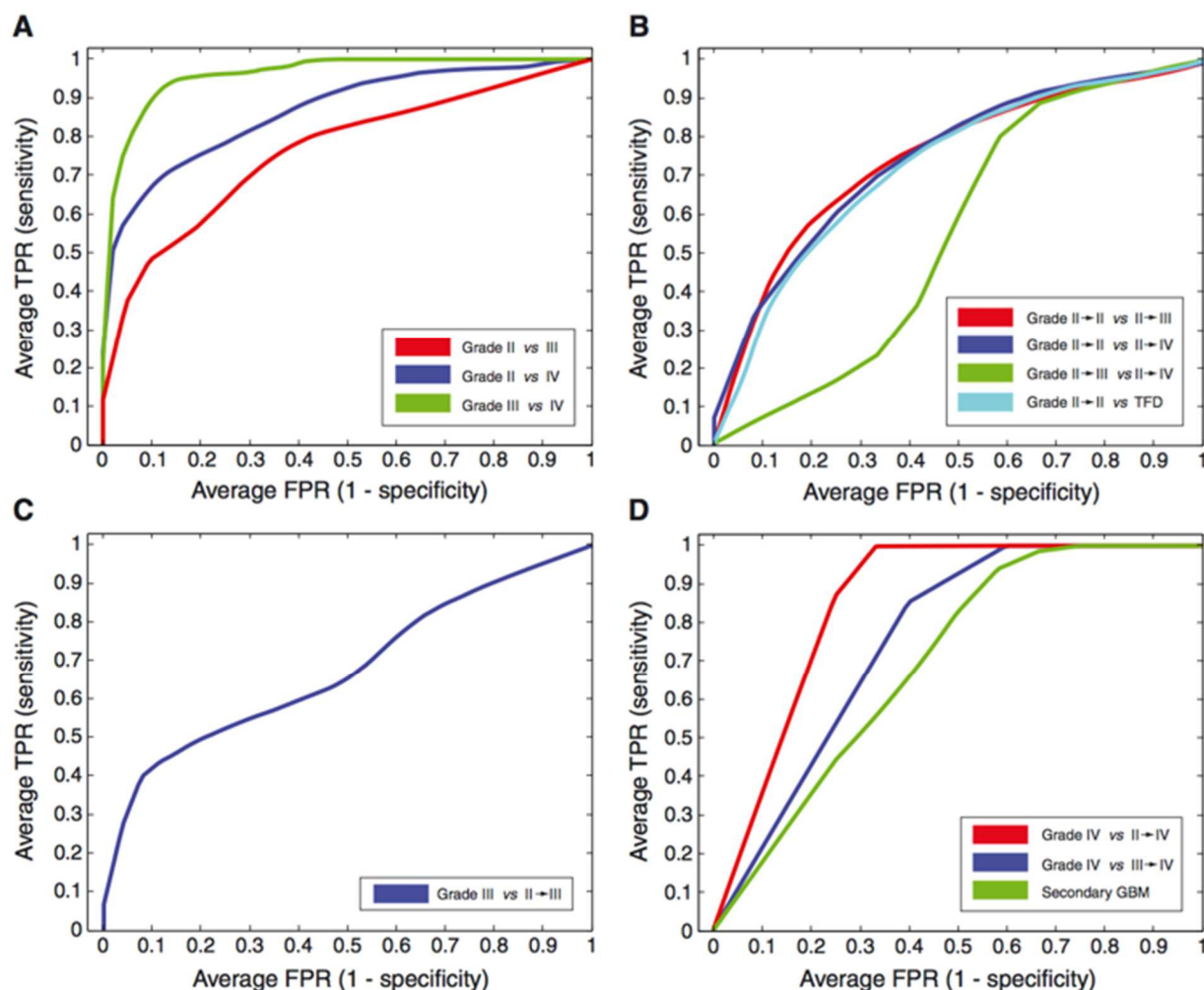
Figure 4.3. Average receiver operating characteristic (ROC) curves for the logistic ridge regression classification models shown in Table 3: primary glioma (A), recurrent low-grade glioma transformation status (B), primary versus secondary grade III (C), and primary versus secondary glioblastoma multiforme (GBM) (D). The averaged curves represent the results of 100 training sets per classification model. FPR, false positive rate; TFD, transformed to a higher grade of malignancy; TPR, true positive rate.

The classification models showed relatively high accuracy in categorizing the metabolite data according to grade (Table 4.3). There was an 84% accuracy in classifying primary grade II versus IV glioma, which underscored the utility of features such as 2HG, tGSH and MCI. Classification of primary grade II versus III glioma showed an accuracy of 73%, with the significant differences being in MCI, PE and Gly. Finally, grade III gliomas were separated from glioblastoma multiforme

(GBM) with an accuracy of 92% based on higher levels of 2HG, tCho, NAA and Cr/PCr. ROC curves that demonstrate the sensitivity and specificity for these classifications are shown in Fig. 4.3A.
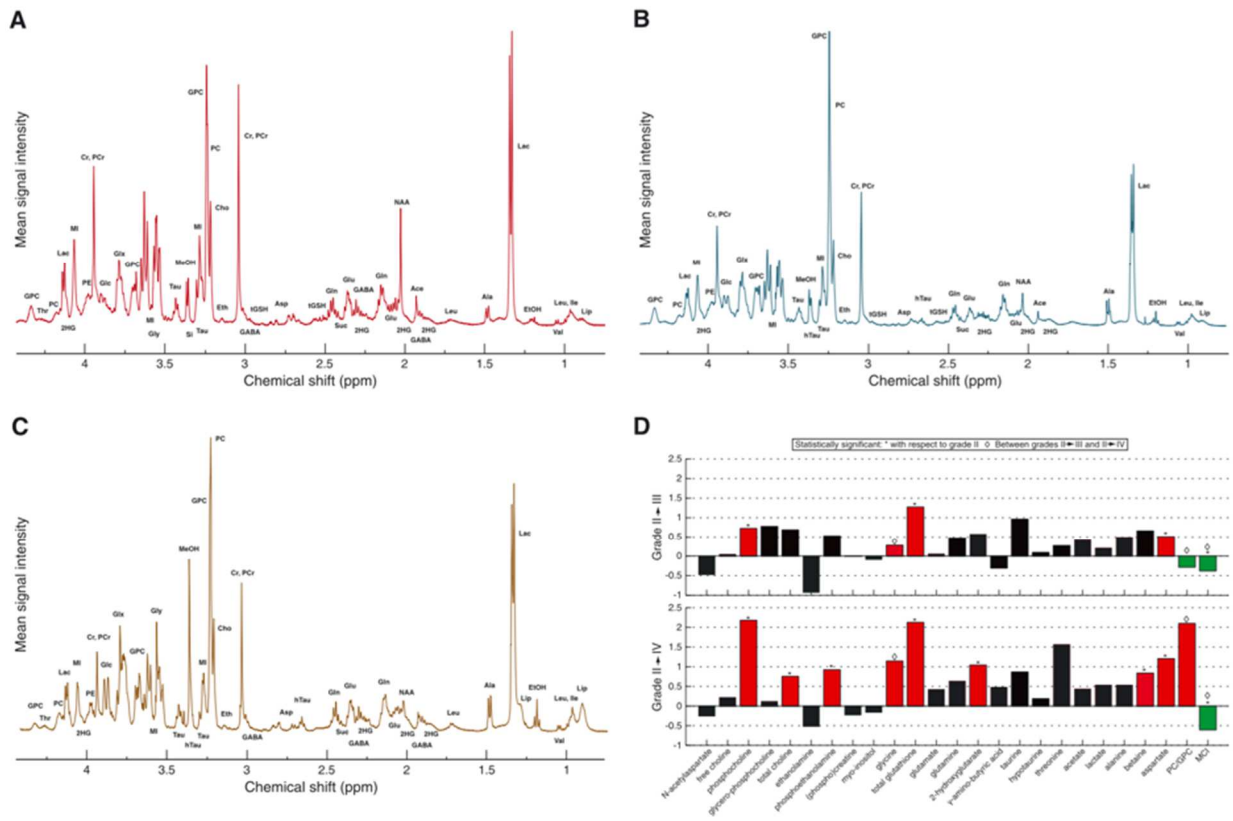
Figure 4.4. Metabolite profiles of recurrent low-grade glioma. Mean Carr–Purcell–Meiboom–Gill (CPMG) spectra for glioma samples histologically defined according to malignant transformation status as grade II → II (n = 43) (A), grade II → III (n = 52) (B) and grade II → IV (n = 19) (C). Deviation in quantified mean metabolite levels of grade II → III and II → IV glioma relative to grade II → II glioma; reported levels are unitless owing to the T_2 dependence of the CPMG acquisition (D). Significant increases or decreases in the metabolite levels displayed as residuals are highlighted in red and green, respectively. Statistical significance was defined as $p < 0.05$ for the comparative analysis among subtypes using the proportional odds logistic regression analysis. MeOH and EtOH are contaminants resulting from surgical sterilization procedures.

Transformation status for recurrent grade II glioma

As can be seen in Table 4.3, many of the lesions with an original diagnosis of grade II glioma were found to have undergone transformation to a higher pathological grade at recurrence. The largest portion of the tissue samples (46%) showed transformation to grade III ($G_{II\rightarrow III}$, n = 52) and 16% to grade IV ($G_{II\rightarrow IV}$, n = 19).

Peaks from the mean spectra (see Fig. 4.4A–C) corresponding to MI, Cr/PCr and NAA consistently discriminated gliomas that had remained grade II ($G_{II\rightarrow II}$) from their transformed counterparts ($G_{II\rightarrow III,IV}$). As was the case for primary glioma samples, there was a transition from GPC to PC as the dominant choline resonance and an increase in the abundance of Lip for grade IV lesions. Figure 4.4D demonstrates that transformation to higher grade was associated with a progressive increase in metabolite levels. Of particular interest is that the levels of PC (p = 0.05 and 0.005) and tGSH (p = 0.02 and 0.003) were significantly higher for both transitions, and that 2HG levels were significantly higher for $G_{II\rightarrow IV}$ (p = 0.01). MCI showed an opposite trend, being lower for both $G_{II\rightarrow III}$ (p = 0.02) and $G_{II\rightarrow IV}$ (p = 0.002) relative to $G_{II\rightarrow II}$. The statistical analysis represented in Table 4.4 emphasizes the significance of these changes.

Table 4.4. Metabolite levels of recurrent low-grade glioma. Relative metabolite levels for each subtype of glioma, displayed as mean±SEM; no units are expressed owing to the T_2 dependence of the CPMG acquisition.

Table 4. Metabolite levels of recurrent low-grade glioma. Relative metabolite levels for each subtype of glioma, displayed as mean ± standard error of the mean (SEM); no units are expressed owing to the T_2 dependence of the Carr–Purcell–Meiboom–Gill (CPMG) acquisition

	Grade II → II (n = 43)	Grade II → III (n = 52)	Grade II → IV (n = 19)	Overall	Grade II → II versus II → III	Grade II → II versus II → IV	Grade II → III versus II → IV
	Mean levels ± SEM			Odds ratios (95% CI)			
	Number of fitted spectral samples			p values			
PC	51 ± 7	88 ± 12	162 ± 41	1.010 (1.003–1.017)	1.013 (1.000–1.026)	1.018 (1.006–1.031)	1.006 (0.999–1.013)
	33	44	14	0.007	0.05	0.005	0.08
tCho	144 ± 19	243 ± 34	252 ± 43			1.005 (1.000–1.010)	
	39	52	17	0.06	0.08	0.03	NS
PE	110 ± 14	168 ± 22	211 ± 57	1.003 (1.001–1.006)		1.006 (1.001–1.011)	
	29	41	15	0.02	0.06	0.02	NS
Gly	152 ± 23	194 ± 20	327 ± 83	1.004 (1.001–1.007)			1.004 (1.000–1.007)
	25	39	13	0.006	NS	0.08	0.05
tGSH	35 ± 0.05	80 ± 11	109 ± 20	1.020 (1.006–1.035)	1.056 (1.007–1.108)	1.060 (1.020–1.101)	
	14	24	9	0.006	0.02	0.003	NS
2HG	32 ± 5	51 ± 8	66 ± 15	1.012 (1.003–1.022)	1.018 (1.001–1.035)	1.034 (1.007–1.061)	
	17	33	13	0.009	0.04	0.01	NS
Asp	125 ± 018	190 ± 23	277 ± 39	1.008 (1.002–1.014)	1.009 (1.000–1.017)	1.017 (1.005–1.030)	
	15	28	11	0.01	0.04	0.007	0.09
PC/GPC	110 ± 37	79 ± 10	344 ± 104				1.014 (1.002–1.026)
	31	42	12	NS	NS	NS	0.02
MCI	325 ± 27	201 ± 21	128 ± 13	0.994 (0.990–0.998)	0.995 (0.991–0.999)	0.981 (0.970–0.993)	0.995 (0.989–1.001)
	38	51	16	0.002	0.02	0.002	0.05
tCho/(P)Cr	98 ± 13	161 ± 19	204 ± 34	1.005 (1.001–1.010)		1.005 (1.000–1.010)	
	37	49	17	0.02	0.06	0.02	NS

2HG, D-2-hydroxyglutarate; Asp, aspartate; Cho, free choline; Cr, creatine; Gly, glycine; GPC, glycerophosphocholine; GSH, glutathione; GSSG, glutathione disulfide; MCI, myo-inositol to total choline index; NS, not significant; PC, phosphocholine; PCr, phosphocreatine; PE, phosphoethanolamine; tCho, total choline ([Cho] + [PC] + [GPC]); tGSH, total glutathione ([GSH] + [GSSG]).

The statistical models created to discriminate $G_{II \to II}$ versus $G_{II \to III}$ and $G_{II \to III}$ versus $G_{II \to IV}$ demonstrated classification accuracies of 69% and 73%, respectively (Table 4.3; Fig. 4.3B). Lower levels of tGSH in $G_{II \to II}$ and elevated levels of PC/GPC in $G_{II \to IV}$ were helpful in distinguishing $G_{II \to III}$. Modeling the optimal classification of $G_{II \to II}$ versus $G_{II \to IV}$ provided an accuracy of 74%, and selected the features of Asp, PC and tGSH as the strongest predictors of $G_{II \to IV}$, whereas high MCI strongly favored $G_{II \to II}$. When comparing all gliomas that had upgraded ($G_{II \to III,IV}$) with those that remained low grade ($G_{II \to II}$), the classification accuracy was 70%.

Table 4.5. Metabolite levels of primary versus secondary grade III glioma. Relative metabolite levels for each subtype of glioma, displayed as mean±SEM; no units are expressed owing to the T_2 dependence of the CPMG acquisition.

Table 5. Metabolite levels of primary *versus* secondary grade III glioma. Relative metabolite levels for each subtype of glioma, displayed as mean ± standard error of the mean (SEM); no units are expressed owing to the T_2 dependence of the Carr–Purcell–Meiboom–Gill (CPMG) acquisition

	Primary grade III ($n = 25$)	Grade II → III ($n = 52$)	Primary *versus* secondary grade III
	Mean levels ± SEM		Odds ratios (95% CI)
	Number of fitted spectral samples		*p* values
Cho	64 ± 9	40 ± 4	1.021 (1.003–1.039)
	21	48	0.02
NAA	24 ± 6	15 ± 3	1.019 (1.000–1.103)
	8	19	0.05
Gly	269 ± 34	194 ± 20	1.004 (1.001–1.008)
	20	39	0.03
PC/GPC	180 ± 81	79 ± 10	1.004 (1.000–1.008)
	13	42	0.03

Cho, free choline; Gly, glycine; GPC, glycerophosphocholine; NAA, *N*-acetylaspartate; NS, not significant; PC, phosphocholine.

Primary versus secondary grade III glioma

There were 25 primary grade III (G_{III}) and 52 secondary grade III ($G_{II→III}$) gliomas. Table 4.5 indicates that the primary lesions had significantly higher Cho (p = 0.02), Gly (p = 0.03) and PC/GPC (p = 0.03). The classification model of G_{III} versus $G_{II→III}$ yielded an accuracy of 77%, and indicated that there were relative elevations in GABA, Ala and GPC for primary lesions (Table 3; Fig. 4.3C).
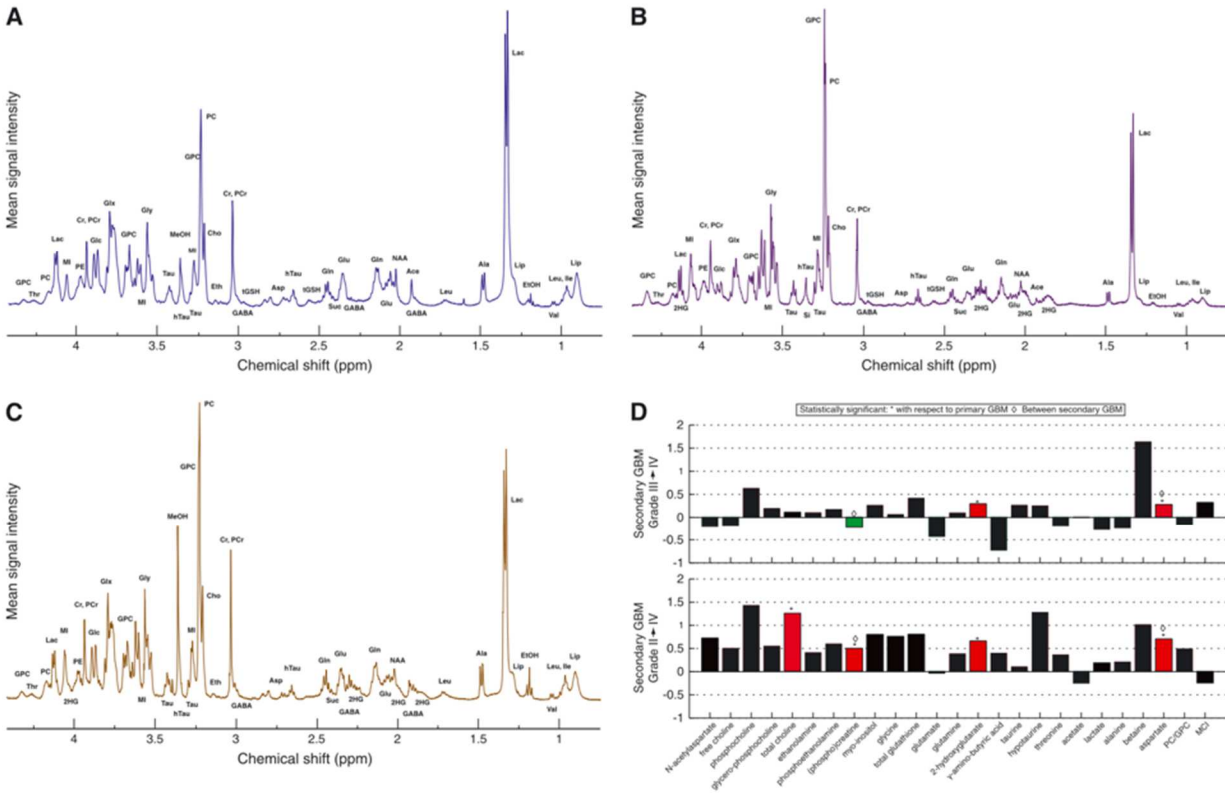
Figure 4.5. Metabolite profiles of primary versus secondary glioblastoma multiforme (GBM). Mean Carr–Purcell–Meiboom–Gill (CPMG) spectra for glioma samples histologically defined as primary grade IV (n = 101) (A) and secondary grade III → IV (n = 14) (B) or grade II → IV (n = 19) (C). Deviation in quantified mean metabolite levels of grade II → III and II → IV glioma relative to grade II → II glioma; reported levels are unitless owing to the T_2 dependence of the CPMG acquisition (D). Significant increases or decreases in the metabolite levels displayed as residuals are highlighted in red and green, respectively. Statistical significance was defined as $p < 0.05$ for the comparative analysis among subtypes using proportional odds logistic regression.

Primary versus secondary GBM

There were 101 samples from primary grade IV and 33 from secondary grade IV ($G_{II \rightarrow IV}$, n = 19; $G_{III \rightarrow IV}$, n = 14) glioma. The most obvious differences in the mean spectra (Fig. 4.5A–C) were the variations in the levels and relative contributions of GPC and PC, the lack of 2HG and the increase in the abundance of Lip. Overall, metabolite levels appeared to be higher in the lesions that arose from grade II glioma (Fig. 4.5C, D). Statistical analysis indicated that tCho, 2HG and Asp were

105

significantly higher in $G_{II \to IV}$ samples relative to the *de novo* G_{IV} (Fig. 4.5D and Table 4.6). Cr/PCr (p = 0.05) and MCI (p = 0.04) were significantly different for $G_{II \to IV}$ samples. Figure 4.6 shows spectra from a primary grade IV glioma (red) and a secondary grade IV glioma (blue) that arose from a recurrent grade II lesion. Differences in the portions of spectra corresponding to resonances of 2HG are clearly visible.

Table 4.6. Metabolite levels of primary versus secondary GBM. Relative metabolite levels for each subtype of glioma, displayed as mean±SEM; no units are expressed owing to the T_2 dependence of the CPMG acquisition.

Table 6. Metabolite levels of primary *versus* secondary glioblastoma multiforme (GBM). Relative metabolite levels for each subtype of glioma, displayed as mean ± standard error of the mean (SEM); no units are expressed owing to the T_2 dependence of the Carr–Purcell–Meiboom–Gill (CPMG) acquisition

	Grade IV (n = 101)	Grade III → IV (n = 14)	Grade II → IV (n = 19)	Overall	Primary GBM *versus* III → IV	Primary GBM *versus* II → IV	Grade III → IV *versus* II → IV
	Mean levels ± SEM			Odds ratios (95% CI)			
	Number of fitted spectral samples			p values			
tCho	112 ± 8	125 ± 27	252 ± 43	0.990 (0.984–0.996)		0.989 (0.981–0.996)	
	53	11	17	0.0004	NS	0.002	0.10
(P)Cr	95 ± 7	73 ± 14	143 ± 22	0.993 (0.987–0.999)		0.992 (0.985–0.998)	0.983 (0.966–1.000)
	50	9	18	0.03	NS	0.01	0.05
2HG	0*	30 ± 3	66 ± 15	0.846 (0.803–0.892)	0.824 (0.747–0.910)	0.830 (0.761–0.905)	
	101	7	13	<0.0001	0.0001	<0.0001	0.08
Asp	162 ± 12	208 ± 34	277 ± 39	0.991 (0.986–0.996)	0.994 (0.990–0.999)	0.991 (0.985–0.996)	
	44	6	11	0.001	0.01	0.002	NS
MI/(P)Cr	208 ± 23	334 ± 61	227 ± 24				1.010 (1.000–1.019)
	62	6	16	NS	0.12	NS	0.04
tCho/(P)Cr	140 ± 16	207 ± 38	204 ± 34	0.995 (0.990–0.999)	0.994 (0.990–0.999)	0.991 (0.985–0.996)	
	76	9	17	0.02	0.02	0.03	NS

2HG, ᴅ-2-hydroxyglutarate; Asp, aspartate; Cho, free choline; Cr, creatine; GPC, glycerophosphocholine; MI, myo-inositol; NS, not significant; PC, phosphocholine; PCr, phosphocreatine; tCho, total choline ([Cho] + [PC] + [GPC]).
*Absence of 2HG resonances confirmed by visual inspection.

The classification models for the discrimination between primary versus secondary grade IV glioma were highly accurate (Table 4.3; Fig. 4.3D), with the most valuable parameter being the level of 2HG. Accuracies for G_{IV} versus $G_{II \to IV}$ and G_{IV} versus $G_{III \to IV}$ models were 94% and 96%, respectively. Other parameters, such as tCho and Asp, were found to be useful for distinguishing the G_{IV} versus $G_{II \to IV}$ subgroups. The comparison between secondary GBM subtypes ($G_{II \to IV}$ versus $G_{III \to IV}$) showed an accuracy of only 62%.
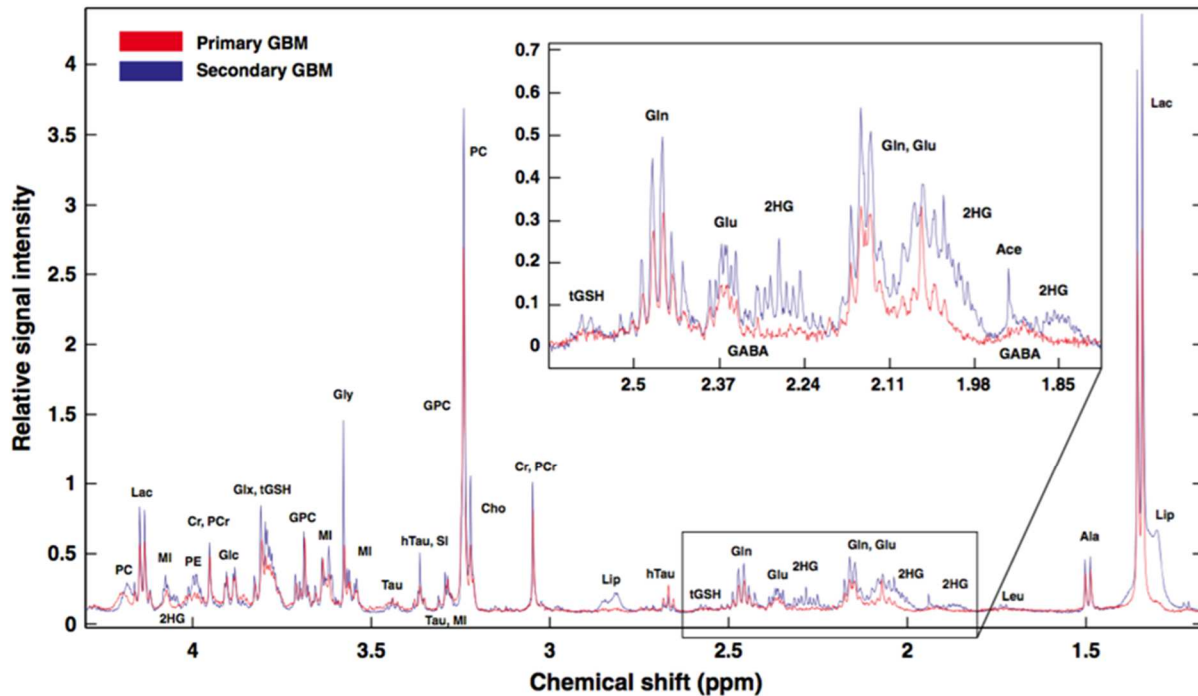
Figure 4.6. Representative spectra from primary versus secondary glioblastoma multiforme (GBM). Red trace represents the high-resolution magic angle spinning (HR-MAS) spectrum from a primary *de novo* GBM; blue trace represent the spectrum from a secondary GBM (grade II → IV). Spectra were normalized by the electronic reference to access in vivo concentrations (ERETIC) signal and tissue sample weights. This example shows the characteristic elevation of metabolites in secondary GBM relative to a primary counterpart, together with the distinguishing presence of the onco-metabolite 2HG.

Discussion

This study has provided a characterization of the spectral profiles for infiltrating gliomas. A critical finding was that ^{1}H HR-MAS spectroscopic techniques enabled an accurate classification of these diverse subtypes with respect to standard histological criteria and changes that are associated with malignant transformation at recurrence. This could be important for oncologists in selecting the most appropriate treatment for individual patients in cases in which there is no tissue available from the initial diagnosis. A further critical finding was that several of the ex vivo metabolite

changes observed could be translated into the in vivo setting. These results are of interest for improving the characterization of glioma for non-invasive diagnosis, planning of tissue sampling and surgical resection (21–27).

Table 4.7 summarizes the important clinical implications of our study according to relevant metabolite findings. A key application of these data is the guidance of tissue sampling at the time of initial diagnosis, given the importance of locating the most malignant region of the tumor for pathological grading. This study suggests that tCho, NAA, Cr/PCr, MI and Lac levels offer the most compelling information for determination of the tumor grade from an in vivo perspective. These metabolites are also of particular interest for studying lesion heterogeneity, especially in the case of grade IV glioma, where representative tissue samples may be difficult to obtain at the time of surgical resection. Similar criteria are also proposed in Table 4.7 for directing tissue sampling with regard to the determination of whether recurrent low-grade gliomas have undergone transformation to a higher grade, and may therefore require more aggressive treatment.

Table 4.7. Summary of relevant clinical implications. Metabolites and indices found to provide potential diagnostic value from this study are summarized according to major clinical needs and challenges.

Table 7. Summary of relevant clinical implications. Metabolites and indices found to provide potential diagnostic value from this study are summarized according to major clinical needs and challenges

1. Direction of tissue sampling at initial diagnosis

Imaging findings	Major challenge	Metabolite information
Non-enhancing lesion – usually grade II or grade III	To distinguish grade II *versus* grade III (IV)	Elevation of MI/tCho suggests grade II Target regions with highest tCho, low NAA, low Cr/PCr
Enhancing lesion, no necrosis – usually grade III or grade IV	To distinguish grade III (II) *versus* grade IV	Presence of 2HG implies grade II or III Target regions with high tCho, low NAA, low Cr/PCr in enhancing region
Enhancing lesion, with necrosis – almost always grade IV	To obtain samples that are representative of tumor properties	Use *in vivo* metabolite data to target regions with different characteristics, i.e. high tCho *versus* low tCho, ±lactate

2. Prediction of malignant transformation

Clinical need	Most relevant metabolite parameters
Targeting most malignant region at surgery	Low MCI, high tCho, low NAA, low Cr/PCr, presence of lactate
Non-invasive assessment of tumor progression	Decrease in MI and increase in tGSH and 2HG imply transformation from grade II to grade III or IV Elevated PC/GPC implies transformation to grade IV

3. Distinguishing between primary and secondary lesions

Clinical need	Most relevant metabolite parameters
Selection of most appropriate therapy	Elevated 2HG is evidence for a grade IV lesion having arisen from a prior grade II or grade III lesion
Determination of how treatment influences malignant progression	Use temporal changes in tCho, Gly, MCI and PC/GPC to monitor therapy

2HG, ᴅ-2-hydroxyglutarate; Cho, free choline; Cr, creatine; Gly, glycine; GPC, glycerophosphocholine; GSH, glutathione; GSSG, glutathione disulfide; MCI, myo-inositol to total choline index; MI, myo-inositol; NAA, *N*-acetylaspartate; PC, phosphocholine; PCr, phosphocreatine; tCho, total choline ([Cho] + [PC] + [GPC]); tGSH, total glutathione ([GSH] + [GSSG]).

The progressive reduction in MCI for lesions that have transformed from grade II to grade III or IV is a potentially important marker that can be monitored in vivo using short-echo ^{1}H MRSI, and may be able to predict transformation to a higher grade or distinguish between recurrent tumor and reactive gliosis (28). Whether other in vivo metabolite data can be used t o make a non-invasive diagnosis of malignant transformation will depend on the signal-to-noise ratio of the various peaks, the accuracy of the quantitative methods used and the magnitude of the changes that need to be detected. Although in vivo detection of tGSH and 2HG has also been reported (9,29–33), these peaks have low signal-to-noise ratios and are located in regions with overlapping spectra from other metabolites. The relative contributions of GPC and PC (4,27,34,35) are a strong *ex vivo* marker for the detection of transformation to grade IV that may relate to specific oncogenic

pathways (36), however their contributions to the tCho peak cannot be separated with *in vivo* ^{1}H MRSI. One possibility which may therefore be of interest for future studies of malignant transformation is the use of ultrahigh-field MR scanners to obtain in vivo ^{31}P MRSI spectra for assessing changes in PC/GPC.

The third application of this study (Table 4.7) is to distinguish between primary and secondary lesions, which is especially pertinent for selecting therapy and understanding the diversity of outcomes between patients who were originally thought to have similar pathology. We showed that secondary grade IV gliomas that arise from grade II (Fig. 4.3C, D) display a very unique profile that is visually characterized by elevations in 2HG, PC, PC/GPC ratio and hTau. The latter metabolite is an intermediate in the biosynthesis of Tau and a sulfur-bearing antioxidant like GSH, capable of reducing reactive oxygen species under conditions of oxidative stress (37,38). A previous HR-MAS study has also indicated that hTau is an important *ex vivo* biomarker for the separation of grade IV glioma and metastatic lesions (39).

The relationship between the levels of 2HG and mutations in the *IDH* genes (*IDH1* and *IDH2*) for up to 70% of lesions diagnosed as grade II glioma has important implications for distinguishing between primary and secondary gliomas (10). Although previous reports in the literature have indicated that 5–12% of primary grade IV gliomas carry IDH mutations (10,11,40), none of the tumors that presented as primary grade IV glioma in this study showed detectable levels of 2HG. This discrepancy may be a result of variations in patient populations between institutions and/or the time at which lesions were originally diagnosed. In either case, 2HG remains an important metabolite to monitor *in vivo*.

The evaluation of the genomic properties of primary and secondary grade III gliomas may also help in our understanding of how treatment history influences the processes associated with malignant progression. Although a substantial number of primary grade III glioma samples were found to be IDH mutant on the basis of immunohistochemistry, and to have detectable levels of 2HG, there were other differences in their metabolite profile relative to secondary anaplastic glioma, which included significantly lower levels of the tumor markers Gly (41) and PC/GPC. By contrast, transition from primary grade III to secondary grade IV glioma was mainly associated with an increase in tCho. This provides additional motivation for collecting tissue samples in the area of the lesion that is seen to have high tCho from ^{1}H MRSI. Although it was not assessed in this ex vivo study, results from in vivo measurements of Lac suggest that this metabolite can also identify important targets for directed tissue sampling (42,43).

Despite attempts to optimize the experimental design of this study, there were some inherent limitations that should be noted. The first concerns the possibility of the presence of differences in tumor cellularity between the portions of the samples that were used for histological and metabolite analysis. For this reason, we did not normalize metabolite levels by measures of tumor cellularity, but rather sought to identify robust patterns that were consistent across tumors of similar grade. The second is that the acquisition parameters used for this HR-MAS study meant that the estimated metabolite levels were weighted by their T_2 relaxation times. Despite this T_2 editing, the current literature has not indicated any statistically significant difference in T_2 values between gliomas of different grade (34,44). Moreover, a CMPG sequence was employed with varying TEs to determine whether differences in metabolite T_2 values could be observed between grade II (n = 3)

and grade IV (n = 4) samples, which represent opposite ends of the tumor cellularity spectrum, and no substantial difference was observed for the choline species, Cr/PCr and MI (data not shown).

A third limitation is that the number of samples analyzed in our study did not allow for further stratification on the basis of histological subtypes of low-grade glioma, such as astrocytoma, oligodendroglioma and the mixed oligoastrocytoma (1,2). Previous studies have indicated that there are differences in metabolite parameters among these subtypes (45,46). This may have influenced the accuracy with which we were able to distinguish between lesions that transformed from grade II to grade III versus those that remained grade II at recurrence. The fact that there was a higher proportion of lesions with an oligodendroglioma subtype in the population that remained grade II (57.1%) and a smaller proportion of lesions with this subtype in the group that transformed to grade III (36.0%) may explain sources of variance that were not adequately captured in the classification models of this study. Ongoing studies in our institution are collecting a larger number of samples in order to allow for a stratification of lesions by their respective histological subtype, and hence to observe how cellular origin relates to profiles of metabolism.

Conclusions

The results obtained in this study have elucidated the association between ^{1}H MRSI and the standard histological grading of gliomas that is used clinically for the diagnosis of patients and the determination of appropriate treatments. Metabolite profiles were able to help differentiate between primary glioma subtypes, predict the transformation of recurrent grade II to either grade

III or IV, and define the pathological trajectories of primary and secondary glioma of grades III and IV. These novel findings suggest that the discrete metabolomic profiles observed may be related to genomic or epigenomic abnormalities of specific glioma subtypes. Metabolites of significance from ex vivo analyses that can readily be observed using clinical MR scanners may also offer in vivo biomarkers to clinicians who are attempting to diagnose patients non-invasively and to monitor treatment. The metabolite profiles that have been identified could also help to characterize intra-lesional malignancy in a manner that is not currently addressed by the histopathological grading scheme, and may therefore aid in the delineation of targets for radiation planning and surgical intervention. This is critical for the clinical management of patients with glioma, and provides motivation for future studies that will examine the relationship between ^{1}H MRSI and genetic, epigenetic and biological variations in these lesions.

Acknowledgements

References

1. Lois DN, Ohgaki H, Wiestler OD, Cavenee WK, Burger PC, Jouvet A, Scheithauer BW,

113

Kleihues P. The 2007 WHO classification of tumours of the central nervous system. Acta Neuropathol. 2007; 114(2): 97–109.

2. Lopes MBS, VandenBerg SR, Scheithauer BW. The World Health Organization classification of nervous system tumors in experimental neuro-oncology. In Levine AJ, Schmidek HH (eds). Molecular Genetics of Nervous System Tumors. Wiley-Liss: New York; 1993, pp. 1–36.

3. Jaeckle KA, Decker PA, Ballman KV, Flynn PJ, Giannini C, Scheithauer BW, Jenkins RB, Bucknew JC. Transformation of low grade glioma and correlation with outcome: an NCCTG database analysis. J. Neurooncol. 2011; 104(1): 253–259.

4. Glunde K, Bhujwalla ZM, Ronen SM. Choline metabolism in malignant transformation. Nat. Rev. Cancer 2011; 11(12): 835–848.

5. Chow LM, Endersby R, Zhu X, Rankin S, Qu C, Zhang J, Broniscer A, Ellison DW, Baker SJ. Cooperativity within and among Pten, p53, Rb pathways induces high-grade astrocytoma in adult brain. Cancer Cell 2011; 19(3): 305–316.

6. Philips HS, Kharbanda S,Chen R, Forrest WF, Sorian RH, Wu TD, Misra A, Nigro JM, Colman H, Soroceanu L, Williams PM, Modrusan Z, Feuerstein BF, Aldape K. Molecular subclasses of high-grade glioma predict prognosis, delineate a pattern of disease progression, and resemble stages in neurogenesis. Cancer Cell 2006; 9(3): 157–173.

7. Verhaak RGW, Hoadley KA, Purdom E, Wang V, Qi Y, Wilkerson MD, Miller CR, Ding L, Golub T, Mesirov JP, Alexe G, Lawrence M, O'Kelly M, Tamayo P, Weir B, Gabriel S, Winckler W, Gupta S, Jakkula L, Feiler HS, Hodgson JG, James CD, Sarkaria JN, Brennen C, Kahn A,

Spellman PT, Wilson RK, Speed TP, Gray JW, Meyerson M, Getz G, Perou CM, Hayes DN. The Cancer Genome Atlas Research Network. Integrated genomic analysis identifies clinically relevant subtypes of glioblastoma characterized by abnormalities in PDGFRA, IDH1, EGFR, and NF1. Cancer Cell 2010; 17: 98–110.

8. Elkhaled A, Jalbert LE, Phillips JJ, Yoshihara HAI, Parvataneni R, Srinivasan R, Bourne G, Berger MS, Chang SM, Cha S, Nelson SJ. Magnetic resonance of 2-hydroxyglutarate in IDH1-mutated low-grade gliomas. Sci. Transl. Med. 2012; 4: 116ra5.

9. Andronesi OC, Kim GS, Gerstner E, Batchelor T, Tzika AA, Fantin VR, Vander Heiden MG, Sorenson GS. Detection of 2-hydroxyglutarate in IDH-mutated glioma patients by in vivo spectral-editing and 2D correlation magnetic resonance spectroscopy. Sci. Transl. Med. 2012; 4: 116ra4.

10. Yan H, Parsons DW, Jin G, McLendon R, Rasheed BA, Yuan W, Kos I, Batinic-Haberle I, Jones S, Riggins GJ, Friedman H, Friedman A, Reardon D, Herndon J, Kinzler KW, Velculescu VE, Vogelstein B, Bigner DD. IDH1 and IDH2 mutations in gliomas. N. Engl. J. Med. 2009; 360: 765–773.

11. Parsons DW, Jones S, Zhang X, Lin JC, Leary RJ, Angenendt P, Mankoo P, Carter H, Siu I, Gallia GL, Olivi A, McLendon R, Rasheed BA, Keir S, Nikolskaya T, Nikolsky Y, Busam D, Tekleab H, Diaz LA Jr, Hartigan J, Smith DR, Strausberg RL, Marie SKN, Shinjo SMO, Yan H, Riggins GJ, Bigner DD, Karchin R, Papadopoulos N, Parmigiani G, Vogelstein B, Velculescu VE, Kinzler KW. An integrated genomic analysis of human glioblastoma multiforme. Science 2008; 321: 1807–1812.

12. Houillier C, Wang X, Kaloshi G, Mokhtari K, Guillevin R, Laffaire J, Paris S, Boisselier B,

Idbaih A, Laigle-Donadey F, Hoang-Xuan K, Sanson M, Delattre JY. IDH1 or IDH2 mutations predict longer survival and response to temozolomide in low-grade gliomas. Neurology 2010; 75: 1560–1566.

13. Hartmann C, Hentschel B, Wick W, Capper D, Felsberg J, Simon M, Westphal M, Schackert G, Meyermann R, Pietsch T, Reifenberger G, Weller M, Loeffler M, von Deimling A. Patients with IDH1 wild type anaplastic astrocytomas exhibit worse prognosis than IDH1-mutated glioblastomas, and IDH1 mutation status accounts for the unfavorable prognostic effect of higher age: implications for classification of gliomas. Acta Neuropathol. 2010; 120: 707–718.

14. Park I, Chen AP, Zierhut M, Ozturk-Isik E, Vigneron DB, Nelson SJ. Implementation of 3T lactate-edited 3D ^{1}H MR spectroscopic imaging with flyback echo-planar readout for glioma patients. Ann. Biomed. Eng. 2011; 39: 193–204.

15. Basser PJ, Pierpaoli C. Microstructural and physiological features of tissues elucidated by quantitative diffusion-tensor MRI. J. Magn. Reson. B, 1996; 111: 209–219.

16. McKnight TR, Noworolski SM, Vigneron DB, Nelson SJ. Anautomated technique for the quantitative assessment of 3D-MRSI data from patients with glioma. J. Magn. Reson. Imaging 2001; 13: 167–177.

17. Albers MJ, Butler TN, Rahwa I, Bao N, Keshari KR, Swanson MG, Kurhanewicz, J. Evaluation of the ERETIC method as an improved quantitative reference for ^{1}H HR-MAS spectroscopy of prostate tissue. Magn. Reson. Med. 2009; 61: 525–532.

18. Stefan D, Cesare FD, Andrasescu A, Popa E, Lazariev A, Vescovo E, Strbak O, Williams S, Starcuk Z, Cabanas M, van Ormondt D, Graveron-Demily D. Quantitation of magnetic resonance

spectroscopy signals: the jMRUI software package. Meas. Sci. Technol. 2009; 20: 104035(9pp).

19. Ratiney H, Albers MJ, Rabeson H, Kurhanewicz J. Semi-parametric time-domain quantification of HR-MAS data from prostate tissue. NMR Biomed. 2010; 23: 1–13.

20. Opstad KS, Bell BA, Griffiths JR, Howe FA. An assessment of the effects of sample ischaemia and spinning time on the metabolic profile of brain tumour biopsy specimens as determined by high-resolution magic angle spinning H NMR. NMR Biomed. 2008; 21(10): 1138–1147.

21. Opstad KS, Wright AJ, Bell A, Griffiths JR, Howe FA. Correlations between in vivo ^{1}H MRS and ex vivo ^{1}H HR-MAS metabolite measurements in adult human gliomas. J. Magn. Reson. Imaging 2010; 31: 289–297.

22. Constantin A, Elkhaled A, Jalbert L, Srinivasan R, Cha S, Chang SM, Bajcsy R, Nelson SJ. Identifying malignant transformations in recurrent low grade gliomas using high resolution magic angle spinning spectroscopy. Artif. Intell. Med. 2012; 55(1): 61–70.

23. Vettukattil R, Gulati M, Sjobakk TE, Jakola AS, Kvernmo NA, Torp SH, Bathen TF, Gulati S, Gribbestad IS. Differentiating diffuse World Health Organization grade II and IV astrocytomas with ex vivo magnetic resonance spectroscopy. Neurosurgery 2013; 72(2): 186–195.

24. Sjobakk TE, Vettukattil R, Gulati M, Gulati S, Lundgren S, Gribbestad IS, Torp SH, Bathen TF. Metabolic profiles of brain metastases. Int. J. Mol. Sci. 2013; 14(1): 2104–2118.

25. Martinez-Bisbal MC, Marti-Bonmati L, Piquer J, Revert A, Ferrer P, Llacer JL, Piotto M, Assemat O, Celda B. 1H and 13C HR-MAS spectroscopy of intact biopsy samples ex vivo and in vivo ^{1}H MRS study of human high grade gliomas. NMR Biomed. 2004; 17(4): 191–205.

26. RutterA, Hugenholtz H,Saunders JK, Smith IC.Classificationofbrain tumors by ex vivo ^{1}H NMR spectroscopy. J. Neurochem. 1995; 64(4): 1655–1661.

27. Righi V, Roda JM, Paz J, Mucci A, Tugnoli V, Rodriguez-Tarduchy G, Barrios L, Schenetti L, Cerdan S, Garcia-Martin ML. [1]H HR-MAS and genomic analysis of human tumor biopsies discriminate between high and low grade astrocytomas. NMR Biomed. 2009; 22: 629–637.

28. Srinivasan R, Phillips JJ, Vandenberg SR, Polley MY, Bourne G, Au A, Pirzkall A, Cha S, Chang SM, Nelson SJ. Ex vivo MR spectroscopic measure differentiates tumor from treatment effects in GBM. Neuro-Oncol. 2010; 12: 1152–1161.

29. Opstad KS, Provencher SW, Bell BA, Griffiths JR, Howe FA. Detection of elevated glutathione in meningiomas by quantitative in vivo ^{1}H MRS. Magn. Reson. Med. 2003; 49: 632–637.

30. Thelwal PE, Yemin AY, Gillian TL, Simpson NE, Kasibhatla MS, Rabbani ZN, MacDonald JM, Blackband SJ, Gamcsik MP. Noninvasive in vivo detection of glutathione metabolism in tumors. Cancer Res. 2005; 65: 10149–10153.

31. Srinivasan R, Ratiney H, Hammond-Rosenbluth KE, Pelletier D, Nelson SJ. MR spectroscopic imaging of glutathione in the white and gray matter at 7 T with an application to multiple sclerosis. Magn. Reson. Imaging 2010; 28(2): 163–170.

32. Choi C, Ganji SK, DeBerardinis RJ, Rakheja D, Kovacs Z, Yang XL, Mashimo T, Taisanen JM, Marin-Valencia I, Pascual JM, Madden CJ, Mickey BE, Malloy CR, Bachoo RM, Maher EA. 2-Hydroxyglutarate detection by magnetic resonance spectroscopy in IDH-mutated patients with gliomas. Nat. Med. 2012; 18(4): 624–629.

33. Pope WB, Prins RM, Albert Thomas M, Nagarajan R, Yen KE, Bittinger MA, Salamon N, Chou AP, Yong WH, Soto H, Wilson N, Driggers E, Jang HG, Su SM, Schenkein DP, Lai A, Cloughesy TF, Kornblum HI, Wu H, Fantin VR, Liau LM. Non-invasive detection of 2-hydroxyglutarate and other metabolites in IDH1 mutant glioma patients using magnetic resonance spectroscopy. J. Neurooncol. 2012; 107(1): 197–205.

34. Usenius JP, Vainio P, Hernesniemi J, Kauppinen RA. Choline-containing compounds in human astrocytomas studied by ^{1}H NMR spectroscopy in vivo and in vitro. J. Neurochem. 1994; 63(4): 1538–1543.

35. Podo F. Tumour phospholipid metabolism. NMR Biomed. 1999; 12: 413–439.

36. Venkatesh HS, Chaumeil MM, Ward CS, Haas-Kogan DA, James CD, Ronen SM. Reduced phosphocholine and hyperpolarized lactate provide magnetic resonance biomarkers of PI3K/Akt/mTOR inhibition in glioblastoma. Neuro-Oncol. 2012; 14(3): 315–325.

37. Aruoma OI, Halliwell B, Hoey BM, Butler J. The antioxidant action of taurine, hypotaurine and their metabolic precursor. Biochem. J. 1988; 256(1): 251–255.

38. Brand A, Leibfritz D, Hamprecht B, Dringen R. Metabolism of cysteine in astroglial cells: synthesis of hypotaurine and taurine. J. Neurochem. 1998; 71: 827–832.

39. Wright AJ, Fellows GA, Griffiths JR, Wilson M, Bell BA, Howe FA. Ex vivo HRMAS of adult brain tumours: metabolite quantification and assignment of tumour biomarkers. Molec. Cancer, 2010; 9: 66.

40. Presner JR, Chinaiyan AM. Metabolism unhinged: IDH mutations in cancer. Nat. Med. 2011;

17: 291–293.

41. Righi V, Andronesi OC, Mintzopoulos D, Black PM, Tzika AA. High-resolution magic angle spinning magnetic resonance spectroscopy detects glycine as a biomarker in brain tumors. Int. J. Oncol. 2010; 36(2): 301–306.

42. Chang SM, Nelson SJ, Vandenberg S, Cha S, Prados M, Butowski N, McDermott M, Parsa AT, Aghi M, Clarke J, Berger M. Integration of preoperative anatomic and metabolic physiologic imaging of newly diagnosed glioma. J. Neurooncol. 2009; 92(3): 401–415.

43. Saraswathy S, Crawford FW, Lamborn KR, Pirzkall A, Chang S, Cha S, Nelson SJ. Evaluation of MR markers that predict survival in patients with newly diagnosed GBM prior to adjuvant therapy. J. Neurooncol. 2009; 91(1): 69–81.

44. Li Y, Srinivasan R, Ratiney H, Lu Y, Chang SM, Nelson SJ. Comparison of T_1 and T_2 metabolite relaxation times in glioma and normal brain at 3T. J. Magn. Reson. Imaging 2008; 28(2): 342–350.

45. Chawla S, Oleaga L, Wang S, Krejza J, Woo JH, O'Rourke DM, Judy KD, Grady MS, Melhem ER, Poptani H. Role of proton magnetic resonance spectroscopy in differentiating oligodendrogliomas and astrocytomas. J. Neuroimaging 2010; 20(1): 3–8.

46. Huang J, Gholami B, Agar NYR, Norton I, Haddad WM, Tannenbaum AR. Classification of astrocytomas and oligodendrogliomas from mass spectrometry data using sparse kernel machines. Engineering in Medicine and Biology Society, EMBC, Annual International Conference of the IEEE, Boston, Massachusetts, USA, 2011; 7965–7968.

Chapter 5: Characterization of *ex vivo* metabolic profiles, histological and *in vivo* MR parameters for regions of non-enhancing versus enhancing tumor in patients with GBM

This chapter presents original research that characterizes contrast-based radiographic subtypes of GBM according to parameters derived from HR-MAS spectroscopy, pathology, and *in vivo* MR imaging. Given the difficulty in detecting non-enhancing disease with conventional MRI, we sought to determine whether spectroscopy could potentially add diagnostic value. Using T_1-weighted anatomical imaging in combination with physiologic imaging to putatively define contrast-enhancing and non-enhancing tumor targets, several tissue specimens were obtained during surgical resection, as previously described. Histologically-confirmed tumor was evaluated by HR-MAS and analyzed at the site of removal on prior *in vivo* imaging, including MRS, PWI, and DWI. Leveraging this unprecedented characterization, the study provides practical guidelines for identifying non-enhancing GBM, which may assist in surgical planning and the monitoring of therapy.

Authors:

Adam Elkhaled, Joanna J. Phillips, Stojan Maleschlijski, Ritu Roy, Annette M. Molinaro, Susan M. Chang, Soonmee Cha, Janine M. Lupo and Sarah J. Nelson

Abstract

Background: Although the contrast-enhancing (CE) lesion on T_1-weighted MR images is widely used as a surrogate for tumor, regions of hyperintensity on T_2-weighted images that are outside of the CE lesion may also contain tumor. This study sought to characterize *ex vivo* metabolic profiles

of samples from within CE and NE regions of GBM and to compare them with histological and *in vivo* MR parameters to assist in defining criteria for estimating total tumor burden.

Methods: Fifty-six patients with newly diagnosed GBM received a multi-parametric pre-surgical MR examination. Targets for obtaining image-guided tissue samples were defined based on *in vivo* parameters that were suspicious for tumor. The actual location from where tissue samples were obtained was recorded, and half of each sample was analyzed for histopathology while the other half was scanned using HR-MAS spectroscopy.

Results: Tumor samples from within CE and NE regions demonstrated comparable mitotic activity, but there was significant heterogeneity in microvascular morphology. *Ex vivo* spectroscopic parameters that were similar between NE and CE samples included levels of total choline and N-acetylaspartate, with differences in levels of myo-inositol, creatine/phosphocreatine, and phosphoethanolamine. Analysis of *in vivo* parameters at the sample locations were consistent with the histological and *ex vivo* metabolic data.

Conclusions: The similarity between *ex vivo* levels of choline and NAA, and between the *in vivo* levels of choline, NAA and nADC in CE and NE tumor indicate that these parameters can be used in defining non-invasive metrics of total tumor burden for patients with GBM.

Key words: non-enhancing GBM, image-guided, HR-MAS, MRSI, spectroscopy

Importance of the study: The importance of this study derives from its multi-parametric characterization of non-enhancing GBM that includes *ex vivo* ultra high-resolution spectroscopy, *in vivo* MR imaging and extensive histopathological analysis. Building upon previous assessments of contrast-based radiographic subtypes of disease, distinct metabolite expression was revealed in

non-enhancing GBM, as well as unique perfusion and vascular traits. Based on intra-tumoral heterogeneity and differences with extra-tumoral tissue, these findings were translated into practical guidelines for delineating non-enhancing disease prior to surgery and during routine MR examinations using DWI and MR spectroscopy.

Introduction

Glioblastoma (GBM) is the most common form of infiltrating glioma in adults with the highest level of malignancy based upon histopathologic criteria developed by the World Health Organization (1). Defining tumor margins for GBM is complicated by their potential for proliferation and invasion into surrounding parenchyma. Median survival with standard-of-care treatment is around 14 months (2) and has remained similar over recent years, despite vigorous research into novel therapeutic agents and whole genome mutational analyses. Given the relatively rapid course of the disease, patients are routinely examined every two months by magnetic resonance (MR) imaging to discern whether radiographic progression has occurred and to modify clinical intervention accordingly.

Routine MR examinations exploit the vascular pathology of GBM, which is characterized by immature and tortuous growth of tumor microvasculature. This leads to blood-brain barrier (BBB) permeability that can be interrogated via the leakage of T_1-sensitive paramagnetic contrast agents. The most commonly utilized agent in clinical practice is gadolinium (Gd) that has been chelated with diethylene triamine pentaacetic acid (Gd-DTPA) to reduce toxicity to patients (3). Extravasation of Gd-DTPA causes a local reduction in the T_1 relaxation time and reveals regions

of elevated signal where the BBB is compromised on T_1-weighted MR images. Increased blood volume and vessel permeability within and beyond the contrast enhancing (CE) lesion can be evaluated using advanced techniques such as dynamic susceptibility contrast (DSC) and dynamic contrast enhanced (DCE) perfusion-weighted MR imaging.

The other type of MR data used for routinely evaluating GBM is fluid-attenuated inversion recovery (FLAIR) T_2-weighted images. Regions that are hyperintense on FLAIR imaging and extend beyond the borders of the CE lesion are referred to as the non-enhancing (NE) lesion. Although part of the NE lesion contains vasogenic edema and other non-specific changes, there may also be substantial regions of infiltrative tumor (4). The recent use of anti-angiogenic agents has added to the ambiguity in interpreting imaging data, because they act by diminishing vascular permeability and can cause a reduction in the size of both the CE and NE lesions, while not necessarily changing the number of tumor cells present.

Other imaging modalities that are thought to be associated with tumor characteristics include diffusion-weighted imaging (DWI) and metabolic imaging using *in vivo* ^{1}H MRSI. Although there have been reports of a linear correlation between tumor cellularity and restricted diffusivity, it is unclear whether this assumption applies to tumor in NE as well as CE lesions. Numerous studies from our own as well as other groups have demonstrated the ability of ^{1}H MRSI to highlight areas of tumor in the NE lesion based upon a combination of increased levels of choline and reduced levels of NAA (5).

The purpose of this study was to obtain image-guided tissue samples from CE and NE regions that were subsequently confirmed to correspond to tumor in order to characterize the similarities and differences between their histological and *ex vivo* spectroscopic profiles. By saving the locations where the actual tissue samples were obtained during surgery, it was also possible to compare the corresponding *in vivo* anatomic, ^{1}H MRSI, DWI, and DSC imaging parameters between the two groups.

Materials and Methods

Patient population

The institutionally approved study comprised 56 treatment-naïve patients who underwent surgical resection for suspected GBM and provided informed consent for removal of image-guided tissue samples. The diagnosis of tumor grade was subsequently confirmed by a single pathologist according to standard histological criteria (1).

Pre-operative MR Exam

A multi-parametric MR examination was conducted within 24 hours prior to surgery using either 1.5- or 3-T whole-body MR scanners (GE Healthcare Technologies, Milwaukee, Wisconsin, USA) with an 8-channel, phased-array headcoil for signal reception (MRI Devices, Knaresborough, United Kingdom). The data obtained included 3-D pre- and post-contrast T_1-weighted inversion recovery spoiled-gradient echo (IRSPGR) images (TR/TE/TI = 8/3/400 ms, 1.5 mm slices, 15º flip angle, 512 x 512 matrix, 1 mm in-plane resolution) and T_2-weighted anatomic FLAIR and fast spin echo (FSE) images (see Supplementary Material). In 45/56 cases, diffusion-weighted imaging was

acquired in the axial plane with spin-echo echo-planar-imaging (TR/TE = 1000/108 ms; voxel size, 1.7 x 1.7 x 3 mm^3; 6 gradient directions; 4 NEX; b = 1000 s/mm^2) and, in 24/56 cases, lactate (Lac)-edited three-dimensional ^{1}H MRSI at 3T. The latter applied point-resolved spectroscopic selection (PRESS) for volume localization and very selective saturation (VSS) pulses for lipid (Lip) signal suppression (excited volume, ~80 x 80 x 40 mm^3; overpress factor, 1.5; TR/TE = 1104/144 ms; field of view, 16 x 16 x 16 cm^3; nominal voxel size, 1 x 1 x 1 cm^3; flyback echo-planar readout gradient in the superior-inferior direction; 712 dwell points; sweep width, 988 Hz) (6). DSC perfusion imaging was acquired in 45/56 cases as a series of T_2*-weighted echo-planar images (TR/TE/flip angle = 1250–1500ms/35–54ms/30–35 degrees, 128 × 128 matrix, slice thickness = 3 – 5 mm, 7 – 15 slices with 60 – 80 timepoints) using a 5 mL/s bolus injection of 0.1 mmol/kg body weight Gd-DTPA (Magnevist, gadopentetate dimeglumine) .

Definition of Targets for Tissue Sampling

In vivo data from the pre-operative examination were transferred to a Unix workstation and in-house software were applied to derive estimates of diffusion, spectroscopic and perfusion parameters. Maps of the apparent diffusion coefficient (ADC) and fractional anisotropy (FA) were generated on a pixel-by-pixel basis (7). The ^{1}H MRSI data were processed as described previously (8) in order to quantify peak heights and areas of total choline (tCho), creatine (Cr/PCr), N-acetylaspartate (NAA), lactate (Lac) and lipid (Lip). Maps of the tCho-to-NAA index (CNI) were derived using an automated iterative linear regression-based algorithm that sequentially removes outlying values and represents the changes in tCho and NAA levels relative to the normal voxels from the same subject (9). DSC perfusion data were processed to generate estimates of cerebral blood volume (CBV) by either fitting dynamic curves using a modified gamma-variate function

(10) or using a non-parametric procedure to estimate peak height (PH) and percent recovery (REC) (11).

Image-guided tissue sampling

One to four tissue targets were identified, based upon observations from previous studies, as being within the CE or NE region using either (i) ADC values less than 1.5 times normal appearing white matter, (ii) CNI values greater than 2, or (iii) CBV values greater than 3. These targets were superimposed upon the T_1-weighted post-contrast images as spherical regions of interest (ROIs) with a diameter of 5 mm, and transferred to the surgical navigation workstation (BrainLAB Inc., Munich, Germany).

While it was not always feasible to resect samples from the pre-defined tissue targets, the surgeon used the image guidance software to provide samples from the nearest accessible regions. The actual sample location was saved on the BrainLAB workstation as both screenshots and files of RAS coordinates relative to the pre-surgery images. After excision, the tissue samples were immediately bisected: half was snap frozen in liquid nitrogen less than 1 min after removal and stored at −80 °C for 1H HR-MAS spectroscopy; the other half was fixed in 10% zinc formalin, dehydrated by graded ethanols and embedded in Paraplast Plus wax (McCormick Scientific, St. Louis, Missouri, USA) using standardized techniques for pathological analysis.

Definition of *in vivo* Parameters

ROIs corresponding to the CE lesion and any area of necrosis (NEC) were manually defined on the T_1 post-contrast images. The T_2 lesion was defined as the region of hyperintensity on the T_2-

weighted FLAIR image and expanded where necessary to include the CE lesion and NEC. The

NE lesion was defined as the entire T_2 lesion minus the CE lesion and NEC. A brain region of

interest was defined using the brain extraction tool in FSL (12), and normal-appearing brain (NAB)

was defined as the entire brain minus the T_2 lesion. Spherical regions with 5-mm-diameter and

centered at the coordinates obtained by BrainLab from the actual site of tissue removal were

defined and visually confirmed as corresponding to the screenshots acquired during surgery.

Target ROIs with greater than 50% contrast-enhancement were classified as enhancing (Enh+),

while ROIs confined to the NEL were considered non-enhancing (Enh-). Figure 5.1 depicts Enh+

(A) and Enh- (B) regions that were confirmed as tumor.

In vivo parameters from within sample ROIs were determined by histogram analysis of pixel

intensities. For the anatomic and DWI parameters, normalized intensity values were obtained by

dividing median intensities in the corresponding ROI by the mode of the intensity in the ROI from

NAB. For the H-1 spectroscopic data, metabolite levels were obtained by sinc-interpolating these

maps to create intensities at the location of the center of the sample ROI. Normalization factors

for tCho, Cr and NAA were defined as median metabolite level values from the subset of 'normal'

voxels that were defined from the CNI algorithm. Levels of Lac and Lip were normalized relative

to the NAA in normal voxels. The CBV, PH and REC were obtained within sample ROIs as
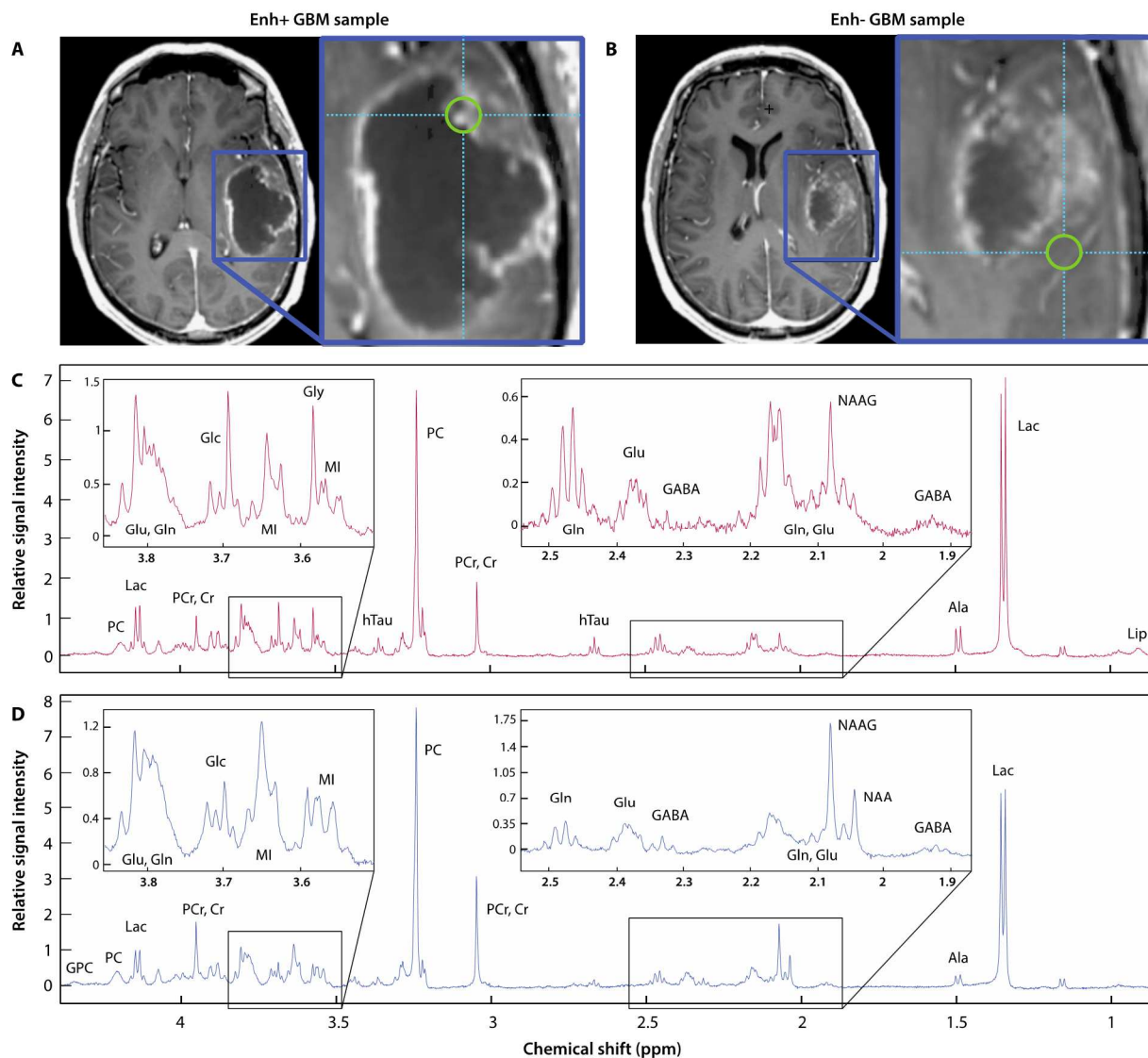
described previously (10, 11).

Figure 5.1. Image-guided tissue from a patient with GBM designated as Enh+ (A) or Enh- (B) on the basis of post-contrast T_1 IRSPGR images. Corresponding CPMG ^{1}H HR-MAS spectra for Enh+ (C) and Enh- (D) tumor samples. NAAG, N-acetylaspartylglutamate.

Histological analysis of the tumor

An experienced neuropathologist evaluated the slides prepared from tissue samples with hematoxylin and eosin (H&E) stains to determine the relative contribution of tumor cells to the overall cellularity. A score of '0' denoted neuropil without tumor; '1' indicated an infiltrating tumor margin containing detectable but not abundant numbers of tumor cells; '2' denoted a more cellular infiltrated zone; and '3' denoted highly cellular tumor with relatively few non-neoplastic cells. Only tissue samples with scores greater than zero were included in the analysis. Further H&E and immunohistochemical analyses were performed to determine overall cellularity, necrosis content, mitoses (MIB-1), hypoxia (CA9), axonal disruption (SMI-31), and microvascular morphology (Factor VIII) (see Supplementary Material).

^{1}H HR-MAS spectroscopy

Tissue samples weighing between 1.11 and 30.42 mg (median, 10.25 mg) were evaluated. A 35-µL zirconia rotor (custom-designed by Varian, Palo Alto, California, USA) was used with 3 µL of 99.9% atom-D deuterium oxide containing 0.75 wt% 3-(trimethylsilyl)propionic acid (Sigma-Aldrich, St. Louis, Missouri, USA) for chemical shift referencing. Data were acquired at 11.7 T at 1 °C with a spin rate of 2250 Hz in a 4-mm gHX nanoprobe with a Varian INOVA 500-MHz multi-nuclear spectrometer.

A rotor-synchronized, one-dimensional, Carr–Purcell–Meiboom–Gill (CPMG) pulse sequence was run with TR/TE = 4s/144ms, 512 scans, 40000 acquired points, 90° pulse and spectral width

of 20 kHz for a total time of 35 min. A relatively long TE was used to maximally suppress the macromolecular background for purposes of metabolite fitting. The electronic reference to access *in vivo* concentrations (ERETIC) method was used to generate an artificial electronic signal that served as an external standard for the estimation of metabolite levels (13).

Pre-processing of the spectra was performed in the time domain using the Java-based Magnetic Resonance User Interface (jMRUI) (14). The estimation of relative one-dimensional metabolite levels was achieved with the semi-parametric algorithm, high-resolution quantum estimation (HR-QUEST), which fits a customized basis set of metabolites to the spectrum (15). The basis set used in this study comprised spectra from 26 metabolite solutions commonly studied in the human brain (Sigma-Aldrich): NAA, free choline (Cho), phosphocholine (PC), glycerophosphocholine (GPC), ethanolamine (Eth), phosphoethanolamine (PE), creatine/phosphocreatine (Cr/PCr), myo-inositol (MI), scyllo-inositol (SI), glucose (Glc), glycine (Gly), total glutathione [tGSH: glutathione (GSH) + glutathione disulfide (GSSG)], glutamate (Glu), glutamine (Gln), 2HG, γ-aminobutyric acid (GABA), taurine (Tau), hypotaurine (hTau), threonine (Thr), acetate (Ace), Lac, alanine (Ala), betaine (Bet), aspartate (Asp), valine (Val) and succinate (Suc). Total choline (tCho) was defined as [PC + GPC + Cho] for comparison with the *in vivo* data. Only metabolite estimates with Cramer-Rao errors less than 12% were included in subsequent analyses. In order to estimate lipid (Lip) content, the area under the methyl Lip resonance, centered at approximately 0.9 ppm, was evaluated over the interval [0.936 0.850] ppm in MATLAB, and normalized by sample weight and ERETIC peak area. Figure 5.1 shows *ex vivo* spectra corresponding to regions of Enh+ (Fig. 5.1A,C) and Enh- (Fig. 5.1B,D) tumor.

Statistical Analysis

Tissue samples with tumor scores of 1-3 were evaluated according to a random mixed effects model in R v3.3.2 (16) that accounted for patients with multiple tissue samples. Odds ratios and *p*-values are reported for continuous imaging and histopathological parameters that were determined to predict enhancement status when accounting for repeated specimen sampling. Ordinal histopathology parameters were compared between Enh+ and Enh- tumor samples using a proportional odds logistic regression model in SAS that also accounted for repeated sampling (17). Pair-wise correlations were assessed for continuous and ordinal variables using the Pearson product-moment correlation test and Kendall tau rank correlation, respectively. Each correlation was run 50 times with a random tumor sample selected per patient upon every iteration; the mean and standard deviations for tau estimates are reported along with median *p*-values. Bonferoni correction was applied for multiple correlations among 116 derived parameters.

Results

Summary of analyzed tumor tissue

As shown in Table 5.1, a total of 102 tumor samples (70 Enh+, 32 Enh-) were acquired from the 56 subjects that were evaluated.

Table 5.1. Summary of analyzed patients and sampled GBM with enhancement classification

Number of patients	Number of tissue samples
11	14 Enh+, 13 Enh-
34	56 Enh+
11	19 Enh-
56 total	**102 total (70 Enh+, 32 Enh-)**

^{1}H HR-MAS spectroscopy

To provide a visual comparison between metabolite profiles of Enh+ and Enh- GBM samples, individual spectra were normalized by the sample weight and ERETIC peak area, then averaged together according to enhancement status. The composite spectra shown in Fig. 5.2 for Enh+ (red) and Enh- (blue) GBM reveal the characteristic features of these distinct radiographic entities. These demonstrate that phosphocholine (PC), rather than glycero-phosphocholine (GPC), is the dominant choline species. Trace levels of N-acetylaspartate (NAA) and the presence of hypo-taurine (hTau) in these samples corroborated the pathological analysis of the tissue. The Enh- tissue samples displayed elevated levels of phosphoethanolamine (PE), creatine/phosphocreatine (Cr/PCr), glycine (Gly), myo-inositol (MI), and GPC. The Enh+ samples demonstrated higher methyl lipid (Lip).
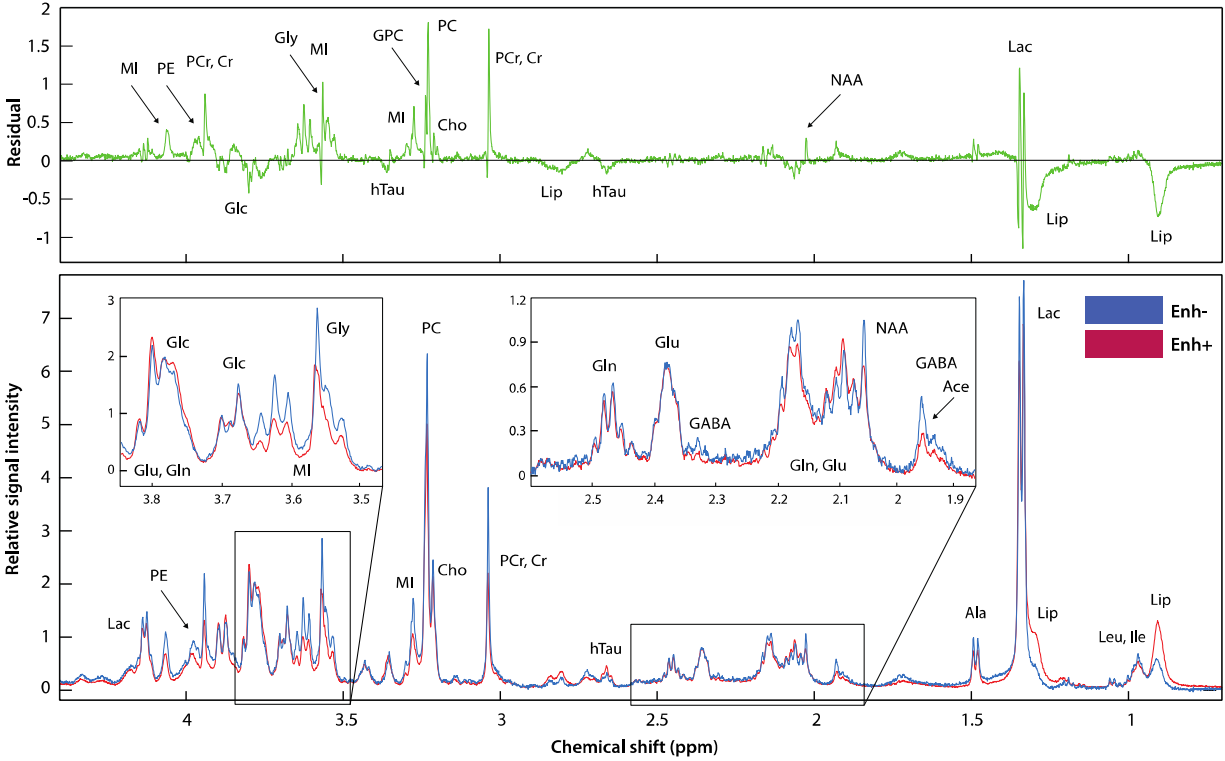
Figure 5.2. Mean CPMG ^{1}H HR-MAS spectra for image-guided Enh+ (red, $n =$ 70) and Enh- (blue, $n = 32$) GBM samples. The residual of Enh- minus Enh+ spectra is shown in green.

Results from the random mixed effects model were consistent with the visual assessments and are shown in Table 5.2. Lactate (Lac) was not considered in the analysis because of its lack of reliability in the *ex vivo* setting (18). The Enh- GBM had significantly elevated MI ($p = 0.003$), Cr/PCr ($p = 0.009$), and PE ($p = 0.05$) compared to Enh+ samples, with a similar trend for Gly. Enh+ tumor samples showed a trend towards elevated methyl Lip ($p = 0.07$), but there was no difference observed in tCho levels (Table 5.2).

There were significant correlations between a number of metabolites for either all samples or the Enh+ samples. In particular, levels of PE were shown to correspond to levels of tCho ($p=0.0001$), glutamate (Glu, $p=0.002$), threonine (Thr, $p=0.002$), and alanine (Ala, $p=0.00002$), which were

134

intercorrelated (see Supplementary Table S5.1). For the same groups of samples, levels of MI were

linked to those of tCho (p=0.009) (Table S5.1). No significant correlations were found among the

Enh- GBM after correction for multiple comparisons.

Table 5.2. Statistical results from random mixed effects model. Metabolite levels are unitless.

		Enh+	Enh-	Odds ratio (95% CI)	p-value
		Mean ± SE (n)			
HR-MAS	MI	1.37 ± 0.12 (53)	2.19 ± 0.35 (23)	0.57 (0.39 - 0.83)	0.003
	Cr/PCr	1.03 ± 0.10 (52)	1.48 ± 0.15 (21)	0.44 (0.24 - 0.82)	0.009
	PE	1.32 ± 0.12 (53)	1.88 ± 0.28 (24)	0.51 (0.28 - 0.94)	0.05
	Lip	8.51 ± 1.70 (70)	4.67 ± 0.53 (32)	1.19 (0.99 - 1.43)	0.07
	Gly	2.21 ± 0.34 (48)	4.34 ± 1.38 (16)	0.86 (0.73 - 1.00)	0.06
	GPC	0.58 ± 0.07 (46)	0.81 ± 0.13 (21)	0.44 (0.18 - 1.07)	0.07
Anatomic	nT1c	1.52 ± 0.01 (68)	0.91 ± 0.01 (29)	140 (23 – 880)	1×10^{-7}
	nFL	1.69 ± 0.01 (67)	1.61 ± 0.01 (29)	NA	NS
	nFSE	2.17 ± 0.01 (63)	1.96 ± 0.03 (29)	NA	NS
Perfusion	nCBV	2.91 ± 0.48 (28)	1.39 ± 0.11 (20)	3.51 (1.46 - 8.41)	0.005
	nPH	2.23 ± 0.33 (28)	1.23 ± 0.09 (20)	4.31 (1.30 - 14.30)	0.02
	REC (%)	75.94 ± 2.46 (28)	84.27 ± 2.27 (20)	0.93 (0.87 - 1.00)	0.04
Diffusion	median	1.54 ± 0.01 (53)	1.44 ± 0.01 (28)	NA	NS
	nADC	0.73 ± 0.01 (51)	0.97 ± 0.01 (25)	0.14 (0.02 - 0.55)	0.01
	median nFA				
¹H MRSI	nCr/PCr	0.51 ± 0.03 (26)	0.93 ± 0.10 (11)	0.22 (0.04 - 1.26)	0.09
	nLac	0.52 ± 0.07 (26)	0.30 ± 0.06 (11)	17.65 (0.84 - 370)	0.07
	nLip	0.86 ± 0.19 (26)	0.59 ± 0.14 (11)	NA	NS

		Enh+	Enh-	Odds ratio (95% CI)	*p*-value
		Mean ± SE (n)			
	CNI	6.75 ± 0.90 (26)	6.69 ± 0.84 (11)	NA	NS
Histopathology	MIB-1 (%)	14.86 ± 0.33 (68)	12.88 ± 0.23 (30)	NA	NS
	average cellularity (cells)	286 ± 2 (67)	287 ± 6 (30)	NA	NS

In vivo Imaging

As expected, the normalized T_1 post-contrast (nT1c) intensities were much higher in the Enh+ ROIs corresponding to the regions where enhancing GBM was sampled intra-operatively (p=1 x 10^{-7}) (Table 5.2). The normalized FLAIR (nFL) and FSE values showed no significant difference in intensities. Perfusion-derived parameters demonstrated clear distinctions between Enh+ versus Enh- tissue, with the measures of perfusion peak height (nPH, p =0.02) and cerebral blood volume (nCBV, p = 0.005) being elevated in Enh+ relative to Enh- GBM, while the percent recovery (REC, p = 0.04) was found to be reduced in Enh+ GBM, indicating greater leakage (Table 5.2). Although the nADC values showed no difference, the median normalized values of fractional anisotropy (nFA) were lower in Enh+ (p =0.01) relative to Enh- targets (Table 5.2).

Lactate-edited ^{1}H MRSI data were obtained for a smaller subset of patients because it was not always possible to add the additional sequence in the clinical setting and because the selected volume did not always cover the tissue sample location. The Enh- targets showed trends toward higher levels of normalized Cr (p=0.09) and lower levels of normalized Lac (p=0.07) compared to Enh+ targets, but with no significant difference in levels of Cho, NAA or Lip (Table 5.2). CNI

values were elevated in both Enh+ and Enh- samples (Table 5.2). There was an inverse correlation between nADC and both tCho (*p*=0.01) and CNI (*p*=0.007) for all samples (Table S5.1).
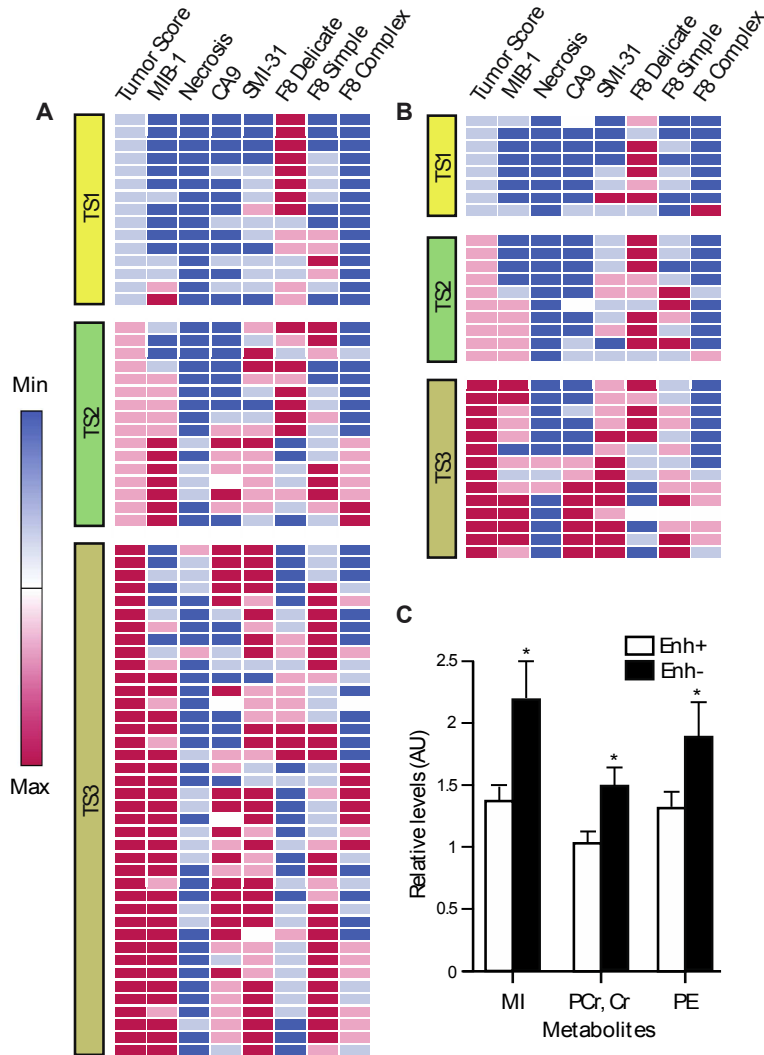

Figure 5.3. Histopathological parameters are depicted in heatmaps for Enh+ (A) and Enh- (B) GBM samples with deterministic hierarchical clustering applied to each tumor score (TS, 1-3) group. Metabolites showing statistically significant differences on the basis of enhancement status (C).

Histopathology

Tumor cellularity was similar between Enh+ and Enh- GBM, with only ~12% more Enh+ samples classified as representing maximal tumor content (Fig. 5.3; Table 5.3). Mean overall cell densities were almost identical at 286 (Enh+) versus 287 (Enh-) cells/200x field. There was no significant difference in the MIB-1 indices for Enh+ and Enh- samples (14.66% versus 12.88% - see Fig. 5.3 and Table 5.2). Delicate microvasculature predominated in 45% versus 24% of Enh- and Enh+ samples and was completely absent in almost a third of the Enh+ samples (OR, p = 3.10, 0.08) (Figure 5.2; Table 5.3). Simple microvasculature overwhelmingly characterized 41% of Enh+ samples compared to 19% of Enh- samples (OR, p =3.15, 0.07) (Fig. 5.3; Table 5.3), while Enh+ samples had relatively higher scores for complex microvasculature (Fig. 5.3; Table 5.3). Hypoxia (CA-9) and necrosis scores were not significantly different with regard to enhancement status, though their distribution favored Enh+ GBM. Axonal disruption (SMI-31) was comparable across all tumor samples.

Table 5.3. Analysis of categorical features. AD, axonal disruption; MVH, microvascular hyperplasia; NA, not applicable owing to insufficient non-zero scores; NS, not significant

Histology Parameter	Tissue Region	Number of Samples	Frequency Distribution of Categorical Scores (%)				Random Effect Model Analysis	
			0	1	2	3	Odds Ratio (95% CI)	*p*-value
Tumor score	Enh-	32	0	25.0	31.3	43.8	0.93	NS
	Enh+	70	0	21.4	22.9	55.7	(0.67 – 3.23)	
Necrosis	Enh-	32	90.6	3.1	6.3	NA	NA	NA

Histology Parameter	Tissue Region	Number of Samples	Frequency Distribution of Categorical Scores (%)				Random Effect Model Analysis	
			0	1	2	3	Odds Ratio (95% CI)	*p*-value
	Enh+	70	75.7	21.4	2.9	NA		
Hypoxia	Enh-	30	60.0	13.3	6.7	20.0	NA	NA
	Enh+	67	37.3	14.9	20.9	26.9		
AD	Enh-	32	15.6	28.1	28.1	28.1	0.96	NS
	Enh+	69	11.6	21.7	29.0	37.7	(0.65-3.56)	
delicate vasculature	Enh-	31	12.9	25.8	16.1	45.2	3.10	0.08
	Enh+	70	27.1	30.0	18.6	24.3	(0.16-1.10)	
simple MVH	Enh-	31	19.4	38.7	22.6	19.4	3.15	0.07
	Enh+	70	11.4	30.0	17.1	41.4	(0.92-5.15)	
complex MVH	Enh-	31	71.0	9.6	19.4	0	1.74	0.18
	Enh+	69	53.6	14.5	20.3	11.6	(0.69-6.65)	

There were several instances where the histological scores and values showed similar trends. Although both Enh+ and Enh- samples independently showed a strong correlation between tumor score and SMI31 (*p*=0.002, 0.004), the majority of correlations related to the enhancing tissue samples (Table S1). Among Enh+ GBM, tumor score was inversely correlated with the presence of delicate microvasculature (*p*=0.01) and positively correlated with CA9 expression (*p*=0.02), while CA9 correlated with necrosis (*p*=0.009) and had an inverse relationship with delicate vasculature (*p*=0.005). Microvascular hyperplasia in Enh+ samples was weakly related to MIB-1

(p=0.05). Both Enh+ and Enh- samples, showed a relationship between MIB-1 and average cellularity (p=0.002, 0.009).

Discussion

This study characterized the metabolomic profiles of tissue samples obtained from enhancing and non-enhancing regions in newly diagnosed GBM that were confirmed to contain tumor by histological analysis. *Ex vivo* ^{1}H HR-MAS metabolite levels were similar for tCho and NAA, but differed for a number of other metabolites that can be evaluated through *in vivo* methods utilizing short echo times. Analysis of the associated histopathology and multi-parametric MR examinations helped to contextualize and corroborate these findings. Given the heterogeneity of anatomic images with regard to contrast extravasation, having non-invasive parameters that can highlight non-enhancing tumor is of interest for planning surgical resection and for the ongoing assessment of total tumor burden.

The heterogeneity in *ex vivo* metabolite expression between Enh+ and Enh- samples may reflect biological differences in the tumor cells and their microenvironment. While Enh+ samples displayed a trend towards elevated methyl Lip that has commonly been linked with necrosis, the chemical profile of Enh- counterparts more closely resembled the increases in MI, Cr/PCr and Gly that were previously observed in samples from *de novo* grade III glioma, which lack necrosis and have limited microvascular proliferation (19). Although failing to reach statistical significance, the trend toward higher levels of GPC in Enh- GBM is also consistent with the metabolic profile displayed by grade III glioma. Elevation in the glia-associated metabolite MI, which has been

extensively employed for classifying infiltrating disease with respect to pathological grade, has also been reported for regions of tumor that are less malignant or contain gliosis based upon standard histological criteria (20, 21).

From a neurochemical perspective, the metabolomic profile exhibited by Enh- samples appears to confirm the heterogeneous nature of this disease, and suggests further investigation into the underlying significance of metabolite differences. The heightened levels of PCr/Cr observed in Enh- samples are likely to be due to the greater bioenergetic potential, as PCr contributes a reservoir of phosphate for rapid ATP generation (22). Trending levels of Gly, a non-essential amino acid and inhibitory neurotransmitter that is commonly found in high-grade glioma (23), are suggestive of malignant pathology, but no direct relationship has been established to explain its relative abundance. Owing to the *in vivo* overlap between Gly's singlet and the M-spin resonance of MI centered at 3.52 ppm, measurements of these two metabolites may be difficult to distinguish without application of techniques such as 2D *J*-resolved spectroscopy and spectral editing (24).

In assessing the pathobiology of GBM, consideration must also be given to the unique lipid metabolism that has been demonstrated in these lesions. Excess lipid has historically been associated with a poor prognosis for patients (25), and may relate to an aberrant oncogenic signaling EGFR/PI3K/Akt pathway that promotes lipid metabolism via the master transcriptional factor SREBP-1 (26). Previous HR-MAS investigations suggested that such lipid elevations are cytoplasmic in origin and indicative of necrosis, which is a pathological hallmark exclusive to GBM within the WHO criteria (27-29). While necrosis was not statistically differentiated in this study, it was noted as >2.5x more common in Enh+ samples. One of the above studies additionally

revealed that the presence of cholesteryl esters and triglycerides in cell extracts from GBM was correlated with the extent of vascular proliferation using both ^{1}H and ^{13}C HR-MAS techniques (29). Given the apparent relevance of lipid fractions to pathology, it is worth noting the elevation of PE in Enh- GBM, which suggests that there are differences in phospholipid metabolism associated with the Kennedy pathway (30).

Within Enh+ GBM, PE also showed multiple exceptionally strong correlations with other metabolites, including tCho and threonine. Because the cytidine diphophospate (CDP)-ethanolamine (Eth) pathway represents half of the Kennedy pathway, there are plausible relations of PE to choline species. The CDP-Eth pathway is additionally known to regulate diacylglycerol, a key activator of serine-threonine kinases, thus providing support for the association with threonine (31).

While limited in coverage and employment, the acquisition of *in vivo* ^{1}H MRSI data proved valuable for corroborating HR-MAS findings. Both *in vivo* and *ex vivo* spectroscopy demonstrated levels of tCho that were not statistically different between Enh+ and Enh- tumor, but nevertheless abnormally elevated relative to NAA, as demonstrated by the *in vivo* CNI values. Previous investigations have shown that the PC resonance forms the dominant contribution to the *in vivo* tCho peak in GBM, whether as primary tumor or secondary tumor that has transitioned from grade II or III glioma (19, 32). Because *ex vivo* Lac levels are considered unreliable given the ongoing metabolism of tissue following extraction, it was instructive to observe increased *in vivo* Lac levels in Enh+ GBM. Such increases may be attributed to heightened anaerobic respiration and/or interpolation of data with nearby necrosis on account of the coarse spatial resolution of MRSI.

Among the metabolites that distinguished Enh- samples, Cr/PCr and MI + Gly offer the greatest promise for *in vivo* characterization of differences between contrast-based radiographic subtypes of GBM. While the *ex vivo* elevation of Cr/PCr levels in Enh- relative to Enh+ samples was seen as a trend for *in vivo* ^{1}H MRSI data, the long echo time utilized in the current study prevented the detection of MI + Gly. Because of the T_2-shortening effects from MI's complex coupling, either a point-resolved spectroscopy (PRESS) sequence with a TE $\leq$ 35 ms or some Carr-Purcell-Meiboom-Gill (CPMG)-inspired sequence would be required for future studies (33).

The differences in vascular physiology assessed by *in vivo* perfusion-weighted imaging in this study were found to accurately reflect the microvascular heterogeneity of GBM represented by Factor VIII immunostaining. Elevations in nPH and nCBV in Enh+ regions were consistent with the observed propensity for microvascular hyperplasia and gross hypervascularity that are associated with angiogenesis. Reduced REC within the enhancing tumor is similarly indicative of immature, perforated vasculature whose permeability provides greater access to the extravascular, extracellular space. Although Enh+ regions displayed aberrant perfusion, the *in vivo* parameters observed in the Enh- regions remained within the range that is considered normal (34), and would therefore present a challenge for defining total tumor burden.

Analysis of the DWI data indicated that nADC values in tumor were similar irrespective of enhancement status, with median values near 1.5 reflecting moderately restricted diffusion. This finding is supported by the fact that overall cell density and tumor cellularity were comparable between Enh+ and Enh- samples. The *in vivo* nADC was also found to inversely correlate with

measures of tCho and CNI, which inform on tumor cellularity via choline species involved in membrane turnover. The higher values of nFA exhibited by Enh- samples demonstrated that non-enhancing components of the tumor may retain greater integrity of the surrounding tissue compared to that in the CE lesion, despite no clear differences in axonal disruption measured via SMI-31. Regardless of the potentially favorable structural status of Enh- samples, histopathologic analysis of MIB-1 mitotic indices indicated that there were similar levels of proliferation as in Enh+ samples. This suggests that Enh- tumor may bear a high degree of malignancy, even in the absence of patent contrast extravasation.

Besides providing evidence of comparable proliferation and cellularity between Enh+ and Enh-samples from GBM, the histopathology also showed internal relationships among several parameters. Both types of samples displayed the expected correlations between tumor score and axonal disruption, as well as between proliferation and average cellularity. For Enh+ samples, the association of hypoxia (as estimated by CA-9 scores) with regional necrosis provided validation of these respective assays. As might be anticipated, delicate vasculature, which is considered normal from a histological standpoint, was found to be inversely correlated with hypoxia for the Enh+ samples.

Conclusion

The results of this study indicate that *ex vivo* levels of tCho and NAA, as well as MIB-1 and tumor score are similar between CE and NE tumor samples. This is consistent with the *in vivo* findings and provides evidence to support the use of *in vivo* CNI as a metric for defining total tumor burden.

The *in vivo* levels of nADC were also found to be similar for CE and NE regions of tumor. Differences in *ex vivo* levels of Cr/PCr, as well as in the factor VIII scores and *in vivo* DSC parameters were consistent with the expectation that Enh- tumor has more normal-appearing vasculature. Although this may result in such regions being more responsive to radiation therapy, it may also mean that they receive a lower dose of chemotherapy, which could be a factor in driving recurrence.

Acknowledgements

Supplementary Material

T₂-weighted Anatomic Imaging

The standard pre-surgical imaging protocol included T_2-weighted sequences: axial fluid-attenuated inversion recovery (FLAIR; 10,000 ms/148ms/2200ms TR/TE/inversion time) and 3-D fast-spin echo (FSE; 3000ms/102ms TR/TE). As with other anatomic imaging, spherical regions with 5 mm diameter were defined based on tissue sampling coordinates recorded by surgical navigation software. Normalized intensity values for FLAIR (nFL) and FSE (nFSE) were obtained by

dividing median intensities in the corresponding tissue sample ROI by the mode of the intensity in the ROI from normal-appearing brain.

H&E and Immunohistochemistry

Overall cellularity was determined using the average number of all cells counted per 200x field. In order to evaluate proliferation in tumor-bearing samples, the MIB-1 index was computed as the proportion of tumor cells undergoing mitosis relative to the overall cellularity of the tissue. This assay was performed with the rabbit polyclonal MIB-1 anti-Ki67 (30-9) antibody (Ventana Medical Systems) at 2 µg/ml for 23 min at 37°C. Disruption of axonal architecture was measured using the mouse anti-SMI-31 (Covance) antibody at 1.5 µg/ml for 8 min at 37°C. A score of 0, no disruption; 1, minimal disruption; 2, mild disruption; 3, severe disruption with no residual SMI-31 immunostaining.

The extent of necrosis was scored based on a review of slides stained by hematoxylin & eosin (H&E): 0, no necrosis; 1, focal necrosis involving <50% of the tissue area; 2, extensive necrosis involving >50% of the tissue area. Hypoxia was also qualitatively measured via IHC staining for carbonic anhydrase (CA)-9, according to the degree of positivity: 0, no positive staining; 1, <10%; 2, ≥10% but <25%; 3, ≥25%.

Microvascular features were assessed in tumor samples via immunostaining for Factor VIII, rabbit polyclonal antibody (Dako) at 1.2 µg/ml for 20 min at 37°C. On the basis of Factor VIII IHC, microvascular morphology was graded as delicate (resembling normal cerebral vessels), simple microvascular hyperplasia (circumferential single cell hyperplasia with definitive lumen), or complex microvascular hyperplasia (circumferential multi-layered and glomeruloid-type vessels).

The relative contribution of each vascular morphology to total vascularity within the sample was qualitatively measured on a four-tiered ordinal scale (0, no contribution; 1, minimal; 2, prevalent; 3, predominant) at a magnification of 200x.

Table S5.1. Correlations among imaging and histopathologic parameters.

Parameters		Tissue Region	Mean ± SD Tau	Number of patients	*p*-value
PE	Glu	Enh+	0.67 ± 0.04	30	0.0004
PE	Thr	Enh+	0.72 ± 0.05	28	0.002
PE	tCho	Enh+	0.74 ± 0.03	31	0.0001
PE	Ala	Enh+	0.81 ± 0.03	27	0.00002
PE	Glu	Enh+	0.67 ± 0.04	30	0.002
Glu	tCho	Enh+	0.77 ± 0.03	34	0.000001
Thr	Ala	Enh+	0.77 ± 0.17	22	0.000003
MI	tCho	Enh+	0.65± 0.04	28	0.009
nADC	*in vivo* tCho	All	-0.67± 0.05	21	0.01
nADC	CNI	All	-0.69± 0.04	21	0.007
Tumor score	SMI-31	Enh+	0.58± 0.05	44	0.002
Tumor score	SMI-31	Enh-	0.71± 0.08	23	0.004
Tumor score	Delicate vasculature (presence)	Enh+	-0.66± 0.05	31	0.01
Tumor score	CA9	Enh+	0.52± 0.04	42	0.02

Parameters		Tissue Region	Mean ± SD Tau	Number of patients	*p*-value
CA9	necrosis	Enh+	0.55± 0.04	43	0.009
CA9	Delicate vasculature (Factor VIII)	Enh+	-0.53± 0.04	42	0.005
Microvasculature Hyperplasia (presence)	MIB-1(%)	Enh+	0.42 ± 0.03	45	0.05
Average cellularity	MIB-1(%)	Enh+	0.46 ± 0.04	42	0.002
Average cellularity	MIB-1(%)	Enh-	0.58 ± 0.03	21	0.009

References

1. Lois DN, Perry A, Reifenberger G, von Deimling A, Figarella-Branger D, Cavenee WK, Ohgaki H, Wiestler OD, Kleihues P, Ellison DW. The 2016 World Health Organization of tumors of the central nervous system: a summary. Acta Neuropathol. 2016; 131(6):803-820.

2. Johnson DR, O'Neill BP. Glioblastoma survival in the United States before and during the temozolomide era. J Neurooncol. 2012; 107: 359-364.

3. Sherry AD, Caravan P, Lenkinski, Primer on gadolinium chemistry. *JMRI* 2009; 30(6): 1240-1248.

4. Lu S, Ahn D, Johnson G, Cha S. Peritumoral diffusion tensor imaging of high-grade gliomas and metastatic brain tumors. Am J Neuroradiol. 2003; 24: 937-941.

5.McKnight TR, von dem Bussche MH, Vigneron DB, Lu Y, Berger MS, McDermott MW, Dillon WP, Graves EE, Pirzkall A, Nelson SJ. Histopathological validation of a three-dimensional

magnetic resonance spectroscopy index as a predictor of tumor presence. J Neurosurg. 2002; 97(4): 794-802.

6.Park I, Chen AP, Zierhut M, Ozturk-Isik E, Vigneron DB, Nelson SJ. Implementation of 3T lactate-edited 3D 1H MR spectroscopic imaging with flyback echo-planar readout for glioma patients. *Ann. Biomed. Eng.* 2011; 39: 193–204.

7.Basser PJ, Pierpaoli C. Microstructural and physiological features of tissues elucidated by quantitative diffusion-tensor MRI. J. Magn. Reson. B, 1996; 111: 209–219.

8.Li Y, Osorio JA, Ozturk-Isik E *et al*. Considerations in applying 3D PRESS H1 brain MRSI with and eight-channel phased-array coil at 3T. Magnetic Resonance Imaging 2006; 24(10):1295-1302.

9.McKnight TR, Noworolski SM, Vigneron DB, Nelson SJ. An automated technique for the quantitative assessment of 3D-MRSI data from patients with glioma. J. Magn. Reson. Imaging 2001; 13: 167–177.

10.Albers MJ, Butler TN, Rahwa I, Bao N, Keshari KR, Swanson MG, Kurhanewicz, J. Evaluation of the ERETIC method as an improved quantitative reference for 1H HR-MAS spectroscopy of prostate tissue. Magn. Reson. Med. 2009; 61: 525–532.

11.Stefan D, Cesare FD, Andrasescu A, Popa E, Lazariev A, Vescovo E, Strbak O, Williams S, Starcuk Z, Cabanas M, van Ormondt D, Graveron-Demily D. Quantitation of magnetic resonance spectroscopy signals: the jMRUI software package. Meas. Sci. Technol. 2009; 20: 104035(9pp).

12.*S.M. Smith. Fast robust automated brain extraction. Human Brain Mapping 2002; 17(3):143-155.*

13.Ratiney H, Albers MJ, Rabeson H, Kurhanewicz J. Semi-parametric time-domain quantification of HR-MAS data from prostate tissue. NMR Biomed. 2010; 23: 1–13.

14.Lee MC, Cha S, Chang SM, et al. Dynamic susceptibility contrast perfusion imaging of radiation effects in normal-appearing brain tissue: changes in the first-pass and recirculation phases. J Magn Reson Imaging. 2005;21(6):683–693.

15.Lupo JM, Cha S, Chang SM, et al. Dynamic susceptibility weighted perfusion imaging of high-grade gliomas: characterization of spatial heterogeneity. Am J Neuroradiol. 2005;26(6) 1446–1454.

16.R Core Team (2013). R: A language and environment for statistical computing. R Foundation for Statistical Computing, Vienna, Austria.

17.Barajas RF, Phillips JJ, Parvateneni R, Molinaro A, Essock-Burns E, Bourne G, Parsa AT, Aghi MK, McDermott MW, Berger MS, Cha S, Chang SM, Nelson SJ. Regional variation in histopathologic features of tumor specimens from treatment-naïve glioblastoma correlates with anatomic and physiologic MR Imaging. Neuro-Oncology 2012; 14(7): 942-954.

18.Opstad KS, Bell BA, Griffiths JR, Howe FA. An assessment of the effects of sample ischaemia and spinning time on the metabolic profile of brain tumour biopsy specimens as determined by high-resolution magic angle spinning 1H NMR. *NMR Biomed*. 2008; 21(10): 1138–1147.

19.Elkhaled A, Llewellyn J, Constantin A, Yoshihara HAI, Phillips JJ, Molinaro AM, Chang SM, Nelson SJ. Characterization of metabolites in infiltrating gliomas using ex vivo 1H high-resolution magic angle spinning spectroscopy. *NMR Biomed*. 2014; 27(5): 578- 593.

20.Castillo M, Smith JK, Kwock L. Correlation of myo-inositol levels and grading of cerebral astrocytomas. Am J Neuroradiol. 2000; 21(9): 1645 - 1649.

21.Candiota AP, Majos C, Julia-Sape M, Cabanas M, Acebes JJ, Moreno-Torres A, Griffiths JR, Arus C. Non-invasive grading of astrocytic tumours from the relative contents of myo-inositol and glycine measured by in vivo MRS. JBR-BTR. 2011; 94(6): 319-329.

22.Govindaraju V, Young K, Maudsley AA. Proton NMR chemical shifts and coupling constants for brain metabolites. NMR Biomed 2000; 13: 129-153.

23.Righi V, Andronesi OC, Mintzopoulos D, Black MB, Tzika AA. High-resolution magic angle spinning magnetic resonance spectroscopy detects glycine as a biomarker in brain tumors. Int J Oncol. 2010; 36(2): 301-306.

24.Schulte RF, Boesiger P, ProFit: two-dimensional prior-knowledge fitting of J-resolved spectra. NMR Biomed. 2006; 19: 255-263.

25.Li Yan, Lupo JM, Parvataneni R, Lamborn KR, Cha S, Chang SM, Neslon SJ. Survival analysis in patients with newly diagnosed glioblastoma using pre-and post radiotherapy MR spectroscopic imaging. Neuro Oncol. 2013; 15(5): 607-617.

26.Guo D, Bell EH, Chakravarti A. Lipid metabolism emerges as a promising target for malignant glioma therapy. CNS Oncol. 2013; 2(3); 289-299.

27.Cheng LL, Anthony DC, Comite AR, Black PM, Tzika AA, Gonzalez RG. Quantification of microheterogeneity in glioblastoma multiforme with ex vivo high-resolution magic-angle spinning (HRMAS) proton magnetic resonance spectroscopy. Neuro Oncol. 2000; 2(2): 87- 95.

28.Opstad KS, Bell BA, Griffiths JR, Howe FA. An investigation of human brain tumour lipids by high-resolution magic angle spinning 1H MRS and histological analysis. NMR Biomed. 2008; 21(7): 677-685.

29.Tugnoli V, Tosi MR, Tinti A, Trinchero A, Bottura G, Fini G. Characterization of lipids from human brain tissues by multinuclear magnetic resonance spectroscopy. Biopolymers. 2001; 62(6): 297-306.

30.Esmaeili M, Hamans BC, Navis AC, van Horssen R, Bathen TF, Gribbestad IS, Leenders WP, Heerschap A. IDH1 R132H mutation generates a distinct phospholipid metabolite profile in glioma. Cancer Res. 2014; 74: 4898.

31.Selathurai A, Kowalski GM, Burch ML, et al. The CDP-ethanolamine pathway regulates skeletal muscle diacylglycerol content and mitochondrial biogenesis without altering insulin sensitivity. Cell Metabolism 2015; 21: 718-730.

32.Glunde K, Bhujwalla ZM, Ronen SM. Choline metabolism in malignant transformation. *Nat. Rev. Cancer* 2011; 11(12): 835–848.

33.Hancu I. Which pulse sequence is optimal for myo-inositol detection at 3T? NMR Biomed. 2009; 22(4): 426 - 435.

34.Law M, Young RJ, Babb JS, et al. Gliomas: predicting time to progression or survival with cerebral blood volume measurements at dynamic susceptibility-weighted contrast-enhanced perfusion MR imaging. Radiology 2008;247:490–498.

Chapter 6: Summary

With the advent of novel molecular techniques, infiltrating glioma have become increasingly subject to interrogation in the modern era. Despite this advancement, treatment for patients remains inadequate on account of limited efficacy and the variability associated with outcome. In the ongoing struggle to monitor response to therapy and more broadly validate emerging clinical trial agents, MRI plays a critical role through diagnostic characterization. Anatomical MRI, as the gold standard of neuro-imaging, provides an excellent means of defining certain abnormalities, yet is beset by ambiguity from non-specific changes that complicate its interpretation. Given this challenge, MR spectroscopic imaging has been employed to augment the functionality of MRI in characterizing infiltrating glioma.

This work sought to identify markers of disease using *ex vivo* high-resolution spectroscopic techniques and then to promote their translation via MRSI. Based on *ex vivo* analysis, it was determined that standard pathological subtypes of infiltrating glioma could be differentially classified according to distinct metabolomic profiles. Such profiles were also found to be relevant in predicting pathologic trajectory by distinguishing between glioma that had undergone malignant progression and those that had remained at the same level of malignancy. Among the patterns of metabolite expression, individual markers may have implications for gauging levels of malignancy prior to surgery and monitioring longitudinal reponse to therapy. Other *ex vivo* work helped characterize contrast-based radiographic subtypes of the most aggressive form of glioma and revealed distinct metabolite expression within the non-T_l enhancing tumor lesion that is not

identifiable by conventional MR imaging. As a result, this study provided practical guidelines for delineating tumor using *in vivo* spectroscopy in conjunction with physiologic imaging.
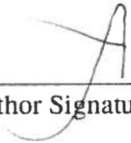
Because many of the important metabolite markers identified from these studies exhibited strong coupling, an *in vivo* MRSI sequence was developed to improve their detection. By introducing multiple broadband RF refocusing pulses with nonlinear phase, it was possible to reduce the peak B_1 and improve the signal fidelity of these metabolites over longer acquisition times. This represents part of the larger effort to exploit the clinical utility of spectroscopy through the translation of relevant biomarkers. As such techniques become more accessible, their integration into standard practice will greatly enhance the role of diagnostic imaging in evaluating patients.

Publishing Agreement

It is the policy of the University to encourage the distribution of all theses, dissertations, and manuscripts. Copies of all UCSF theses, dissertations, and manuscripts will be routed to the library via the Graduate Division. The library will make all theses, dissertations, and manuscripts accessible to the public and will preserve these to the best of their abilities, in perpetuity.

Please sign the following statement:

I hereby grant permission to the Graduate Division of the University of California, San Francisco to release copies of my thesis, dissertation, or manuscript to the Campus Library to provide access and preservation, in whole or in part, in perpetuity.

_____   12/16/16
Author Signature   Date